2019

Hurricane Imaging Radiometer (HIRAD) Tropical Rainfall Retrievals

Abdusalam Alasgah
University of Central Florida

HURRICANE IMAGING RADIOMETER (HIRAD) TROPICAL RAINFALL RETRIEVALS

by

ABDUSALAM NASSER ALASGAH
B.S. King Saud university, 2009
M.S. University of Central Florida, 2015

A dissertation submitted in partial fulfillment of the requirements
for the degree of Doctor of Philosophy
in the Department of Electrical and Computer Engineering
in the College of Engineering and Computer Science
at the University of Central Florida
Orlando, Florida

Fall Term
2019

Major Professor: W. Linwood Jones

ABSTRACT

The Hurricane Imaging Radiometer (HIRAD) is an airborne passive microwave remote sensor, developed to measure wind speed and rain rate in hurricanes. This dissertation concerns the development of a signal processing algorithm to infer tropical rainfall from HIRAD radiance (brightness temperature, Tb) measurements.

The basis of the rain rate retrieval algorithm is an improved forward microwave radiative transfer model (RTM) that incorporates the HIRAD multi-antenna-beam geometry, and uses semi-empirical coefficients derived from an airborne experiment that occurred in the Gulf of Mexico off Tampa Bay in 2013. During this flight, HIRAD observed a squall line of thunderstorms simultaneously with an airborne meteorological radar (High Altitude Wind and Rain Profiler, HIWRAP), located on the same airplane. Also, ground based NEXRAD radars from the National Weather Service (located at Tampa and Tallahassee) provided high resolution simultaneous rain rate measurements.

Using NEXRAD rainfall as the surface truth input to the HIRAD RTM, empirical rain microwave absorption coefficients were tuned to match the measured brightness temperatures. Also, the collocated HIWRAP radar reflectivity (dBZ) measurements were cross correlated with NEXRAD to derive the empirical HIWRAP radar reflectivity to rain rate relationship. Finally, the HIRAD measured Tbs were input to the HIRAD rain retrieval algorithm to derive estimates of rain rate, which were validated using the independent HIWRAP measurements of rain rate.

ACKNOWLEDGMENT

First I would like to thank my family, without their support over the years none of this would have been possible. They have always been there for me and I am thankful for everything they have helped me achieve.

Next, I would like to thank my advisor Professor Dr. Linwood Jones for the unlimited support and guidance he provided for me over the past four years. I am so fortunate to have such an advisor, thank you for the knowledge you have passed on and I will always be grateful for having the opportunity to do my research under your supervision. I would like to thank my dissertation committee Dr. Parveen Wahid, Dr. Wasfy Mikhael, Dr. Xun Gong and Dr. Josko Zec for their inputs and support

I would also like to thank the CFRSL lab members for their continuous support and assistantship to pass every obstacle through my time in the lab, can't ask for a better team and working environment.

TABLE OF CONTLENT

LIST OF FIGURES

LIST OF TABLES

CHAPTER 1:
INTRODUCTION

1.1 Overview of HIRAD science

This dissertation is a continuation of the Central Florida Remote Sensing Laboratory's (CFRSL) contribution toward the Hurricane Imaging Radiometer (HIRAD) research, and the goal of this dissertation focuses on the retrieval of rain rate in hurricanes using the multi-frequency brightness temperatures (Tbs) measured by HIRAD. The HIRAD instrument is an airborne multiple channel (4, 5, 6 and 6.6 GHz) passive microwave radiometer. Operating onboard of two different NASA high-altitude aircraft (WB-57 and Global Hawk, at an altitude of ~ 20 km), HIRAD provides microwave Tb images over a swath of 60 km with high spatial resolution of 2 - 5 km. From these Tb measurements, the hurricane ocean surface wind and tropical rain fields are inferred.

HIRAD was developed by the National Aeronautics and Space Administration (NASA) Marshall Space Flight Center (MSFC) during the period 2004-2010, as a collaboration with the National Oceanic and Atmospheric Administration (NOAA) Hurricane Research Division (HRD), the Central Florida Remote Sensing Laboratory (CFRSL) and the University of Michigan (UM). This imaging microwave radiometer was developed as a prototype of the next generation hurricane wind sensor, which operates on the HRD hurricane hunter aircraft. Its design was based on the present sensor, the Stepped Frequency Microwave Radiometer (SFMR) [1]. While SFMR is the only remote sensor presently capable of measuring the surface wind speed, it's utility in hurricane surveillance is limited by the narrow measurement swath (< 1 km) along the aircraft ground track. Thus, the surveillance aircraft usually flies a "Figure-4" pattern through the hurricane eye (as

shown in Figure 1-1), to sample the winds in 4 quadrants of the storm, which takes between 1 – 2 hours to complete. On the other hand, the potential of HIRAD is to image the entire hurricane eye wall region that contain the peak winds in a single pass from a high altitude aircraft. Thus, HIRAD offer the potential to improve hurricane surveillance for the future.

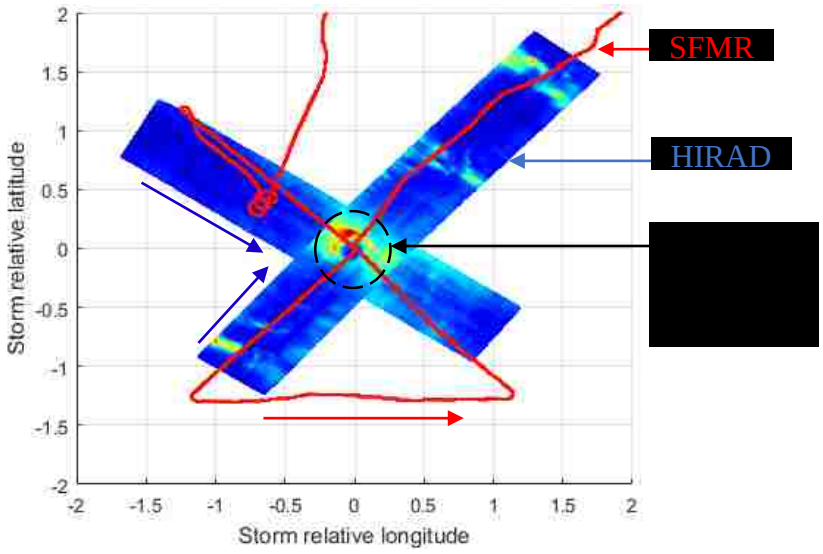

Figure 1-1: Typical Hurricane Hunter aircraft "Figure-4" flight pattern with SFMR and HIRAD measurement swaths shown.

1.2 Rain Impact on Hurricane Retrievals

The HIRAD concept was based upon simultaneously obtaining images of the hurricane at several widely spaced microwave frequencies, which allows the retrieval of both ocean wind speed (WS) and rain rate (RR). Before the hardware development and flight testing of HIRAD, theoretical studies were performed that demonstrated that accurate WS and RR retrievals were possible in the presence of expected random instrument Tb measurement errors (delta-Tb) [2]-[6].

For a number of reasons, the promise of hurricane WS and RR retrievals has yet to come to fruition. Based upon early HIRAD measurements over hurricanes, the hurricane measurement

requirement was relaxed to measure only WS in the presence of rain (i.e., ignore the rain rate measurement). Unfortunately, the experience has been shown that even moderate rain dominated the retrieval, and as a result, the WS measurement is usually severely compromised. However, when rainfall is light, it is possible to measure WS, but the issue has been to reliably identify (flag) where it was raining. This dissertation addresses this issue and seeks to provide a forward Radiative Transfer Model (RTM), which is necessary first step toward developing a quantitative rain rate retrieval algorithm for moderate to strong tropical rainfall. In this way, simultaneous retrievals of both WS and RR may be possible; or at a minimum, WS can be reliably flagged as rain contaminated and a realistic WS measurement error estimate can be provided.

To perform rain rate retrievals, a crucial factor is the ability to theoretically model the rain Tb over the ocean as a function of earth incidence angle (EIA) and radiometer frequency. Prior to this dissertation, this Tb model was strictly theoretical and not validated by experimental evidence, but this research takes advantage of a unique observation opportunity that occurred during a strong tropical rainfall, whereby the HIRAD instrument measured Tb simultaneously with two meteorological radar measurements. This event known as the Tampa Bay Rain Experiment, provided empirical data, which allowed the HIRAD forward RTM to be tuned to match the independent rain rate observations of the two radar remote sensors [7].

1.3 Dissertation Research Objectives

The objective of this research is to lay the foundation for the development a rain rate retrieval algorithm for HIRAD. This is a tedious process that involves the following tasks, which are described in the subsequent chapters:

1. Process airborne and ground-based meteorological radar reflectivity to provide estimates of the "true" ocean scene 3D rain volume that was observed by HIRAD.
2. Development of a theoretical forward RTM that accurately models HIRAD oceanic scene brightness temperatures using the geometry for a single cross-track scan and at 5, 6 & 6.6 GHz.
3. Investigate preliminary RR retrieval algorithms using the HIRAD forward RTM.

1.4 Description of Tampa Bay Rain Experiment

The Tampa Bay Experiment was part of the Hurricane and Severe Storm Sentinel (HS3) mission; a 5-year airborne hurricane measurement conducted by NASA, to provide a better understanding of hurricane formation and intensity processes [8]. This flight research program flew 21 missions with a total of 670 hours of flight time using NASA's Global Hawk and WB-57 aircraft; however, for this dissertation, only limited observations from the "over-storm payload" were applicable, which included HIRAD and the High-Altitude Imaging Wind and Rain Airborne Profiler (HIWRAP - conically scanning Doppler radar) that provided 3D imaging of rainfall within the atmosphere.

On September 16, 2013 (GMT: Sept. 16 @ 01:37), a tropical squall-line of thunderstorms was observed simultaneously by the HIRAD, HIWRAP and the ground-based NOAA National Weather Service Next-generation Radar (NEXRAD) at Tampa and Tallahassee, Florida. This was a serendipitous event that provided the important tropical precipitation observation dataset, which is the basis for this dissertation. While unplanned, the HIRAD scientist (in the mission control room) recognized the potential of this opportunity and requested a real-time deviation to the flight

plan, which was implemented and became the “Tampa Bay Rain Experiment” (see Section 4.1 for more details). What was unique in this experiment was the combination of the HIWRAP airborne radar (see Section 2.3) and calibrated ground-based radars (see Section 2.4) that simultaneously viewed the intense rain event and provided a 3D rain volume, which was viewed by HIRAD.

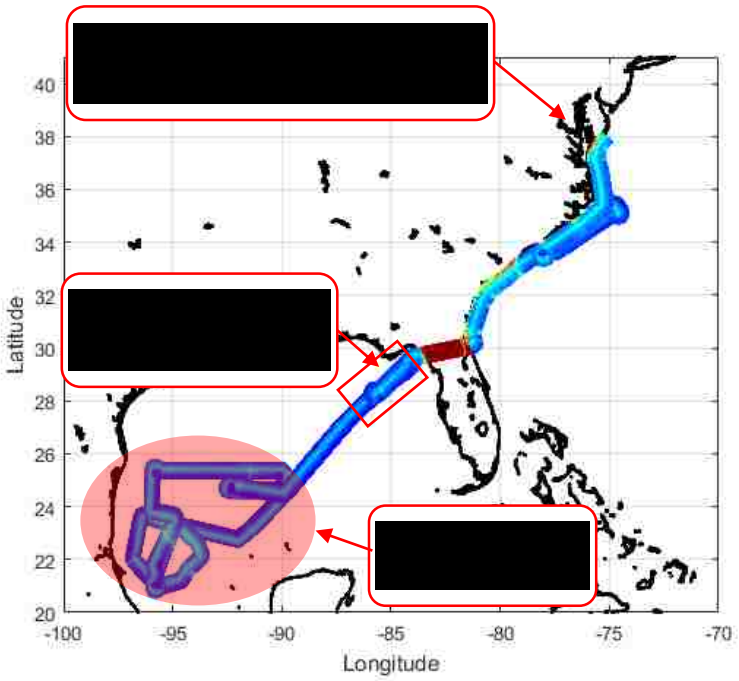

Figure 1-2: Global Hawk flight path during HS3 flight on Sept. 16, 2013. Note the locations of the Tampa Bay Rain Experiment and the HIRAD land-calibration.

Details of the Global Hawk flight lines, which collected Tb and radar reflectivity observations used in this dissertation, are shown in Figure 1-2. For this 30-hour flight, the Global Hawk aircraft flew to observe a hurricane in the western Caribbean Sea near the coast of Mexico. On the return to the NASA Wallops Flight Facility, the aircraft passed over a tropical squall line with intense rain, and as a result three Global Hawk passes were conducted over this unplanned event, which provided the data used in this dissertation.

1.5 Dissertation outline

The research performed under this dissertation is described in the following chapters:

Chapter 2 presents a description of the instruments that provided these data; Chapter 3 presents a discussion of the measurement 3D grid used in the analysis; the measurement geometry for HIRAD, HIWRAP and NEXRAD; and the geolocation validation for HIWRAP surface reflectivity image features as compared to Google Earth maps; Chapter 4 presents 3D rain reflectivity measurements from HIWRAP and NEXRAD; Chapter 5 presents the HIRAD forward Radiative Transfer Model and discusses the sampling of NEXRAD 3D rain volume into the RTM layers. Also results of comparisons between measured and modeled Tbs are presented; Chapter 6 presents a maximum likelihood estimation HIRAD rain rate retrieval algorithm and comparisons with the independent NEXRAD rain rate measurements. Finally, Chapter 7 presents conclusions and recommendations for future studies.

CHAPTER 2:
INSTRUMENT DESCRIPTION

2.1 Hurricane and Severe Storm Sentinel (HS3) Mission

The Hurricane and Severe Storm Sentinel (HS3) Mission [8] was a five-year airborne observations program under NASA's Earth System Science Pathfinder Program, which was one of five large field campaigns operating under the Earth Venture program. The science objectives of HS3 was to investigate the processes that underlie hurricane formation and intensity change in the Atlantic Ocean basin. HS3 was motivated by hypotheses related to the relative roles of the large-scale environment and storm-scale internal processes.

The Global Hawk Unmanned Air Vehicle (UAV), is NASA's newest platform for suborbital remote sensing research, and it is an ideal platform for investigations of hurricanes, capable of flight altitudes greater than 19 km (55,000 ft) and flight durations of up to 30 hours, with round-trip distances greater than 9,000 miles. HS3 used two Global Hawks, one with an instrument suite geared toward measurement of the atmospheric environment, and the other with instruments suited to inner-core hurricane structure and processes. The over-storm environmental payload included the High-Altitude Imaging Wind and Rain Airborne Profiler (HIWRAP - conically scanning Doppler radar), the Hurricane Imaging Radiometer (HIRAD - multi-frequency interferometric radiometer), and the High Altitude Monolithic Microwave integrated Circuit (MMIC - Sounding Radiometer – not included in this dissertation), and Figure 2-1 shows the location of HIRAD and HIWRAP on the Global Hawk. During 2014, flights from NASA's Wallops Flight Facility in Virginia occurred between Aug. 26 and Sept. 29, during the peak of the Atlantic hurricane season. Being an unmanned aircraft, the Global Hawk was operated by pilots

in a control room at the NASA Dryden Flight Center in California, with 2-way communications provided by redundant satellite links. The UAV used the Inertial Navigation System (INS) for guidance, navigation and control of the aircraft, and important flight parameters (e.g., altitude, attitude: roll, pitch and yaw, engineering telemetry, etc.) where recorded in real-time during its missions.

Figure 2-1: Global Hawk UAV with major remote sensor instruments.

An example of the HS3 flight track, which provided the observations used in this dissertation, is shown in Figure 1-2. For this 30-hour flight, the Global Hawk flew to observe a hurricane in the western Caribbean Sea near the coast of Mexico. On the return to the NASA Wallops Flight Facility, the aircraft passed over a tropical squall line with intense rain, and as a result three Global Hawk passes were conducted over this unplanned event, which provided the data used in this dissertation.

2.2 HIRAD Overview

The Hurricane Imaging Radiometer (HIRAD) is an airborne passive microwave radiometer that measures C-band brightness temperatures, which are processed to retrieve images of oceanic wind speed and rain rate for research purposes. It operated onboard two of NASA's aircrafts WB-

57 and Global Hawk, which are manned and unmanned aircrafts respectively, flying at an altitude around ~ 20 km.

HIRAD was developed as a joint project between NASA Marshall Space Flight Center (MSFC), the National Oceanic and Atmospheric Administration (NOAA) Hurricane Research Division, the Central Florida Remote Sensing Laboratory (CFRSL) and the University of Michigan. The objective was to develop a prototype of a microwave imager capable of imaging a typical hurricane in a single pass, which could significantly improve the wind speed measurements provided by the nadir viewing Step Frequency Microwave Radiometer (SFMR).

The antenna on HIRAD captures microwave emissions from the ocean surface, which is used to produce a two-dimensional image of the hurricane surface wind field that can provide a significant advantage over the current narrow swath SFMR sensor. In addition, HIRAD provides multi-frequency brightness temperatures that enables the retrieval of both tropical rainfall and hurricane surface wind speed. The measurement swath of HIRAD compared to a typical hurricane wind field is shown in Figure 2-2.

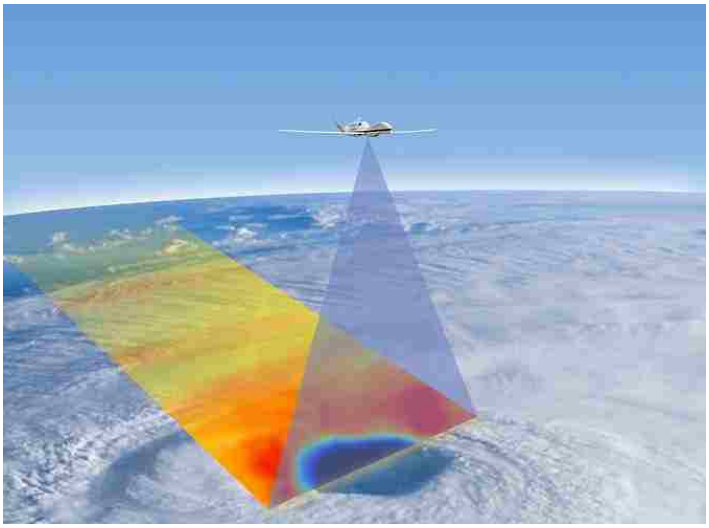

Figure 2-2: HIRAD able to image complete hurricane eyewall in a single pass.

2.2.1 HIRAD 1D STAR Measurements

HIRAD is designed to provide images of the retrieved ocean wind speed and rain rate over a wide swath, using Synthetic Thinned Array Radiometer (STAR) technology [9]. The instrument operates as a spectrometer that measures the Fourier transform of the ocean brightness temperature (Tb) scene in "cross-track scans" at 4 C-band channels (4, 5, 6, 6.6 GHz). For each channel, the individual spectral Tb components (known as visibilities) are created by complex cross-correlation interferometers between pairs of the antenna arrays. A brightness temperature image of the earth scene is produced every second (known as a scan) by an inverse Fourier transform of the visibilities. From these Tb measurements, it is possible to infer ocean surface winds (up to hurricane force) even in the presence of strong tropical rains.

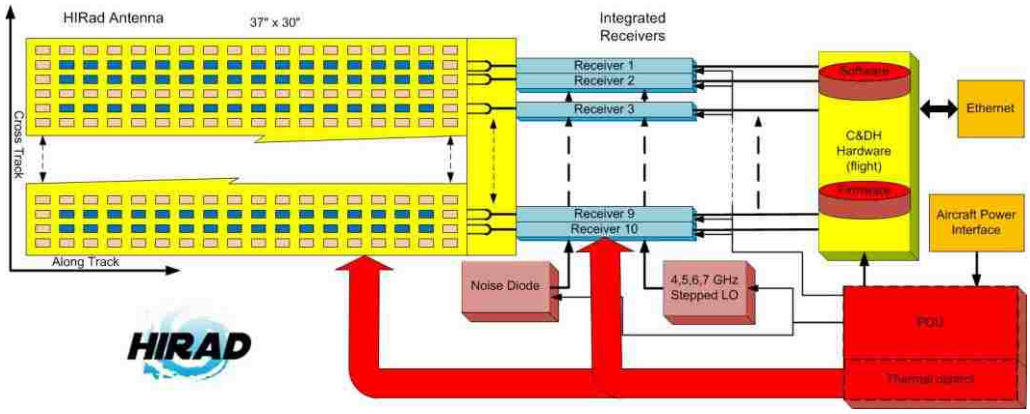

Figure 2-3: HIRAD block diagram.

The instrument block diagram (Figure 2-3) comprises an integrated stacked patch antenna array of 10 fan beam elements and corresponding analog radiometer receivers with integrated calibration sources, a real-time digital signal processor, and subsystems for command and data handling (C&DH) and for power distribution (PDU) and thermal control. The signals from each of the 10 linear array elements (fan beam antenna patterns) are filtered, amplified, demodulated and digitized by dedicated receivers. All possible pairs of the 10 radiometer signals are cross-correlated in the digital signal processor using complex multipliers to form the raw, un-calibrated, visibility samples that make up level-0 archival data produced by the sensor. Data are recorded on an on-board hard drive and downloaded after flight.

2.2.2 Antenna Description

HIRAD antenna (Figure 2-4) is a phased array of 10 linear array antennas (Sticks) that used electronic signal processing (correlation receivers) to synthesize the equivalent of multiple push-broom antennas [9, 10]. The antenna was designed to measure horizontally polarized brightness temperature, but also an unwanted cross polarization is captured, which is only significant at the

edge of the swath. Each stick array is composed of stacked multi-resonant radiators, operating at 4 C-band frequencies 4, 5, 6 and 6.6 GHz. Each linear array (Stick) is an individual fan beam antenna element, that is placed in an optimum thinned array configuration to produce the interferometer baselines needed for aperture synthesis [9]. All the fan beams overlap defining a "brightness temperature strip" on the earth surface to be imaged.

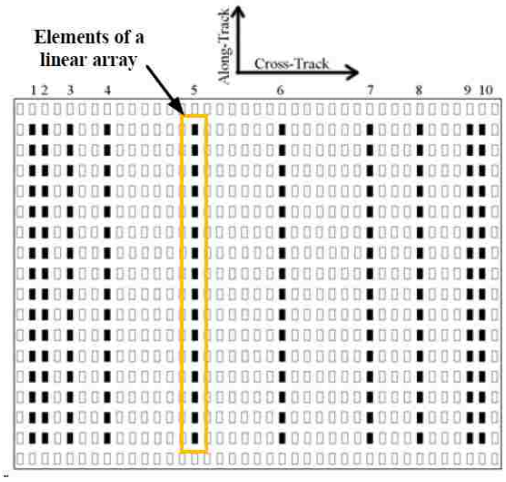

Figure 2-4: HIRAD array antenna with 10 linear array elements shown in bold symbols [3].

The HIRAD Tb image sub-pixels along the strip are resolved by interferometry, and the strip is oriented cross track (±90°) to the direction of motion, so that the aircraft forward motion creates an equivalent "pushbroom" image (see Figure 2-5), with 321 overlapping beams spaced equally in the nadir scan angle. By signal processing, the HIRAD instantaneous field of view (IFOV) is synthesized by summing beams to match the IFOV's for the four frequencies. The effective beamwidth of the antenna beams is a few degrees that increases monotonically with cross-track location, which results in an IFOV at nadir of ~ 2 km and ~ 6 km at edge of swath. The

HIRAD Tb image is limited to ±60 degrees, and the resulting swath width is ~ 3 x Altitude (60 Km for a typical flight altitude of 20 km).

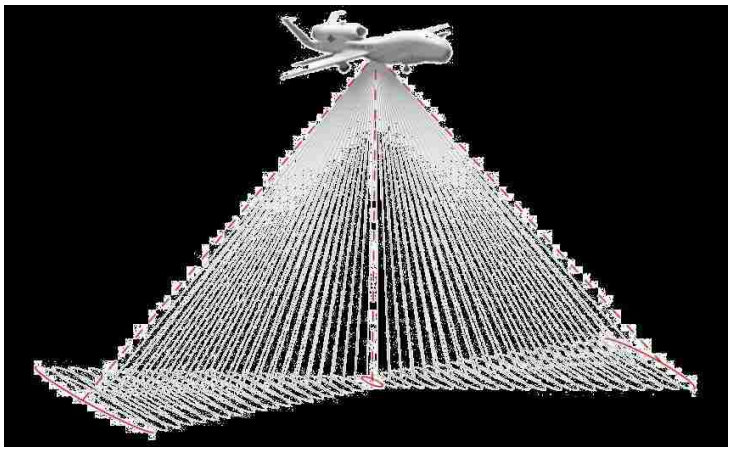

Figure 2-5: HIRAD equivalent pushbroom radiometer.

2.2.3 Data Format (Beams vs. Scan)

HIRAD Tb image comprise 321 beam positions in the cross-track direction by the number of scans (time duration of the flight line), which are described in detail in Chapter 3. The HIRAD Tb data used in this dissertation were collected during the HS3 flight on Sept. 16, 2013. NASA MSFC performed all HIRAD post-flight data processing to produce these brightness temperatures and associated geolocation parameters.

2.3 HIWRAP Overview

The High-Altitude Imaging Wind and Rain Airborne Profiler (HIWRAP) is a conical scanning meteorological Doppler radar that operates on the Global Hawk [11]. As its name implies, HIWRAP is designed to provide calibrated reflectivity (dBZ) and Nyquist sampled Doppler velocity measurements in 250 m range gates from the aircraft to the surface. In the

atmosphere, the radar backscatter is from precipitation, which is advected by the local atmospheric winds; therefore, HIWRAP measurements are used to retrieve 3-dimensional tropospheric winds and the associated precipitation field. Also, the surface echo can be used to retrieve ocean vector surface winds.

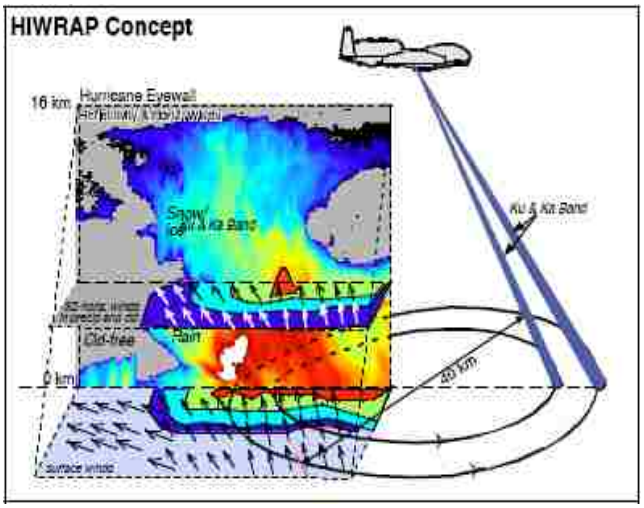

Figure 2-6: HIWRAP measurement geometry from [11].

HIWRAP is dual frequency radar that operates at Ku (13.5 GHz) and Ka band (34 GHz), which transmits and receives with a spinning 0.5 m parabolic reflector that produces two pencil beams at corresponding incident angles of 30 and 40 degrees. As shown in Figure 2-6, the beams conically scan through the volume, while measuring the Doppler/reflectivity profiles from both beams simultaneously. For this dissertation, only the Ku-band reflectivity data are applicable.

2.4 NEXRAD

The Next-Generation (meteorological) Radar (NEXRAD) system is operated by the National Oceanic and Atmospheric Administration - National Weather Service (NOAA-NWS)

[12]. This national radar network of 159 NEXRAD sites, within the continental U.S., provides continuous meteorological radar measurements at high spatial and temporal coverage for the area.

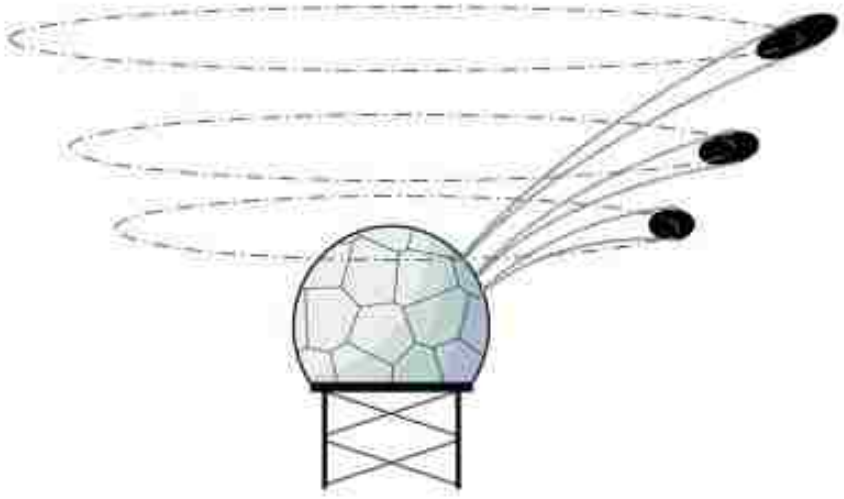

Figure 2-7: NEXRAD volume scan showing 3 of multiple (typically 8) elevation scans.

NEXRAD is a dual polarized Doppler radar that operates at ~2.8 GHz (S band), with a conically scanning 8.5 m diameter dish antenna (~ 1° beamwidth). The radar measurements are obtained in volume scans (see Figure 2-7), which corresponds to a series of conical antenna 360° rotations at different radar elevation angles (0.5 to 19 degrees) that are known as volume-scan levels. The radar data products are supplied in data granules of individual volume scans that typically occur at a 4 – 5 minute refresh period.

The NEXRAD system provides a wide range of radar data products, divided between reflectivity-based product (of interest for this dissertation) and radial velocity based products (not used for this research). The base (Level-1) reflectivity data are binned and averaged into range cells that are 1^{o} azimuth resolution by 1 km range resolution, over a distance (range) of a few km out to a max range of 460 km. All data products are viewable using the National Weather Service "Weather and

Climate Tool kit" (WCT), which allows users to select the desired product and level and to view reflectivity images of the region of interest. The reflectivity data are sorted in polar coordinates (range and azimuth), along with the time and the antenna elevation angle of each measurement. For this dissertation, using the known altitude of the radar beam at a given range, we transform the radar data into a Cartesian grid (longitude, latitude and altitude) which is discussed in detail in Chapter 3.

CHAPTER 3:
GEOLOCATION VALIDATION

As described in Section 1.3, the objective of this research is to:

1. develop of a theoretical forward radiative model that accurately models the HIRAD oceanic scene brightness temperatures (with heavy rain) for a cross-track scan,
2. provide empirical validation of the forward RTM for the Tampa Bay Rain Experiment,
3. and investigate an inverse retrieval algorithm to infer "path average rain rate" for a cross-track scan.

This chapter provides details concerning geolocation of the HIRAD, HIWRAP and NEXRAD data sets, which are a crucial sub-part of these tasks. Note that these research objectives uses the 3D rain imagery provided by the National Weather Service NEXRAD weather radar at Tallahassee, FL and the 3D rain imagery provided by the HIWRAP. Because of the transient nature of a propagating tropical squall line of thunderstorms, it is crucial that these two radar measurements be aligned spatially and temporally. Therefore, an important part of this research is to perform a detailed evaluation of HIWRAP radar pixel geolocation (latitude, longitude), which is accomplished using HIWRAP surface reflectivity images of high-contrast land/water boundaries. In this chapter, we discuss methodologies implemented to validate the radar pixel's geolocation accuracy, and results are presented to provide quantitative pixel geolocation errors compared to high-resolution Google Earth maps.

3.1 HIRAD 3D Grid

The selection of the common 3-dimensional (3D) grid was an important decision that was made early-on during the dissertation research. Both HIWRAP and NEXRAD were conical scan geometries, and HIRAD was a cross-track scanning geometry. Both HIRAD and HIWRAP shared a geometry coordinate system (with a moving origin at the Global Hawk 3D location); but NEXRAD was fixed (ground-based) with the origin at the radar antenna. Since all three datasets had to be collocated, the selection of the HIRAD grid became the most advantageous choice, which is described next.

The HIRAD data are organized into the Hierarchical Data Format (HDF5) [13]. This format creates a multi-dimensional file comprised of "stacked" 2D matrices, with each matrix for a different parameter (e.g., Tb (5, 6 & 6.6 GHz), time, EIA, latitude, longitude, etc.), all of which are located on the earth's surface. A data vector of desired parameters is generated by selecting a row index and column index and "drilling-down" through the multiple layers to select parameters of interest.

For HIRAD, the matrix rows are the "HIRAD scans" and the matrix columns are the HIRAD beam #'s. Through-out this dissertation, images of parameters (e.g., Tb) are presented using the MatLab command "imagesc(par)", where "par" is the parameter of interest. It should be noted that the geolocation of the HIRAD surface pixels are the intersection of line of sight vectors from the aircraft in the cross-track plane with the earth sphere. It is important to note that the distance from the nadir point to a given beam surface pixel are arc lengths, which are not linear with beam#. Therefore, the matrix image displayed is NOT a true geometric project of the surface parameter such is seen in a photograph. The distortion is small over the central portion about the

matrix center (separation between beams ~ 0.1 km) and becomes increasing greater at the swath edges (separation between beams ~ 0.15 km). There is no distortion in the along-track direction with the separation between scans ~ 0.15 km. Where geometric fidelity is important, the images are produced using the "turbo-scatter plot", which uses the latitude and longitude for the pixel location and color for a representation of the parameter value.

Since the geolocation of the HIRAD, HIWRAP and NEXRAD datasets are 3D, we use the HIRAD grid to collocate these data spatially. The HIRAD grid (right-hand coordinate system) is shown in Figure 3-1, where X corresponds to HIRAD beams, Y corresponds to HIRAD scans and Z is altitude, which corresponds to the center of the HIRAD radiative transfer model 39-layers (0.25 to 19.75 km with a step of 0.5 km). For illustrative purposes, the grid points in the YZ-plane are shown for every 5th scan and for only 5-beams. For the Global Hawk second pass, the matrix size was (321 beams x 661 scans x 39 RTM layers), and NEXRAD RR's were resampled (interpolated) to fill the respective matrix before analysis was performed.

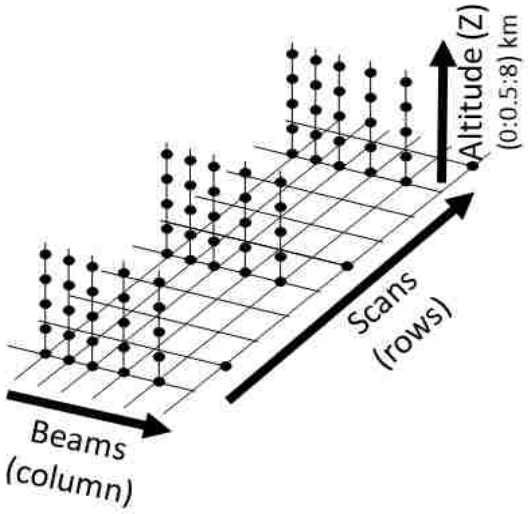

Figure 3-1: HIRAD geolocation grid (decimated to show every 5th scan and only 5 beams). Matrix dimensions (661 x 321 x 39).

3.2 HIWRAP Measurement Geometry

The HIWRAP used a single (Ku-band) conical scanning pencil-beam (3°) parabolic reflector antenna that produced a circular pattern on the surface, as shown in Figure 3-2. As the UAV flew along a straight and level flight line at a nominal altitude of 18 km, the distance to the surface (slant range = 23.5 km) was constant, and the antenna cone angle was 30° that resulted in approximately an earth incidence angle (EIA = 30°) and an "effective" (two-way) antenna instantaneous field of view (IFOV = 0.54 km cross-track x 1.09 km along-track). The orientation of the IFOV changed with azimuth scan angle as seen in Figure 3-3, but the IFOV dimensions were constant.

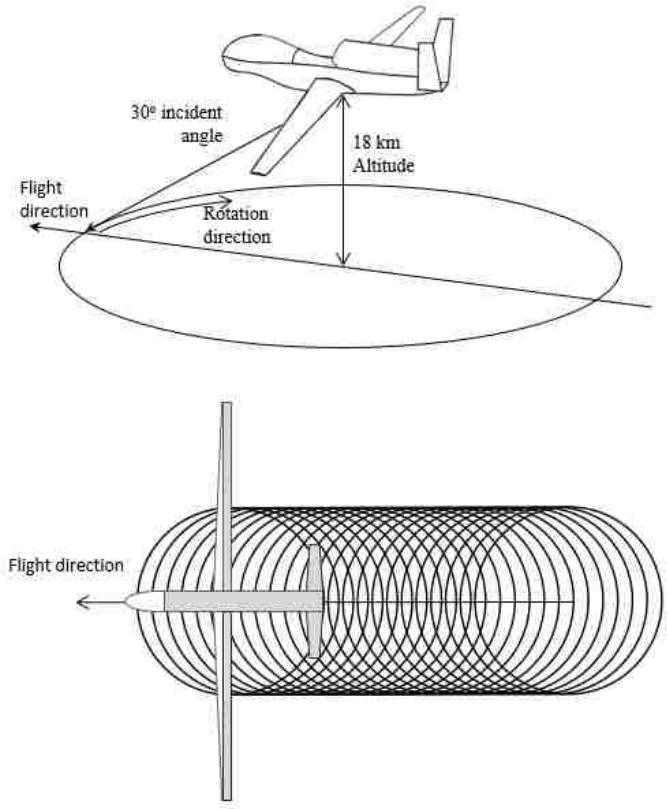

Figure 3-2: HIWRAP conical scanning geometry.

For each radar transmitted pulse, the rain backscatter power was captured in 75 m range gates (RG) from the aircraft to the surface, and multiple pulses were averaged to provide estimates of the volumetric radar cross section ("Z" in units of m^2/m^3). Therefore, at fixed slant ranges (constant altitudes), planar 2D images of echo reflectivity were produced with a semi-circular raster-scan pattern (note that forward and aft-looking measurements were separated into different data sets).

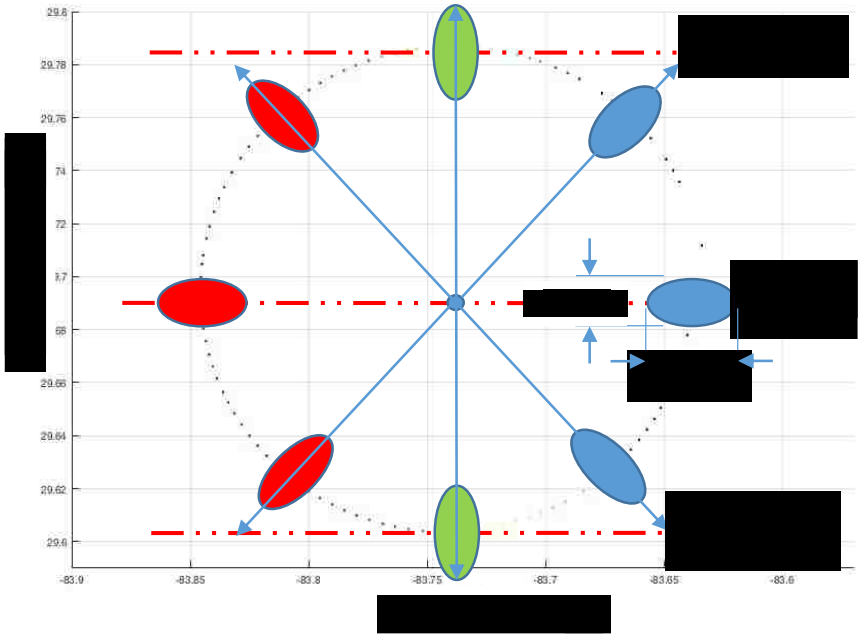

Figure 3-3: HIWRAP IFOV orientation for several HIRAD beam positions.

However, this idealized geometry rarely happened because the Global Hawk UAV continuously experienced attitude changes in roll, pitch and yaw during flight, and as a result, the antenna spin axis did not always point in the nadir direction that produced small but significant perturbations in the idealized circular scan surface locus. Fortunately, the UAV on-board inertial navigation system continually measured the altitude, heading, and attitude, which were input the

geolocation software, provided by the NASA GSFC [14], to calculate the instantaneous slant range of the surface echo and the corresponding surface pixel geolocation centroid. These data were merged into the HIWRAP data product ("hs3_hiwrap_kuinnerchirp_2013Sep16_021927-024604") to provide the necessary parameters for analysis (see Table 3-1).

Table 3-1: HIRAD Parameters

Variable	Description
Year	Year the data was collocated
Freq	Frequency of the radar
Tilt	Antenna cone angle
Gatesp	Range gate spacing
Roll	Aircraft roll angle
Pitch	Aircraft pitch angle
Head	Aircraft heading
Sgate	Surface range gate
Rang	Radial distance of pulse center from radar
azi	Azimuth position of the beam

3.3 Spatial Collocation of HIWRAP and HIRAD

The HIWRAP data came in polar coordinates, where measurements (pixels) were represented by range and antenna rotation angle (azimuth), but since the objective was to combine HIWRAP and HIRAD observations, these data were reshaped to the HIRAD 3D grid spatial format (see Section 3.1) in a two-step process. First, using the HIWRAP flight geometry (altitude, tilt, roll, pitch, heading, and aircraft sub-point geolocation), data were extracted for fixed RG locations (representing a constant altitude surface) and were converted into Cartesian coordinates, where a measured radar backscatter was represented by longitude, latitude and fixed altitude (known as

"raw" or "native" format). Next, these radar measurements were optimally interpolated into the 3D spatial HIRAD grid, which resulted in a HIWRAP reflectivity matrix used for analysis.

For the geolocation error analysis, we chose the HIWRAP surface RG (where the maximum reflection occurred), which was nominally RG# 277. Further, since HIWRAP was a conical scanning radar, we generated forward (fore-) and rearward (aft-) looking datasets for analysis, which were separated based on the rotation angle, where forward was defined as the measurements between azimuth < 90° and > 270° and rearward data was the measurement within radar azimuth > 90° degrees and < 270°.

Further, since the HIWRAP rain reflectivity comparisons with NEXRAD was performed at a spatial resolution of ~ 0.5 km, we gridded and averaged these HIWRAP data on constant altitude layers (surface to 10 km altitude) for comparison.

3.4 HIWRAP Geolocation Analysis

For satellite and airborne microwave radiometer imaging, knowledge of antenna pointing plays a significant role, therefore analysis techniques have been developed by the microwave remote sensing community to maintain a high level of accuracy. Satellite orbit (aircraft flight path) uncertainties, antenna pointing misalignment and aircraft attitude are some of the factors that play a role in the geolocation accuracy, which can cause differences in water/land boundaries between the measurement geolocation compared to high resolution map coordinates. One common method, to determine the geolocation accuracy, is to use the surface microwave measurement images and to calculate the corresponding derivative (rate of change of intensity) at the water/land regions. See Appendix-A for further details.

3.4.1 Land/Water Boundary Location Procedure

For HIRAD, Sahawneh [15] applied a similar method and compared the 5 GHz Tb images of land/water crossings to high-resolution maps to determine the geolocation accuracy. His analysis used the approach of Clymer et al. [16], which estimated the beam pointing error for the 8-beam antenna of the Microwave Radiometer (MWR) on the AQ/SAC-D satellite.

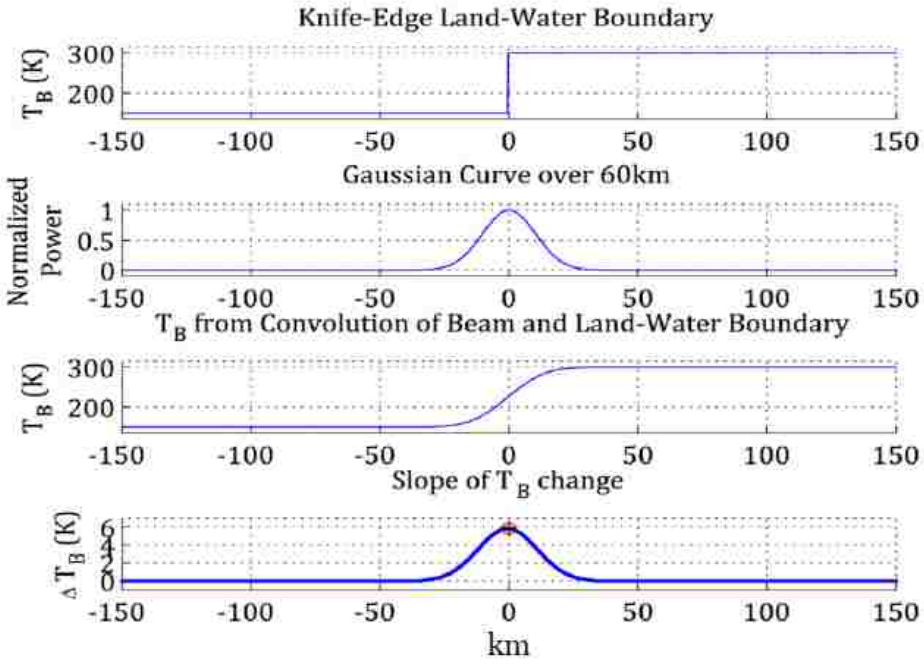

Figure 3-4: Convolution of a theoretical "knife-edge" land/water boundary with an ideal 1-dimensional Gaussian antenna pattern. The lower two panels are brightness temperature and brightness slope (figure from Clymer et al. [16]).

Clymer's analysis was based upon a simulation performed using a Gaussian antenna pattern to model the observed brightness temperature (Tb), when passing over a step function water/land boundary as shown in Figure 3-4. The first panel shows the modeled water/land feature where lower Tb level represent water (150 K) and the higher Tb level represent the land (300 K). The second panel shows the normalized Gaussian antenna pattern, and the third panel shows the

result of the convolution between the antenna pattern and the simulated Tb (step function). Last panel shows the derivative (slope) of the modeled Tb, where the maximum absolute slope appears where the antenna beam filled equally by water and land. It should be noted that this approach is robust and insensitive to the antenna beamwidth. Thus, this geolocation technique compares the location of the maximum absolute slope with the corresponding land/water boundary location of a high-resolution map.

3.4.2 Google Earth Comparison

Based upon the above section discussion, an evaluation of the geolocation of the HIWRAP surface echo pixels with a high-resolution Google Earth Map was performed. Specifically, we performed an analysis of the HIWRAP surface reflectivity image of the northern Florida peninsula as the Global Hawk flew from the Gulf of Mexico to the Atlantic Ocean exiting over the city of Jacksonville, which is shown in Figure 3-5. The HIWRAP surface reflectivity image (dB in the resampled HIRAD grid format) showed several water/land boundaries (lakes, rivers and ocean coastline) where the geolocation comparisons were made.

Consider now, the differences between HIWRAP surface reflectivity in the native and HIRAD grid formats presented in Figures 3-6 and 3-7. In Figure 3-6, the reflectivity contrast between land and water are improved in the HIRAD format, which is an advantage that enhances the intensity slope (derivative). The reason is more evident as illustrated in Figure 3-7, which shows an expanded view of the pass over Lake Sampson. Note that each radar measurement is color coded using the dB scale on the right-hand side. In the upper image (native format), we can see a reduced density of radar measurements (pixels) that occur along conical arcs as compared to the resampled HIRAD grid along straight scan lines. At the left-hand side of the figure, the locus

of 3 scan arcs are shown in the upper panel, and the corresponding locus of 6 HIRAD scans are shown in the lower panel. Also shown are the HIWRAP IFOV's as a red ellipses about the measurement pixels (native format), which show continuous radar spatial sampling in both the along-track and cross-track dimensions. Also shown as the bold "circle pattern" is the land/water boundary for Lake Simpson. Note that the diameter is 3 – 4 IFOV's, which allows the lake to be readily resolved in the radar reflectivity image.

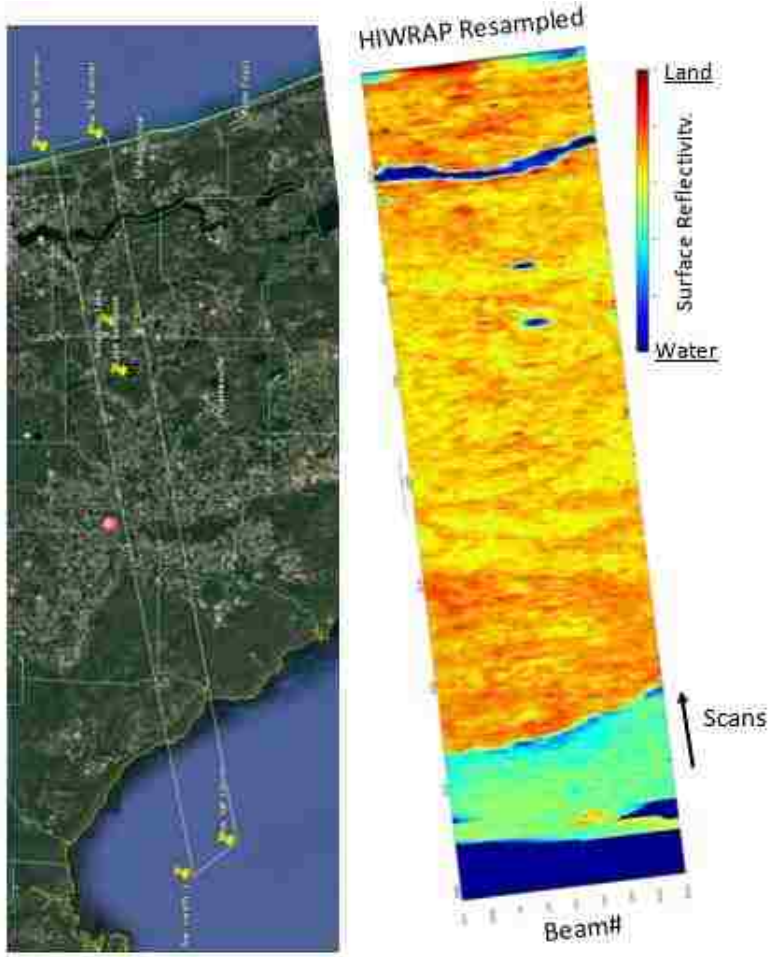

Figure 3-5: Global Hawk pass over North FL (Google Earth – left side) with the HIWRAP swath of surface reflectivity indicated in false color image (right side).

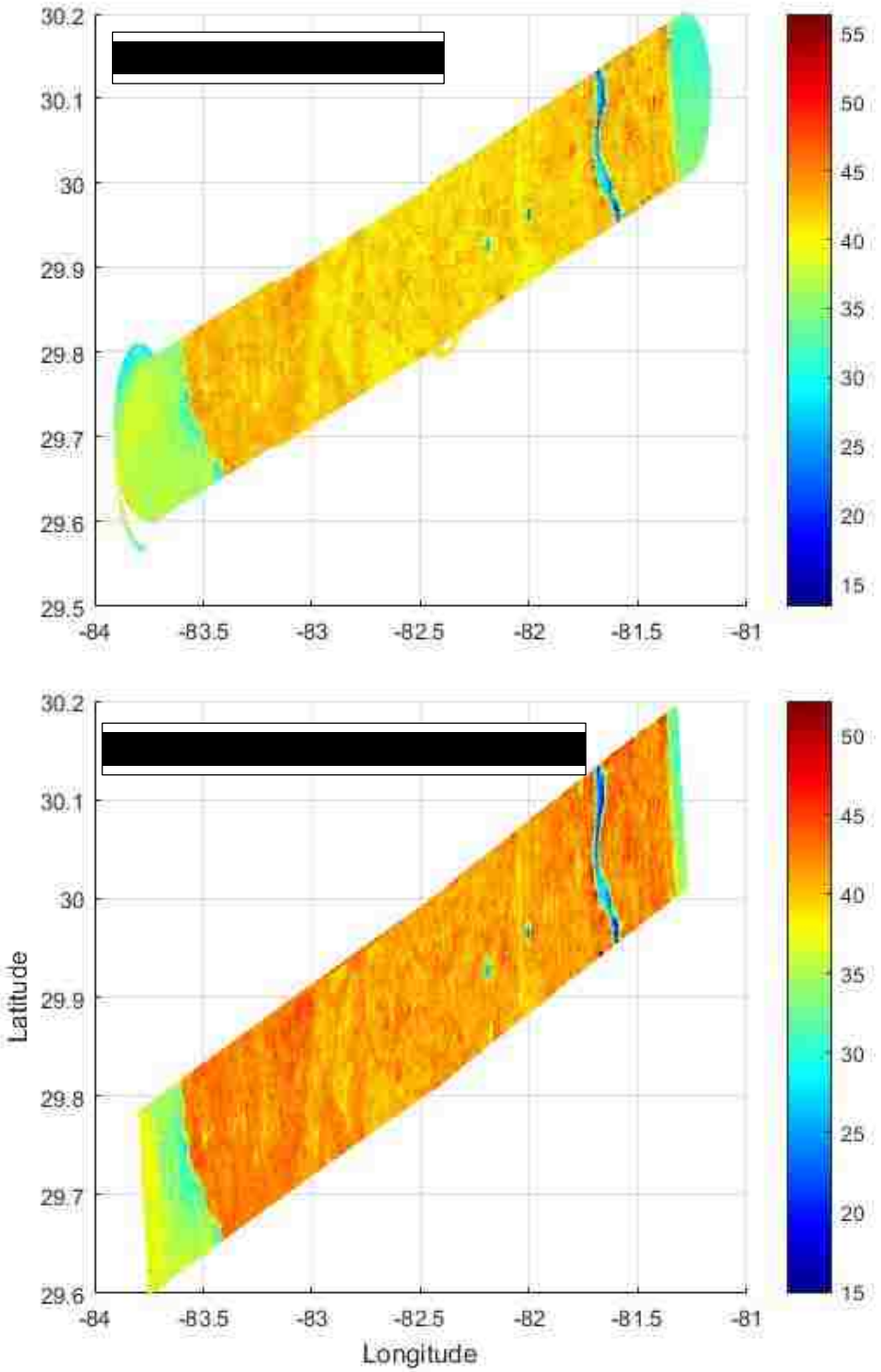

Figure 3-6: Comparison of HIWRAP surface reflectivity image in Native and HIRAD grid formats.

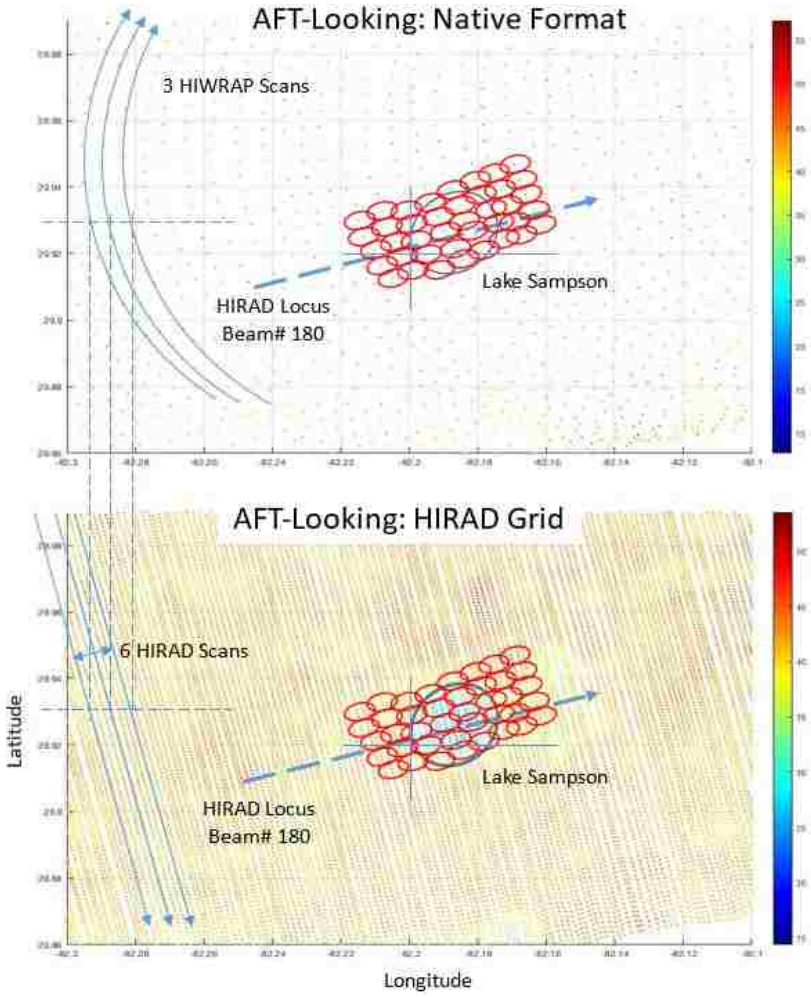

Figure 3-7: Comparison of HIWRAP surface reflectivity image in Native and HIRAD grid formats.

3.4.3 Selection of Geolocation Targets

Next, The HIWRAP data, resampled to the HIRAD grid and smoothed using a low-pass filter, were analyzed using the time series along a fixed beam position for the transition over land/water boundaries that occurred during the transit of the Global Hawk across the Florida peninsula from the Gulf coast to the Atlantic Ocean.

Consider first Figure 3-8 (upper panel) that shows the geolocation test area in the blue dashed box. Note that there are 4 land/water features (2 lakes, St Johns River and the Atlantic Ocean coast), where the analysis was performed. There is an excellent qualitative agreement between HIWRAP reflectivity image (lower-left) and the high resolution Google Earth map (lower-right).

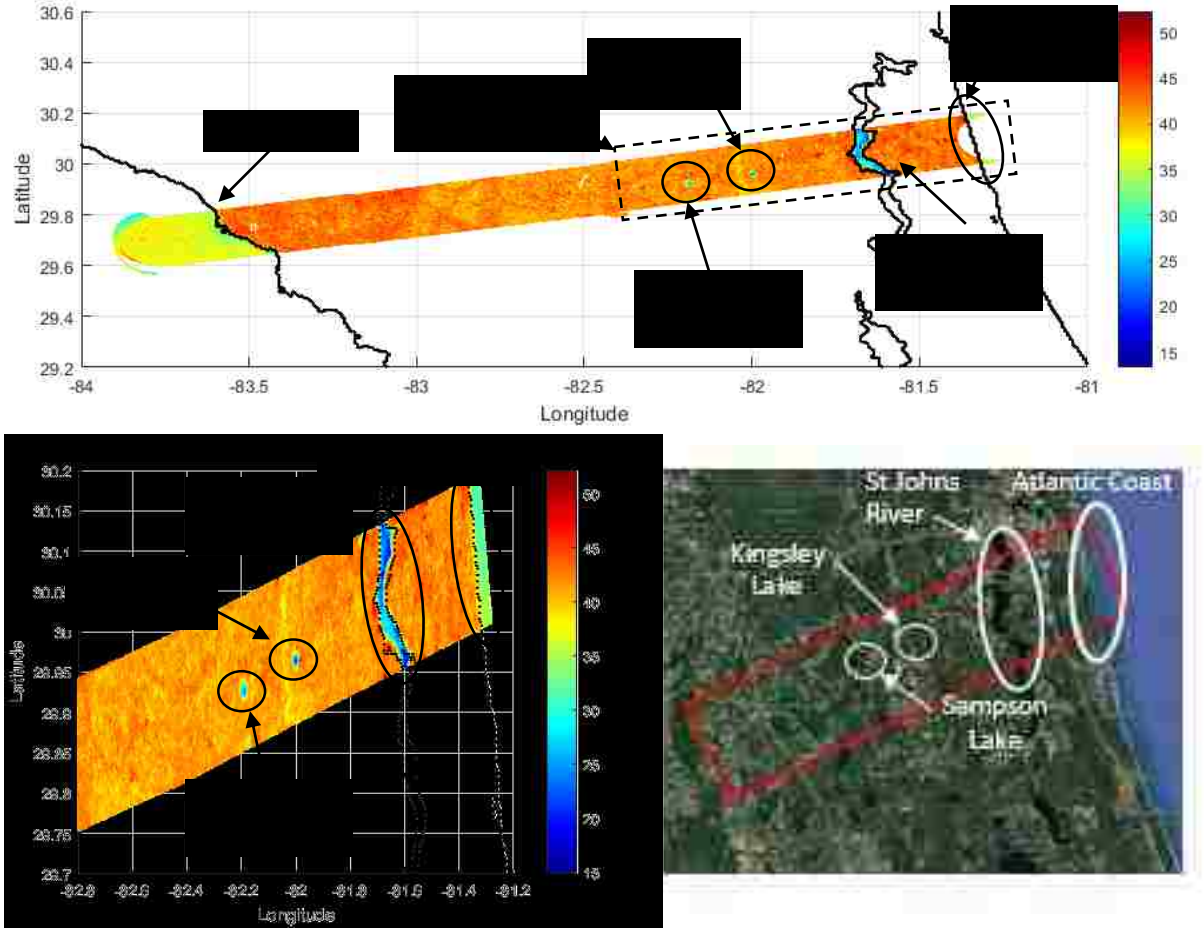

Figure 3-8: HIWRAP swath across north Florida (top), and expanded image for the water/land features using the high resolution HIWRAP surface reflectivity image (bottom-left) and corresponding Google map (bottom-right).

Next, we expand Figure 3-8 to show the images between HIWRAP reflectivity image (lower-left) and the high resolution Google Earth map (lower-right).

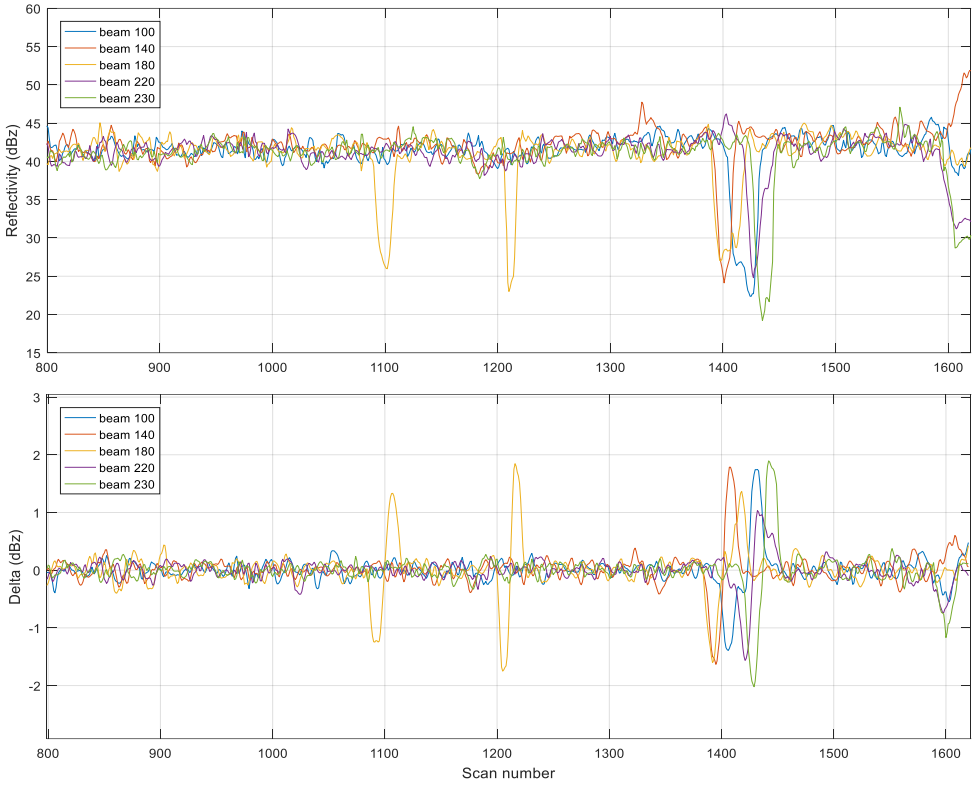

Figure 3-9: HIWRAP surface reflectivity (upper) and reflectivity-slope (lower) time series for multiple HIRAD beam positions.

Following the Clymer procedure, the geolocation analysis was performed as a function of the HIWRAP azimuth scan angle, which maps into HIRAD beam # after resampling. For example, in Figure 3-9 top panel, we display a time series plot of HIWRAP surface reflectivity (dB) for multiple beam #'s (100, 140, 180, 220 & 230), and note that the x-axis is HIRAD scans (sec). The land reflectivity is typically +42 dBz, but occasionally the value drops < +30 dBz, when the IFOV passes over water (scan # 1100, 1215, 1390-1430 and 1590). The corresponding reflectivity slope

(first derivative) time series is plotted in the lower panel, where the peak slopes correspond to the HIWRAP observed water/land boundaries locations, and the polarity of the peak (positive or negative) represent the IFOV transition order (water to land or land to water) respectively.

3.4.4 Accuracy Assessment

The first example is the geolocation error estimation for beam # 140 at the St. Johns River that is presented in Figure 3-10. In the left panel, the maximum negative slope corresponds to HIWRAP's IFOV crossing of the St. Johns River. Next, this associated location (lat/long) of the max reflectivity slope is then marked on the Google map to determine the collocation error, which results in a difference of 514 m using the measuring tool of Google map as illustrated in Figure 3-10 right panel.

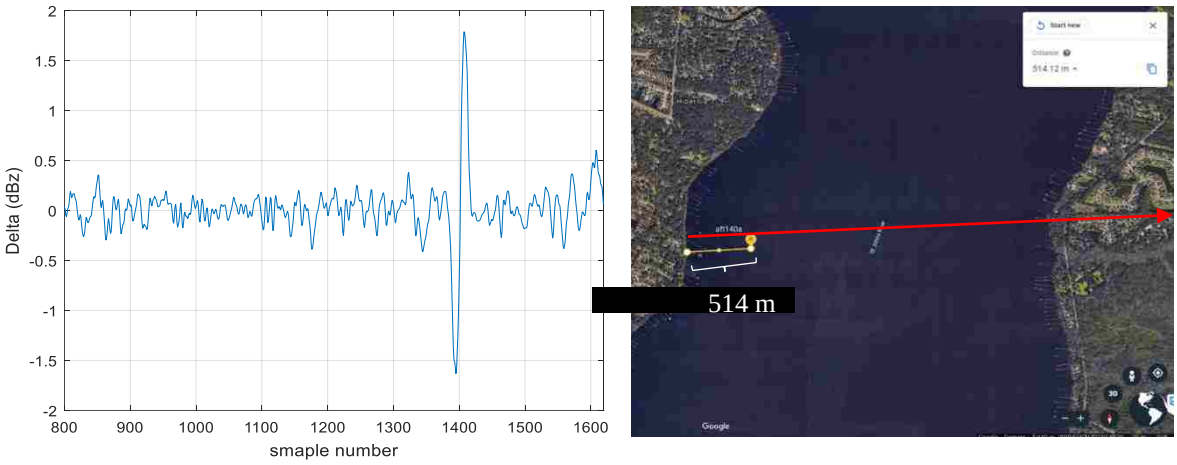

Figure 3-10: Geolocation estimation for beam #140 over St. Johns River.

The same procedure is also performed with the other water/land features lakes (Sampson and Kingsley) and the Atlantic Ocean coast line. The geolocation error for HIWRAP beam # 180 is measured at these bodies of water, and the Figure 3-11 shows the fore- (blue) and aft-look (red) reflectivity slope time series in the (top panel) and the corresponding position within the

HIWRAP swath (bottom panel). Note the excellent alignment of the fore- and aft-looking pixels in the HIWRAP image, which yield nearly identical results (geolocation errors).

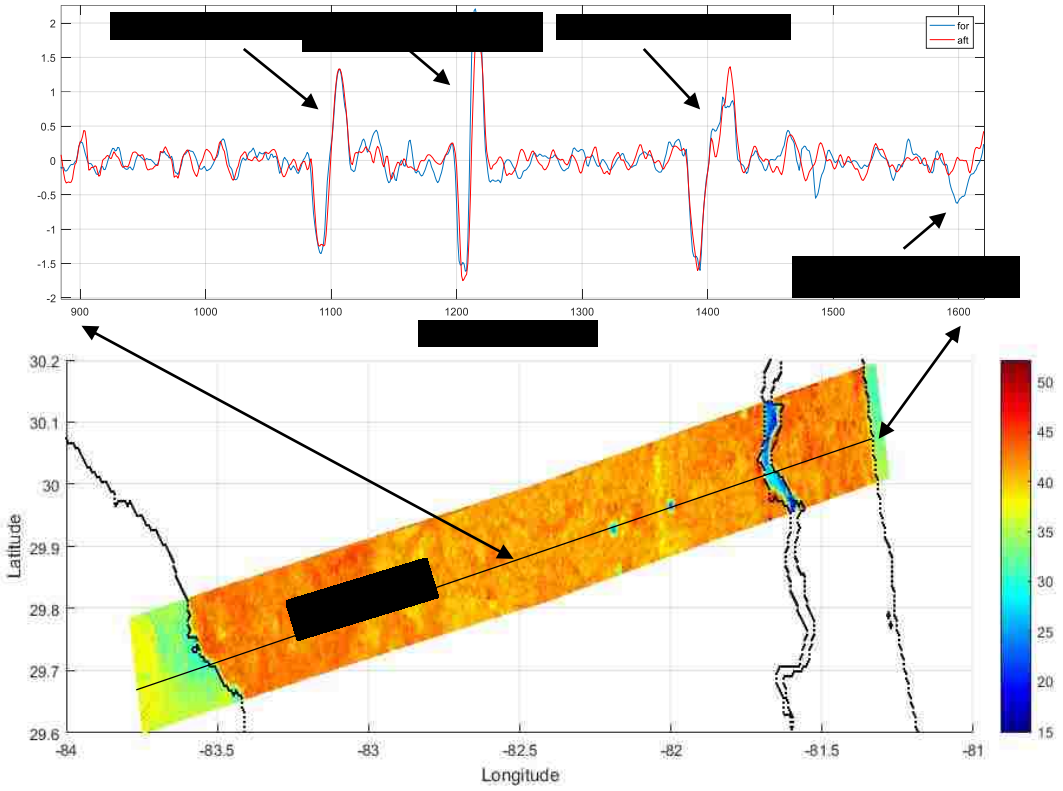

Figure 3-11: Time series of HIWRAP fore- and aft-looking reflectivity slopes for beam # 180.

Another example is shown for Lake Sampson in Figure 3-12, where the lake boundary is close to circular with a diameter of ~ 3 km. For this case, the measurements occurred at 10 beam positions (equally divided between fore- and aft-looks), which were selected to cover most of the Lake. In this figure, the locations of the max slope points are shown by yellow markers on the Google map. Also, for this case the reflectivity slopes were calculated both along-track and cross-track to ensure accuracy of the evaluation. Results for comparisons for Lake Sampson, St John' River and the Atlantic Coastline are presented in Table 3.2, 3.3 and 3.4 respectively.

Figure 3-12: HIWRAP geolocation analysis for Lake Sampson. Yellow markers are the location of the maximum reflectivity slopes.

Table 3-2 HIWRAP Geolocation Offsets for Lake Sampson

Position/Beam	Offset (m)
L1	874
L2	502
L3	978
L4	1160
L5	231
L6	832
L7	782
L8	0
L9	334
L10	688

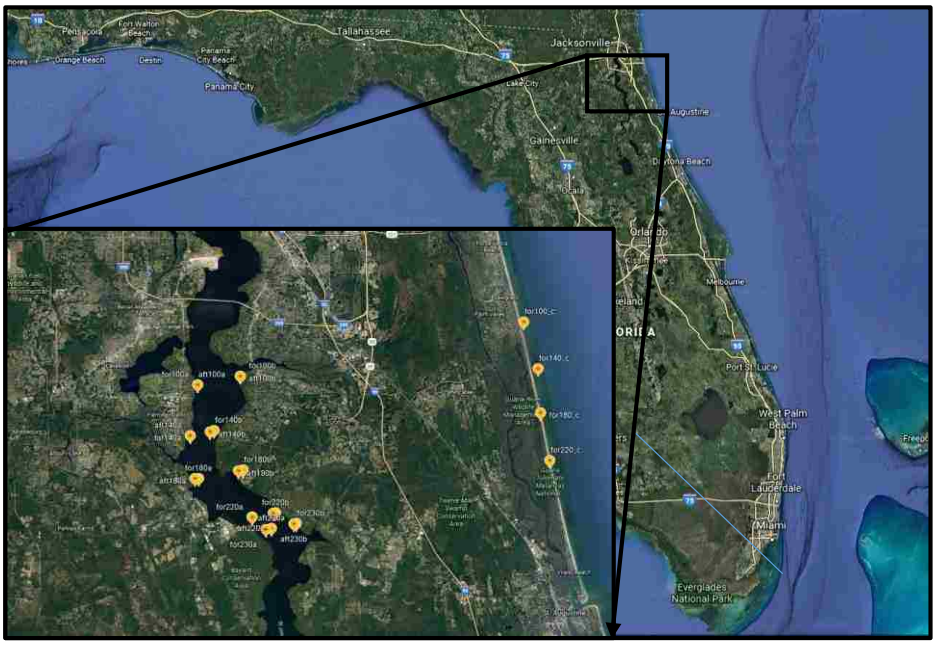

Figure 3-13: HIWRAP geolocation analysis for St Johns River. Yellow markers are the location of the maximum reflectivity slopes.

Table 3-3 HIWRAP Geolocation Offsets for St Johns River

Position	Offset (m)
R1	295
R2	0
R3	700
R4	-456
R5	228
R6	270
R7	367
R8	-83
R9	264
R10	472

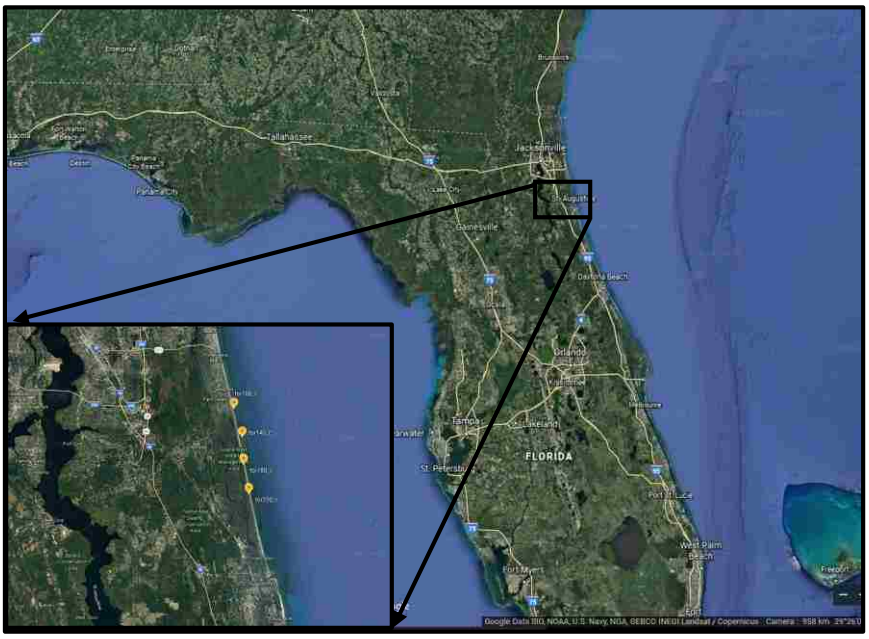

Figure 3-14: HIWRAP geolocation analysis for Atlantic Coastline. Yellow markers are the location of the maximum reflectivity slopes.

Table 3-4 HIWRAP Geolocation Offsets for Atlantic Coastline

Position	Offset (m)
C1	105
C2	545
C3	-135
C4	-183

Figure 3-15 presents a histogram of the geolocation errors for the combined lake, river and ocean crossings. Results are within ±1 km, regardless of water/land features and independent of the HIWRAP azimuth position; however, note that this reflectivity slope technique has a small positive bias (away from land). The mean of the histogram is 401.1 m and the standard deviation

is 364.3 m. Unfortunately, there is no empirical assessment for geolocation accuracy within the atmosphere, where the cross-correlation of NEXRAD and HIWRAP rain pixels occurs, but, based upon geometric calculations, we expect that the relative geolocation accuracy would be the same. Thus, giving that the NEXRAD has a resolution of 1 km, this HIWRAP geolocation error is quite acceptable for joint analysis.

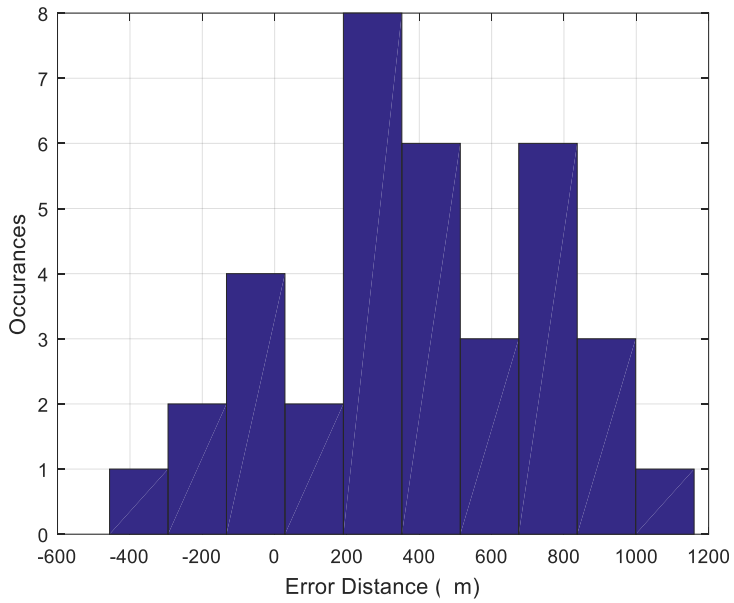

Figure 3-15: Histogram of combined lake, river and ocean geolocation offsets (errors) for various HIWRAP azimuth looks.

CHAPTER 4:
HIWRAP REFLECTIVITY AND RAIN RATE TUNING WITH NEXRAD

On September 16, 2013 (GMT: Sept. 16 @ 01:37), a tropical squall-line of thunderstorms was observed simultaneously by the remote sensors on board of the Global Hawk aircraft (HIRAD and HIWRAP) and the ground-based NEXRAD's at Tampa and Tallahassee, Florida. This was a serendipitous event that provided the important tropical precipitation observation dataset, which is a major part of this dissertation. What was unique about this experiment was the combination of the HIWRAP airborne radar (see Section 2.3) and calibrated ground-based radars (see Section 2.4) that simultaneously viewed an intense squall-line rain event with uniform moderate wind speed conditions. Since HIWRAP did not provide a RR product, we used the raw reflectivity product to derive RR, which was adjusted to match the collocated NEXRAD precipitation measurements (surface truth standard). This was advantageous to this dissertation because both HIWRAP and NEXRAD radars provided the independent "rain rate surface truth" for the validation of the HIRAD rain retrieval, which is presented in Chapter 6.

4.1 Tallahassee NEXRAD Rain Coverage

Because the Tallahassee NEXRAD (KTLH) was closer to the location of the Global Hawk (GH) path, its volume scan provided observations that were nearer to the surface (see Table 4.1) and with higher spatial resolution than those of the Tampa NEXRAD. Closer range is important because the radar antenna beam cross section of the NEXRAD rain volume increased with the target range, and the KTLH provided the best geolocation match with the high-spatial resolution HIWRAP pixels. Figure 4-1 shows the Level-1 (base-scan) Tallahassee radar reflectivity product

(Constant Altitude Plan Position, CAPI) that is displayed using the Weather and Climate Toolkit; where the right panel contains the details of the measurement, including date, time and the reflectivity color scale in dBZ. The figure also shows a rectangle that corresponds to the HIWRAP measurements swath, which ranges from 170 to 250 km from NEXRAD location, at ~200 degrees azimuth relative to North that was used for the colocation procedure.

Table 4-1: NEXRAD Refracted Beam Altitude for Volume Scan Elevations.

NEXRAD Elevation	Center of Beam Altitude (km)	@ Range (km)
Level 1	1.55	197.5
Level 2	2.91	197.6
Level 3	4.43	197.6
Level 4	6.10	197.7
Level 5	8.23	197.8
Level 6	10.66	198.0
Level 7	13.71	198.3
Level 8	17.53	198.6

The Tampa Bay Rain Experiment comprised three GH passes over the squall line (shown in Figure 4-2), while the storm was moving rapidly to the north-west during the measurement. It is important to note that this NEXRAD image corresponds to the beginning of the GH second pass.

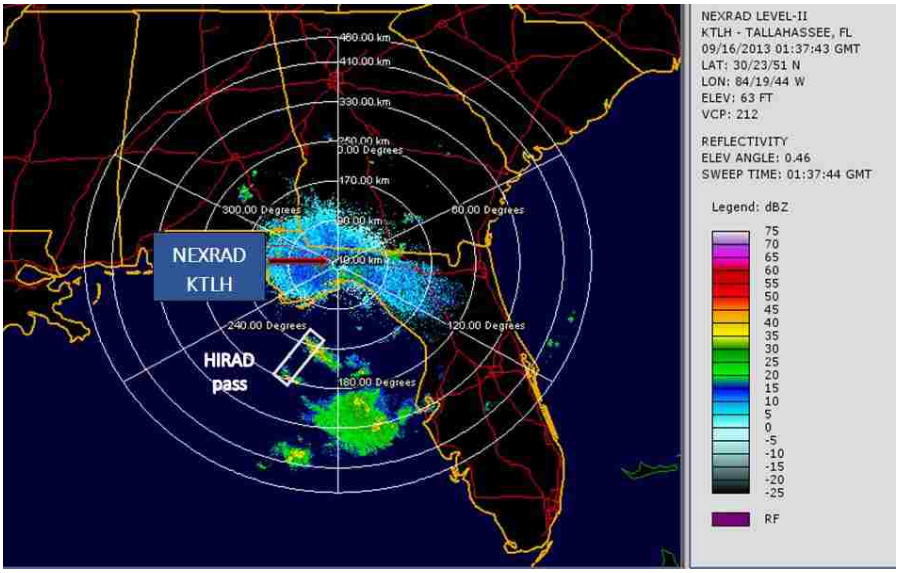

Figure 4-1: Tallahassee NEXRAD (KTHL) base-scan radar reflectivity CAPI image for the tropical squall-line rain event (Tampa Bay Rain Experiment).

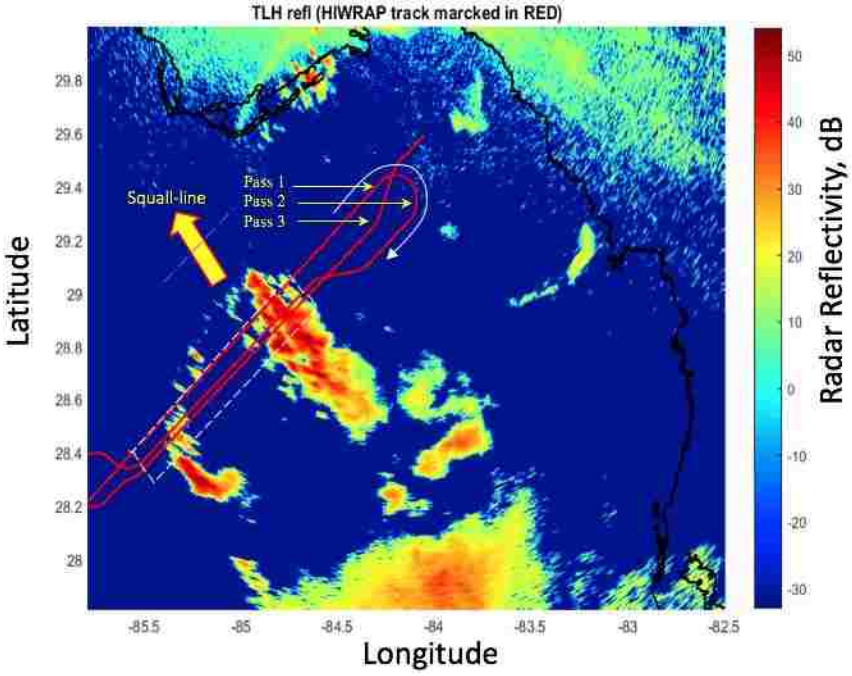

Figure 4-2: Expanded view of NEXRAD/HIWRAP geolocation over the tropical squall-line for level-1 of volume scan-14. White dashed box is the HIWRAP swath, and the direction of the squall-line motion (NW) is indicated by the yellow arrow.

The motion of the squall-line is shown in Figure 4-3 during the next ten minutes elapsed time between two volume scans, V-14 lower panel and V-16 (closest in time with the second pass) in the middle panel (imagesc format). The rain feature was a very dynamic event that changed in shape and intensity as it propagated rapidly to the North-West, which is captured in the differential image (top panel).

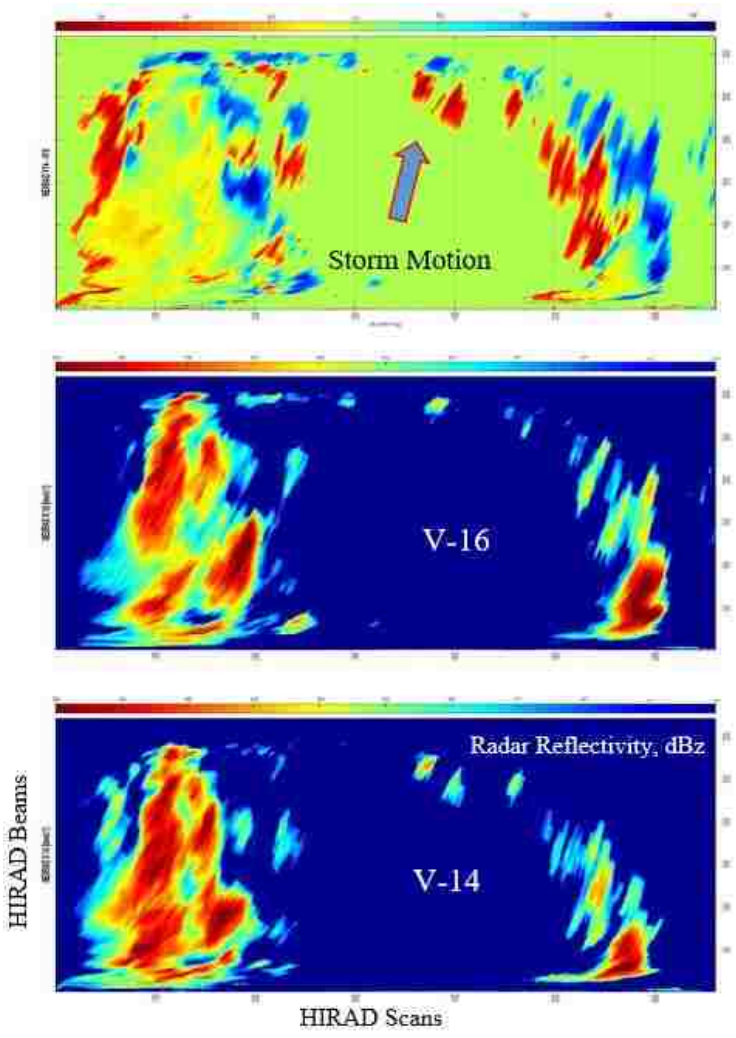

Figure 4-3: NEXRAD level-1 radar reflectivity patterns (imagesc format & color scale in dBz) for volume scan V-14 (bottom), volume scan V-16 (center) and differential image of (V-14 minus V-16) (top image). The arrow in the top panel indicates the direction of the squall-line motion, and note that the horizontal axis is HIRAD scans and the vertical axis is HIRAD beams.

Also, this can be seen in Figure 4-4, in the foreward-looking radar reflectivity images for the three Global Hawk passes. The second HIWRAP pass (heading South-West) was selected for the analysis, as it contained both rain regions, and the structure of the rain provided a larger area of colocations and wider dynamic range of rain for the tuning process.

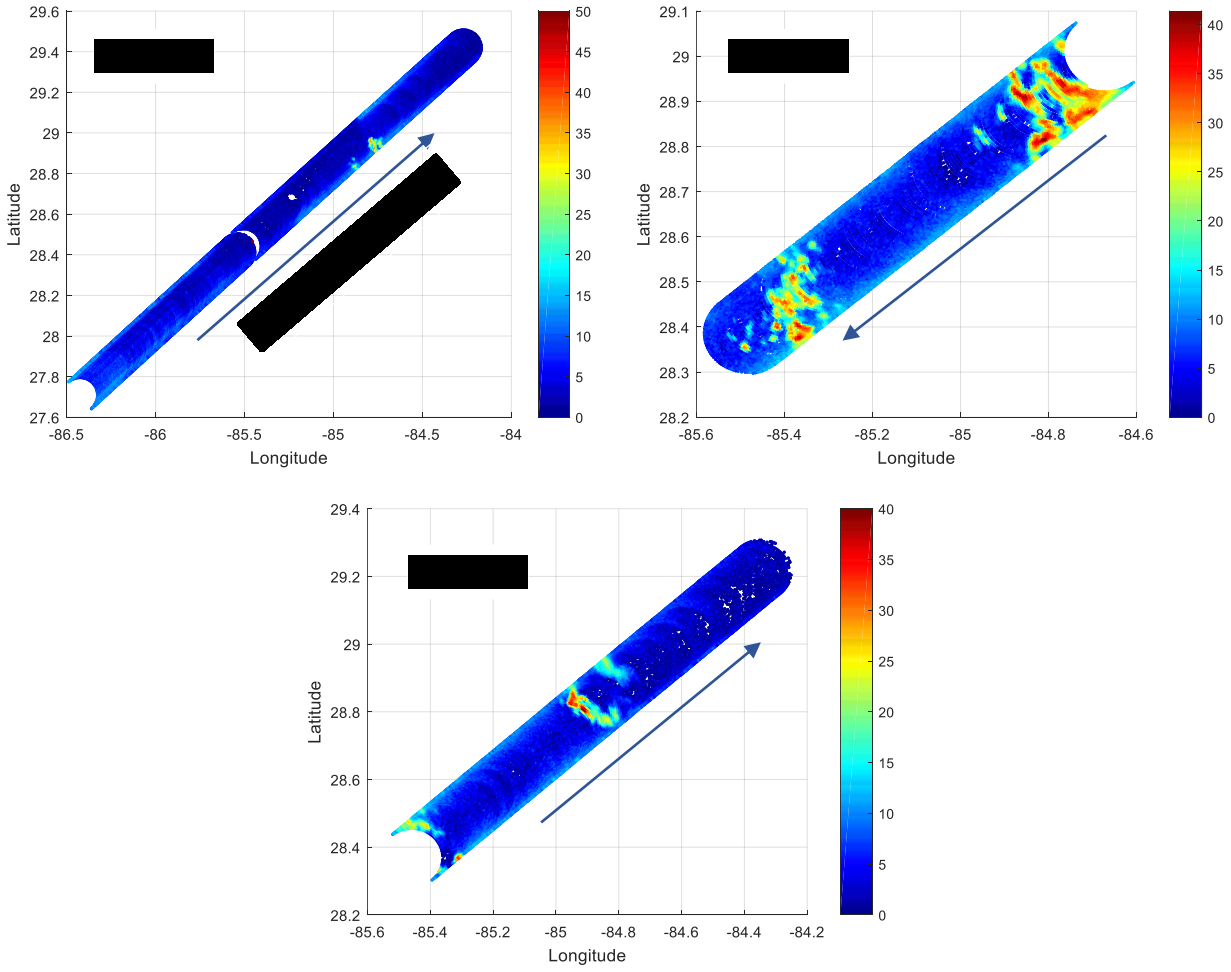

Figure 4-4: HIWRAP forward-look reflectivity images over the three GH passes. Note different latitude and longitude scales for each panel.

4.2 HIWRAP and NEXRAD collocation

Both radars use different line of sight (LOS) measuring geometries, namely: NEXRAD is a ground radar with a near-horizontal propagation path that is refracted through the atmosphere; and HIWRAP is a high altitude, airborne conical-scanner that images the rain along a "straight-line" slant path, from the top of the rain to the surface.

In uniform media, radar electromagnetic (EM) waves propagate in straight paths, but since the earth's atmosphere is not uniform (air density decreases with altitude), the ground-based radar propagation is refracted by the vertical gradient of the atmospheric index of refraction, that results in a curved path toward the earth. For standard atmosphere conditions, the National Weather Service (NWS) supplies beam height calculations at given ranges using a refraction model [17]. In this model, the earth radius is assumed to be 4/3 of its actual radius, and the propagation paths become approximately straight lines. Thus, the altitude of the radar beam center is calculated:

$$h = \sqrt{R'^2 + r^2 + 2 \cdot R'^2 \cdot sin(\phi)} - R' + (h_a - h_r) \qquad (4\text{-}1)$$

where ϕ is the radar antenna elevation, r is range from the radar, *R'* = 4/3*earth radius, and h_a is the height of the radar antenna above the sea level and h_r is the height of the earth surface (above sea level) at the area of interest (note for oceans h_r is zero altitude). Table 4.1 shows the altitude of the refracted beam at the range, corresponding to the geometric center of the "HIRAD BOX" (squall-line rain event) for the different NEXRAD elevation angles (volume scan levels).

The time of the Global Hawk passes over the storm (flight leg) is about 10 – 15 minutes, while NEXRAD requires ~5 minutes to complete one volume scan. A HIWRAP/NEXRAD collocation example is shown in Figures 4-2 and 4-5. The corresponding temporal collocations between HIWRAP/NEXRAD are volume scans "KTLH20130916_013739_V06" and

"KTLH20130916_014717_V06" respectively for the beginning and end of the flight leg-2.

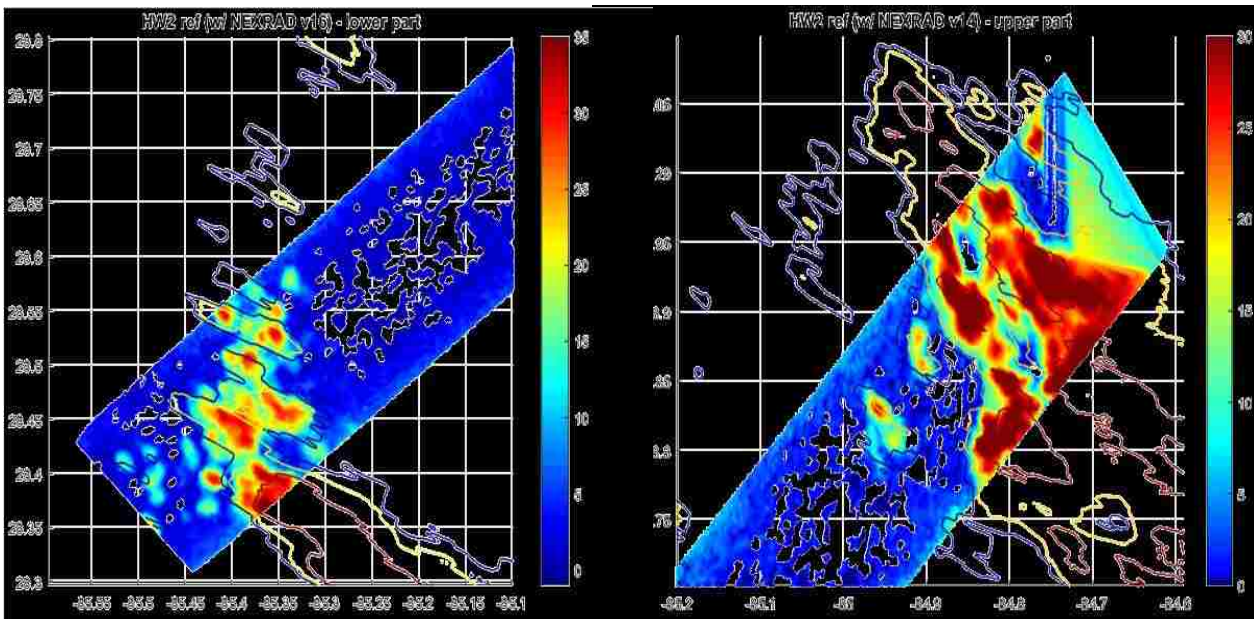

Figure 4-5: HIWRAP rain radar reflectivity @ altitude =1.5 km (volume scan level-1) and corresponding NEXRAD reflectivity contours for second Global Hawk pass (North to South). Note: at the beginning of leg-2 (right panel) corresponds to NEXRAD volume scans #14 and at the end of leg-2 (left panel) corresponds to volume scan #16, which provides best temporal alignment.

Figure 4-5 shows a two-panel CAPI-1.5 km comparison of HIWRAP and NEXRAD reflectivity, where the HIWRAP dBZ image is shown in color and the NEXRAD rain reflectivity is represented by three contour lines, each line representing a different reflectivity value threshold (1, 20 and 40 dBZ). The right-hand panel shows good spatial alignment with the first volume scan (#14) and the left-hand panel (ten minutes later) shows a similar (good) alignment with the other volume scan (#16).

4.2.1 Description of 3D rain volume

As previously discussed in Section 3.2, HIWRAP used a conical scanning pencil-beam (3°) parabolic reflector antenna that mapped out a circular pattern on the surface. As the UAV flew along a straight and level flight line at a nominal altitude of 18 km, the distance to the surface was constant, and the beam incidence angle was 30° that resulted in an effective elliptical instantaneous 2-way field of view (IFOV) = 0.54 km minor-axis x 1.09 km major-axis. Moreover, the rain backscatter power was captured in 75 m range gates (RG) from the aircraft to the surface. Therefore, at fixed slant ranges (constant altitudes), planar 2D images (CAPI) of echo reflectivity were produced with a circular scan pattern.

NEXRAD was a ground-based radar with conically scanning 8.5 m diameter dish antenna (~ 1° beamwidth). The radar measurements were obtained in volume scans, whereby the antenna rotated 360 degrees with 8 different elevation angles (0.5 to 19 degrees). During each antenna revolution (~ 40 sec), the radar reflectivity was measured in polar coordinates (range x azimuth, CAPI format), which was sequential for each radar antenna elevation angle. Base (Level-1) reflectivity data were binned and averaged into range cells that were 1^{o} azimuth resolution by 1 km range resolution, and at the HIWRAP measurement location (range ~ 200 km), the two-way effective radar beam diameter was ~ 2 km. The reflectivity data were sorted in polar coordinates (range and azimuth), along with the antenna elevation angle and the time of each measurement. Details of NEXRAD and HIWRAP geometry were previously discussed in Chapter 2 and 3.

While, the two radars used different geometry (polar coordinates) to image the rain event, they were able to collocate the two measurements at a specific point (same location and altitude relative to the sea surface), and both datasets were resampled to the common 3D HIRAD grid

(Section 3.1). However, it must be noted that the two radars were not simultaneous in time; therefore, the propagating rain cells may be slightly displaced in the two images. For the results that follow, it is not a serious issue, but for the HIRAD collocations (discussed later) is a significant issue that was mitigated. Also, for the radar reflectivity tuning comparisons that follow, an altitude of 1.5 km was selected that corresponded to level-1 NEXRAD data (see Table 4.1).

4.3 Radar Reflectivity (dBZ) Tuning

As the time interval of the HIWRAP second pass (11 minutes) exceeded the time for one NEXRAD volume scan (~ 5 minutes), it was necessary to select 2 of 3 consecutive NEXRAD volume scans ("KTLH20130916_013739_V06" and "KTLH20130916_014717_V06" respectively) that approximately matched the corresponding HIWRAP measurement times for the two rain bands that occurred at opposite ends of the flight line (see Figures 4-2, 4-4 & 4-5). It is important to note that (for a given altitude level) the corresponding NEXRAD measurements over the squall-line occurred over two short-time intervals (< 10 sec. each) that were separated by 10 minutes, but the corresponding HIWRAP rain measurements took about 1 minute each to measure the same region with fore-looking and aft-looking conical.

Since the NEXRAD rain reflectivity product was well calibrated, it was used for the tuning the spatially collocated HIWRAP measurements. Both NEXRAD and HIWRAP CAPI's were sampled in a 1 km cube, and we constructed a scatter diagram to establish the mean cross-calibration between the NEXRAD/HIWRAP rain reflectivity measured in dB units. Note that radar reflectivity is approximately logarithmic with rain rate, which corresponds to a straight-line in a log-Y versus log-X plot.

As shown in Figure 4-6, the resulting mean correlation between HIWRAP and NEXRAD is high; with a slope close to unity (0.98) and with 10 dB bias (HIWRAP lower compared to NEXRAD). The 10 dB bias is reasonable considering that is related to the differences in the measuring geometry (rain volume), operating frequency and the two radar reflectivity measurement calibrations. Regardless, this bias is not significant to this research, as the HIWRAP rain measurements are tuned to the NEXRAD rain rate measurements, that are taken to be the standard. Thus, in the analysis that follows, the HIWRAP reflectivity was adjusted according to the linear regression equation (4.2) before transformed to rain rate.

$$\text{HIWRAP\_adj} = 0.987*\text{HIWRAP\_meas} + 10, \text{dBZ} \tag{4.2}$$

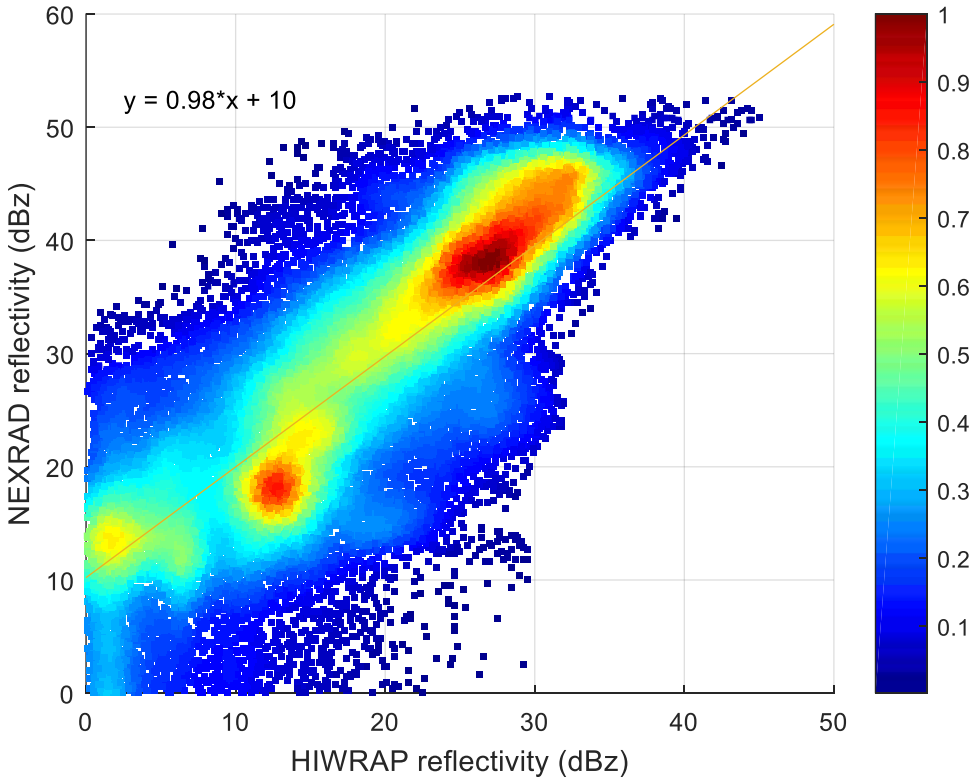

Figure 4-6: Density scatter plot of HIWRAP and NEXRAD reflectivity measurements (dBZ) with linear regression. Color is the number of measurements (warm colors being greater).

4.4 Rain Rate Tuning

It was necessary to define the 3D distribution of rain in the atmosphere, which was the environmental parameter input to the HIRAD brightness temperature radiative transfer model. So, the next step in the analysis process was the radar reflectivity to rain rate conversion for both NEXRAD and HIWRAP, and the adjustment of HIWRAP rain rates (tuning) to match NEXRAD. Since HIWRAP reflectivity was tuned to match NEXRAD, we used the National Weather Service "default NEXRAD Z-R relationship" [18], which is an empirical relationship between reflectivity and rain rate as follows:

$$Z = 300\,R^{1.4} \tag{4.3}$$

where Z is the normalized reflectivity (volume-radar-cross-section/unit volume, $\mathrm{mm}^6\mathrm{m}^{-3}$) and R is the rain rate in mm h^{-1}. This statistical relationship is well accepted within the meteorology science community to yield reasonable rain rates.

Therefore, by applying this Z-R relationship to the NEXRAD volume scan reflectivity data, we produced the corresponding 2D rain rate matrices (CAPI'S) at the fixed altitudes (NEXRAD levels), which were interpolated into the HIRAD 3D rain volume. In Figure 4-7, the corresponding rain rate image (at 1.5 km altitude) is plotted versus the latitude and longitude coordinates (MatLab "turboscat"). Note that this figure produces the true geometric projection of the rain image, which is equivalent to a camera photograph.

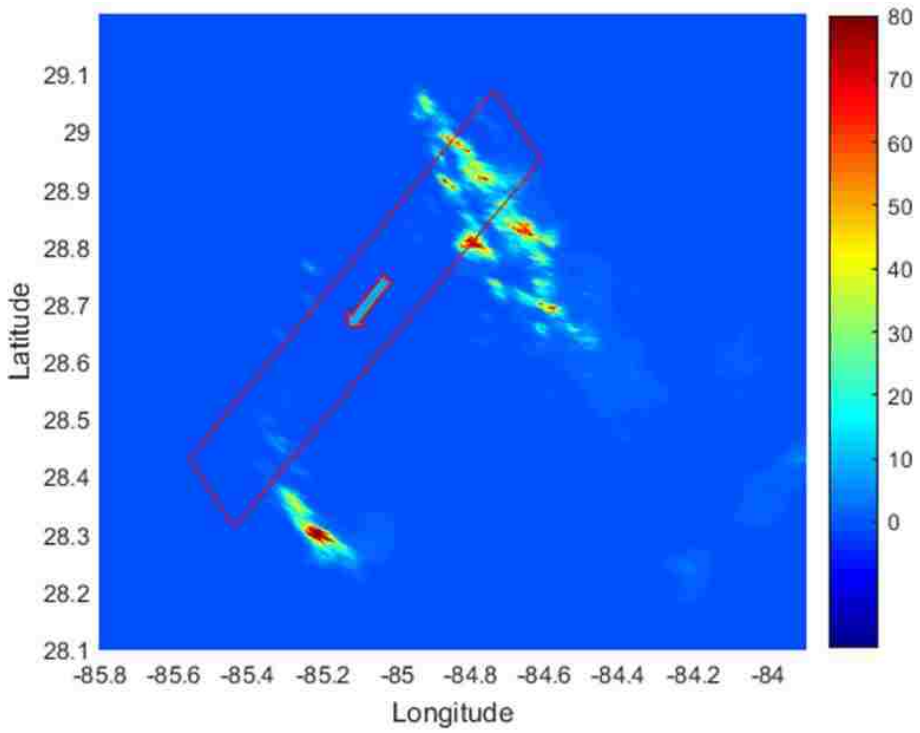

Figure 4-7: NEXRAD rain rate CAPI-1.5 km (volume scan #14) using the default National Weather Service Z-R relationship. The HIWRAP swath is indicated in the red rectangle (flight direction indicated), and the color bar is rain rate in units of mm/h.

Also shown in Figure 4-8 are the corresponding CAPI-1.5km images for NEXRAD (NX), HIWRAP-Fore look (HWF) and HIWRAP-Aft look (HWA) that are displayed using the MatLab matrix plot "imagesc", with HIWRAP measurement swath edges denoted by the red-dashed lines labeled "edge-of-scan (EOS)". Note that these imagesc plots are NOT true geometric projections and that there is a "mirror reversal" in the beam # coordinates (right and left flipped). At first glance, these three images appear to be highly correlated, but the 2D cross-correlation of HWF and HWA with NX yielded low correlation coefficients (only between 25% – 40%), which is probably because the images are not simultaneous and because the rain cells are moving.

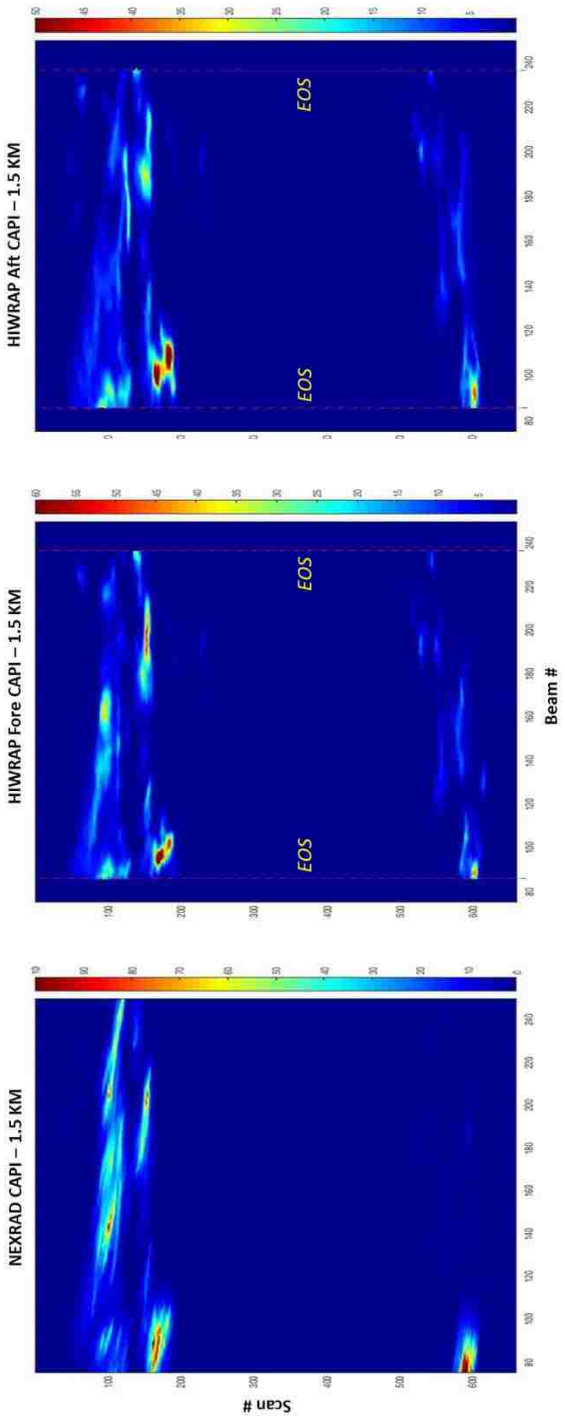

Figure 4-8: Corresponding NEXRAD (bottom) and HIWRAP (middle is forward-looking and top if aft-looking) radar rain rate CAPI's @ 1.5 km altitude and resampled to the HIRAD 3D

grid, where color scale is rain rate in mm/h. Note that these panels (MatLab "imagesc") are mirror images with right/left sides reversed (compared to Figure 4.7).Next, in Figure 4-10, we compared scatter diagrams between collocated (but not simultaneous) NX, HWF and HWA rain measurements. For this purpose, we sub-divided the atmosphere (from the surface to 8 km) into 1 km cubes, which contained all the rain that was observed by HIRAD upwelling and downwelling paths. The collocated NEXRAD and HIWRAP rain rates were averaged in these cubes (pixels) and were plotted in scatter diagrams. The large variance in these plots is indicative of spatial registration problems in the rain features, but overall the mean statistical comparison (linear regression) is reasonably good with ~ unity slopes and small offsets.

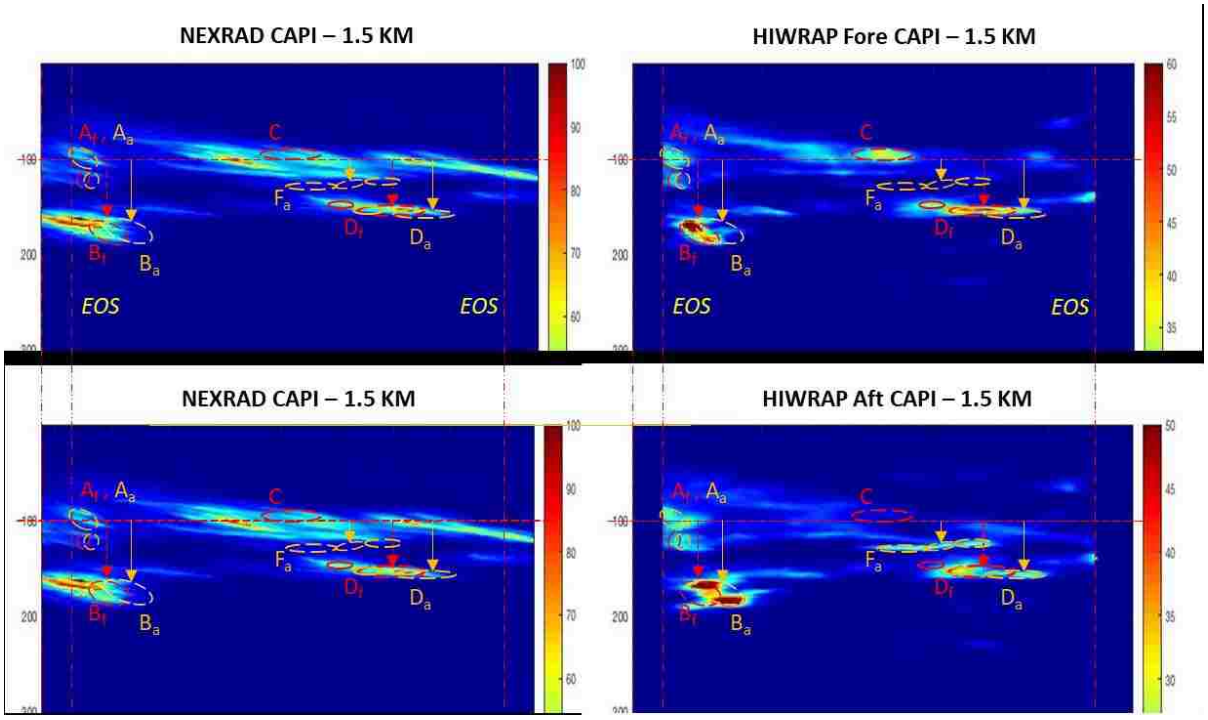

Figure 4-9: Comparison of HIWRAP-Fore, -Aft, & NEXRAD CAPI-1.5km with rain features as colored ellipses (fore = red & aft = orange) and color scale is rain rate (mm/h).

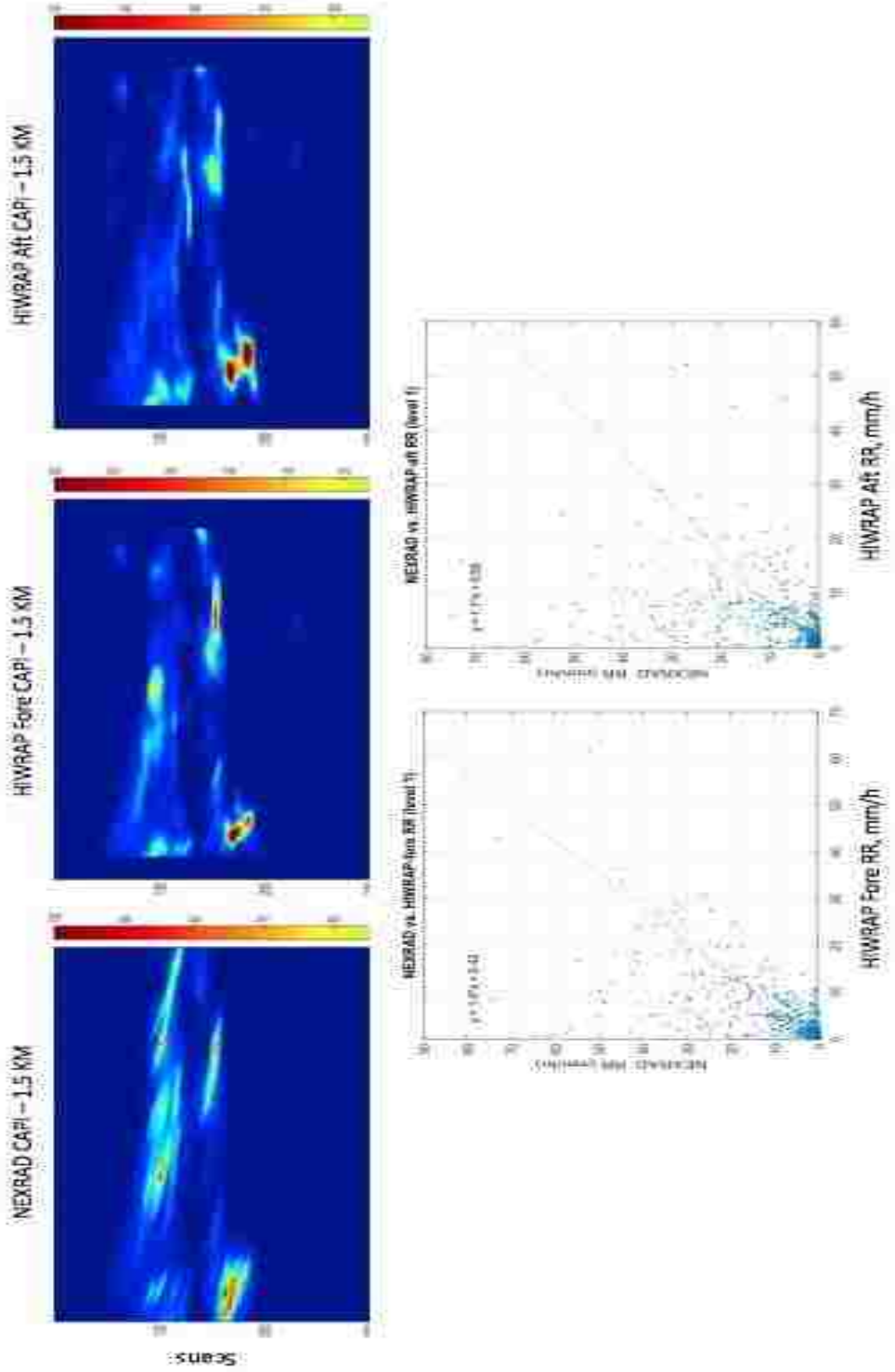

Figure 4-10: HIWRAP rain rate cross-correlation with NEXRAD for CAPI-1.5km.

Next, we present more HIWRAP rain rate comparisons with NEXRAD volume scan level-2 (CAPI-3.0km) in Figures 4-11 and 4-12. For these 3 rain images, the co-registration of rain features between HWF and HWA were definitely improved (as shown in Figure 4-12), but the spatial alignment of rain features with NX were consistently mis-registered (similar to the CAPI-1.5km results). Moreover, compared to the CAPI-1.5km scatter diagrams, these results (between NX and the HWF and HWA) were improved. In addition, in Figure 4-13 and 4-14, additional scatter diagrams at higher altitudes (CAPI's at 4.5 km and 6 km) are presented that show good agreement. Although, at these altitudes, the number of rain pixels (1 km cubes) were significantly reduced and corresponding rain rates are lower.

In summary, the most probable reasons for the spatial mis-registration observed between the rain features in NEXRAD and HIWRAP CAPI's are; radar observation time differences of the rapidly moving storm, different radar viewing geometries, and rain propagation attenuation (not yet considered). Concerning the geometry, the NEXRAD near-horizontal antenna scan had good range resolution (1 km), but the effective (2-way) antenna beam diameter was large ~ 2 km (i.e., ~ 4 cubes in a single NX measurement). On the other hand, the downward viewing conical scan of HIWRAP (IFOV 0.5 x 1 km) provided an excellent match for the cubes. However, a serious issue was the rain propagation loss (attenuation) over path lengths of a few km, which was negligible for the NEXRAD frequency (S-band) but was highly attenuated for the HIWRAP frequency (Ku-band). As will be discussed in the next section, we conclude that the HIWRAP rain rate measurements at low altitudes were significantly reduced compared to the true rain rates (represented by NEXRAD measurements).

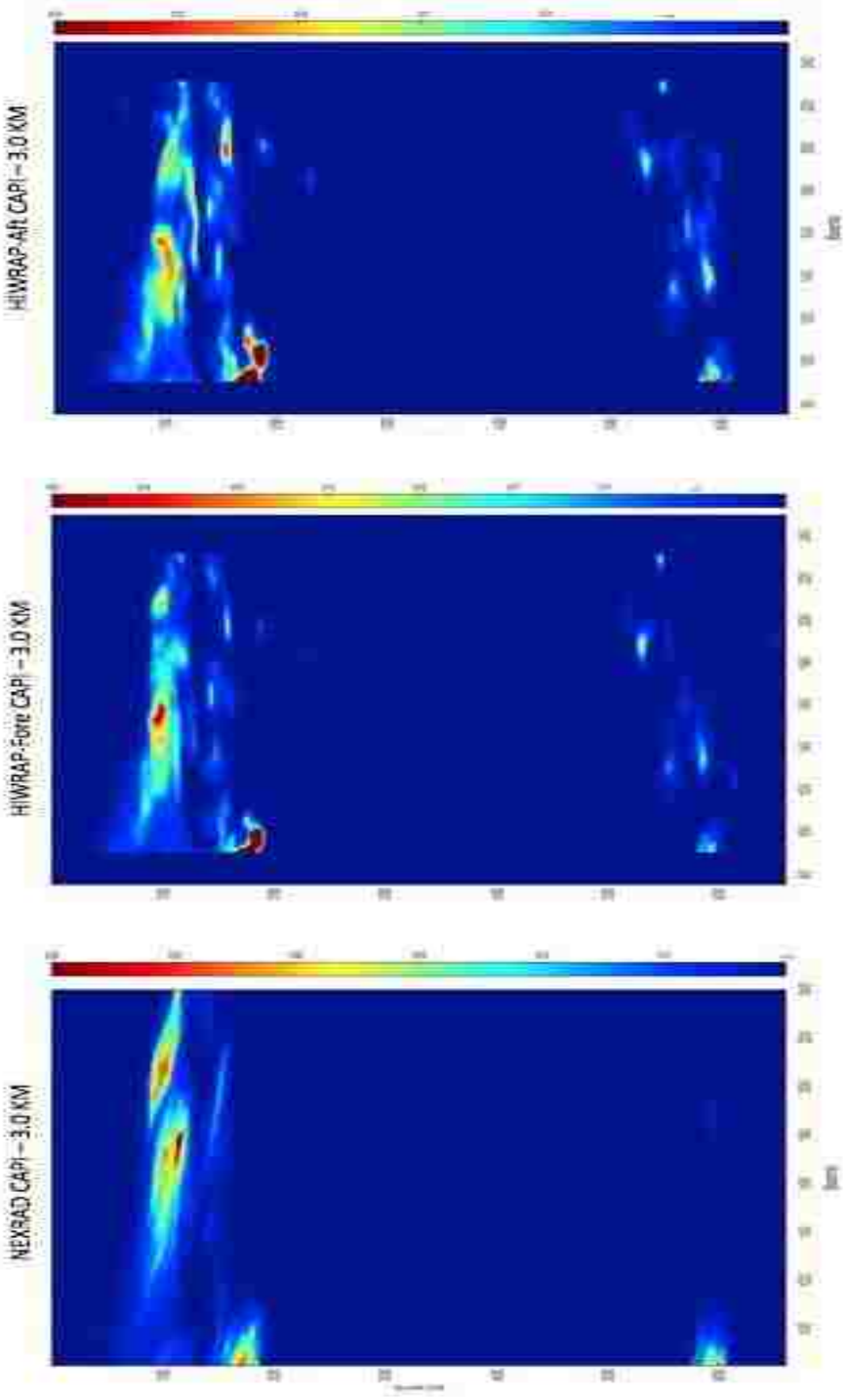

Figure 4-11: NEXRAD and HIWRAP CAPI-3.0km corresponding 2D Rain Images (MatLab imagesc), where color scale is rain rate in mm/h.

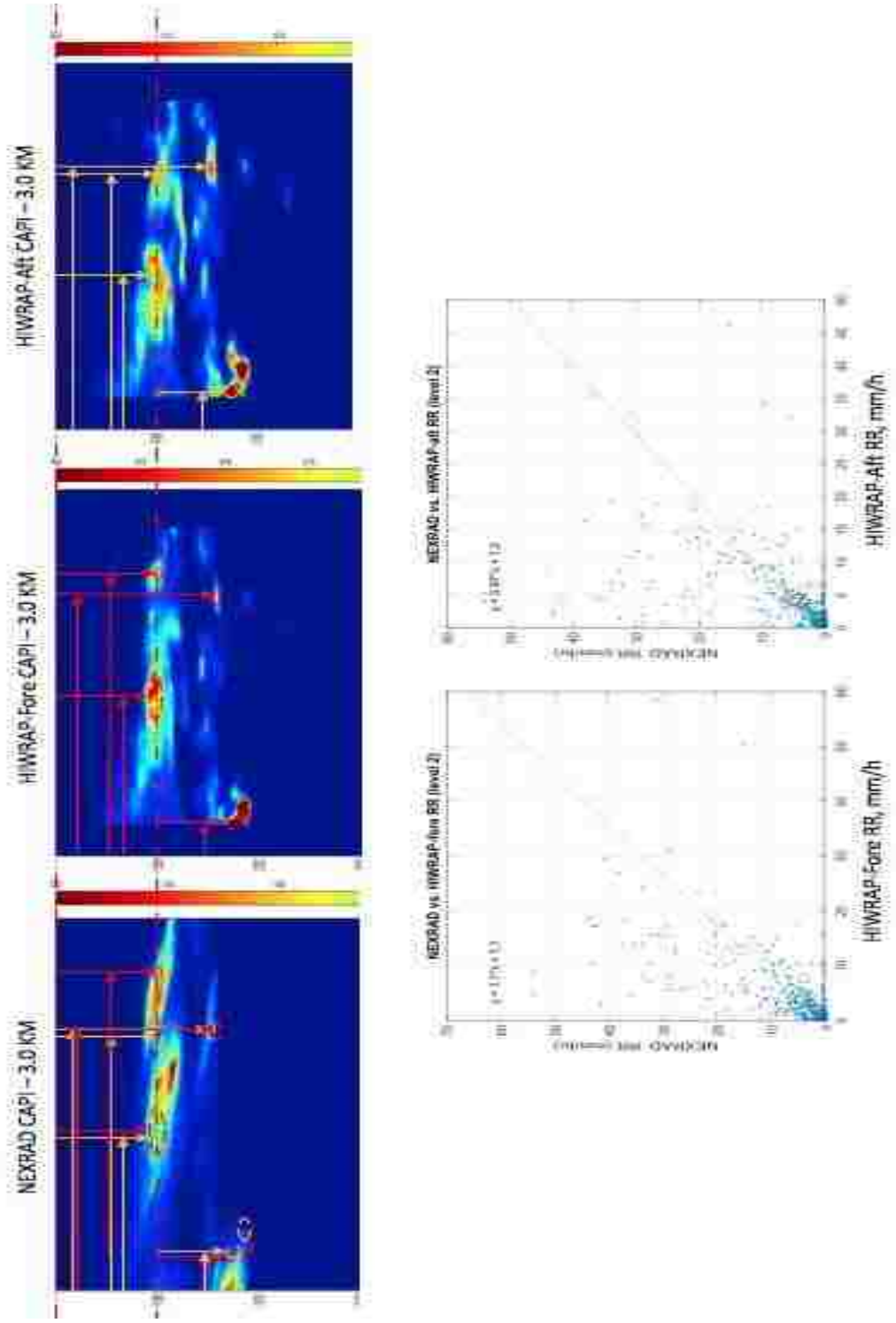

Figure 4-12: NEXRAD and HIWRAP CAPI-3.0km corresponding 2D Rain Images (MatLab imagesc), and scatter diagrams (bottom right) Fore-looking and (upper right) Aft-looking.

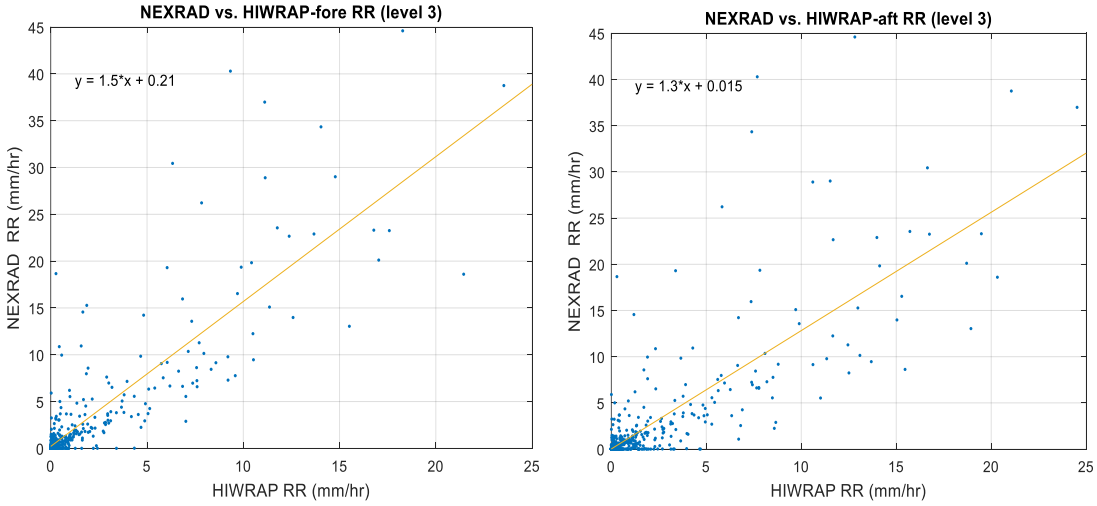

Figure 4-13: HIWRAP and NEXRAD scatter diagrams for CAPI-4.5km.

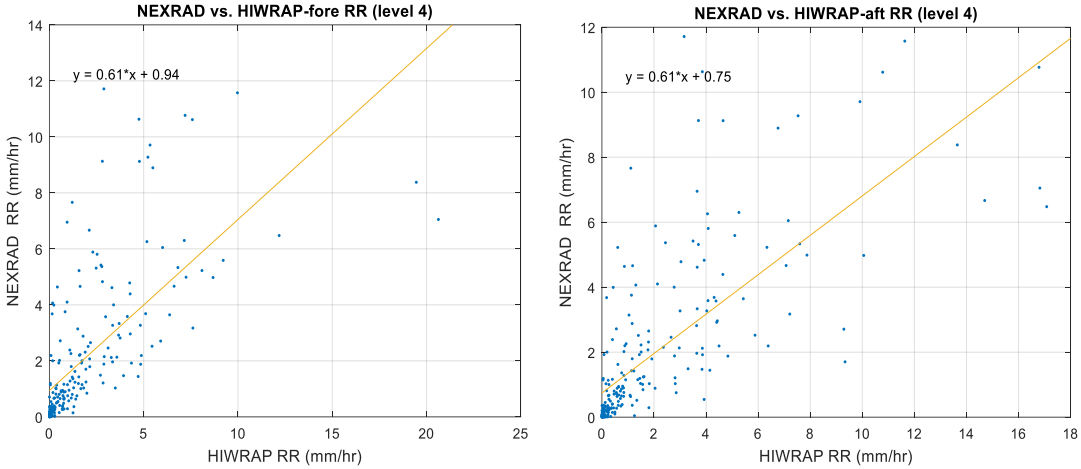

Figure 4-14: HIWRAP and NEXRAD scatter diagrams for CAPI-6.0km.

4.5 Cross-track Rain Rate Profile

Next, we present the NEXRAD and HIWRAP rain rate profiles (versus altitude) in the cross-track plane, which correspond to the HIRAD beam-altitude plane at a selected scan position. The first example, in Figure 4-15, displays the NX CAPI-4.5km with scan-100 (displayed as a

dashed red line - left panel), and in the right panel, the corresponding rain rate profile (RRP-100) is shown with the color representing the RR in mm/h. This profile was constructed from NEXRAD rain rates from the first 4 levels of the volume scan (1.5 km to 6 km) that were distributed (3D interpolation) into the HIRAD grid (imagesc format). In the RRP-100, note that the Y-coordinates are HIRAD RTM layers from the aircraft (#1) to the ocean surface (#39), and the X-coordinates are HIRAD beam positions. Note that CAPI-1.5km corresponds to the 3rd HIRAD RTM layer in the 3D grid. In all rain rate profiles, we assume that the rain rate is constant from the 3rd RTM layer to the 1st RTM layer at an altitude of 0.5 km.

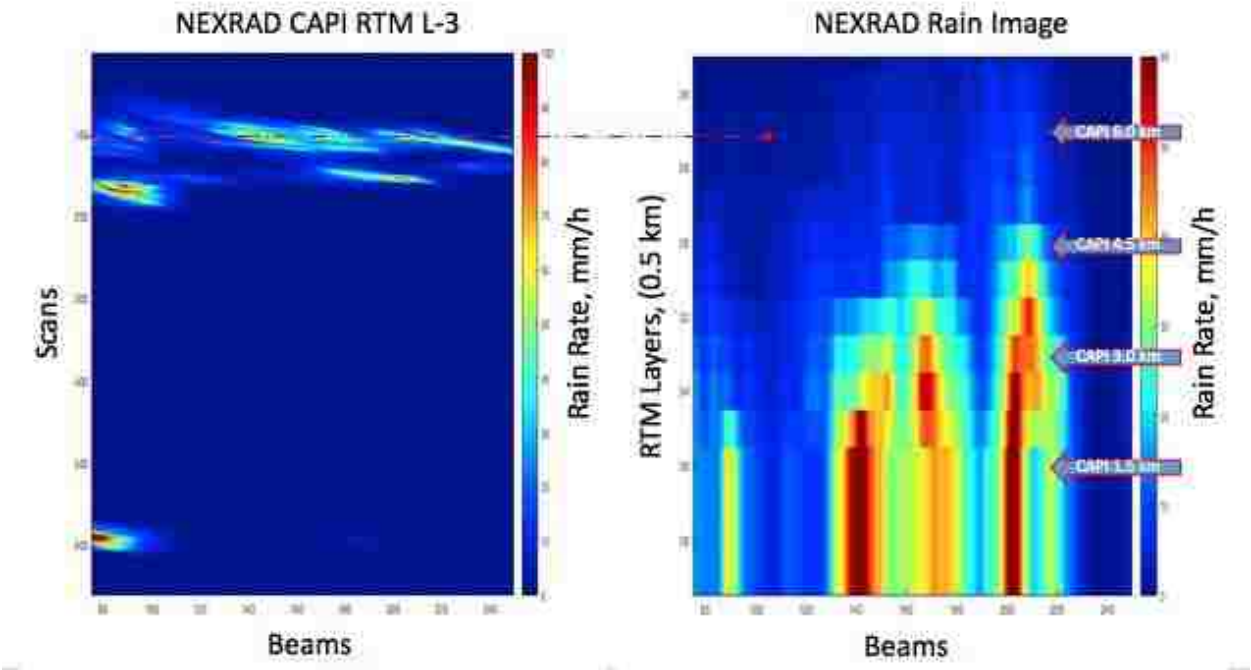

Figure 4-15: NEXRAD 2D CAPI-4.5km rain rate image (left panel) and vertical rain rate profiles (right panel) in the HIRAD cross-track plane for scan 100 (imagesc format).

Next, we show the collocated NX and HWF CAPI-4.5km in Figure 4-16 and the corresponding HIWRAP cross-track HWF (RRP-100) in Figure 4-17.

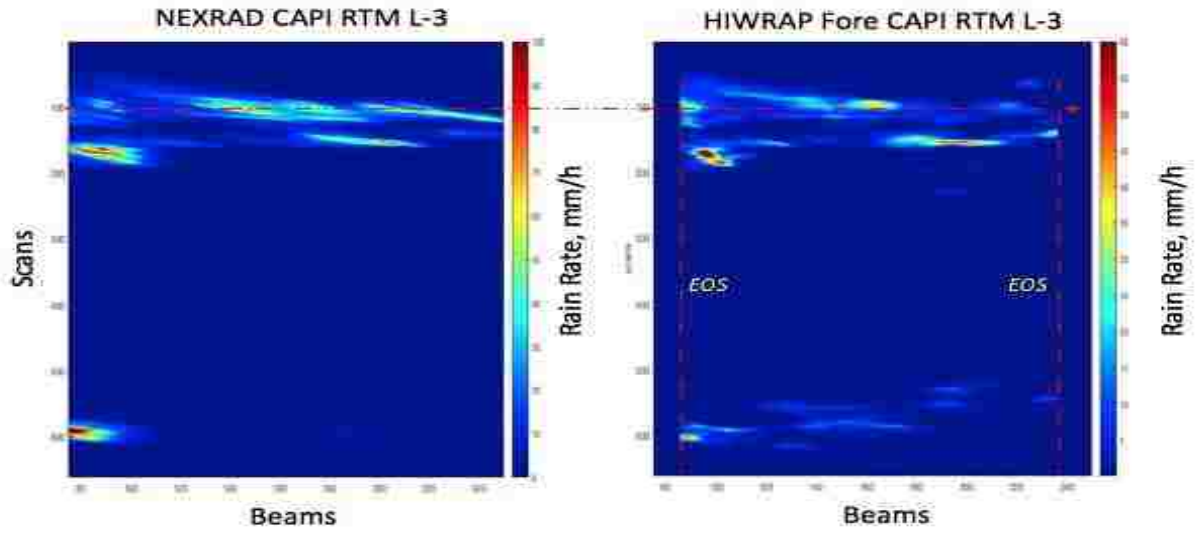

Figure 4-16: NEXRAD and HIWRAP-Fore CAPI-4.5km.

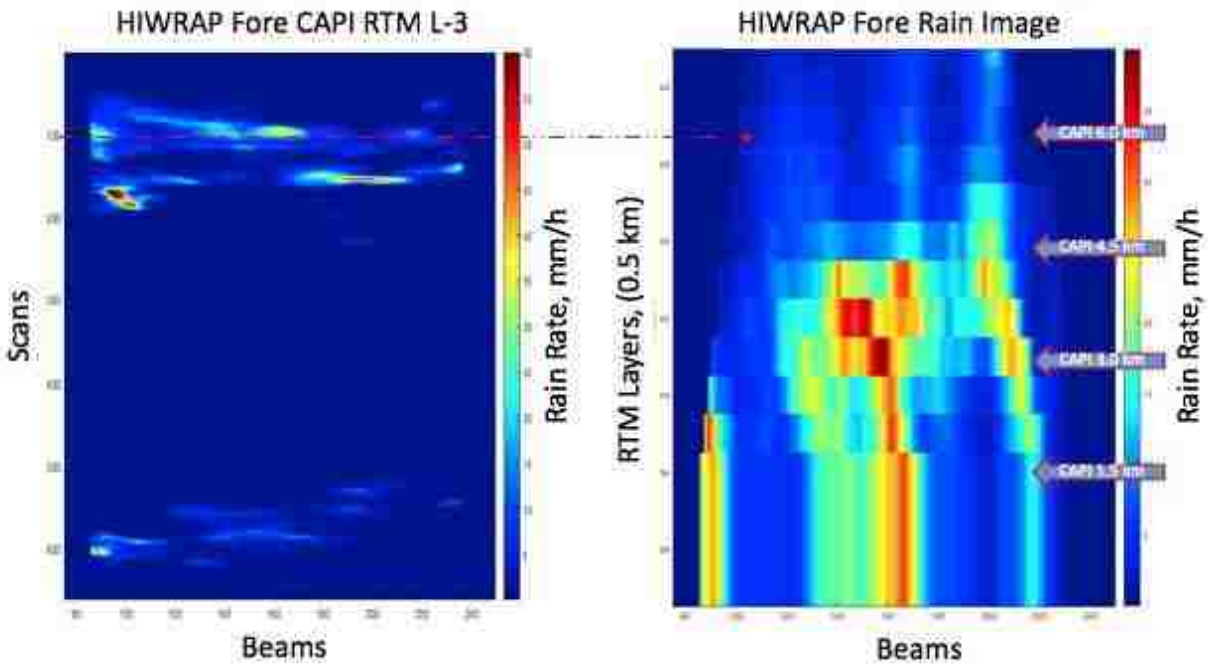

Figure 4-17: HIWRAP-Fore 2D rain rate vertical profile for HIRAD scan 100.

Since both Figures 4-15 and 4-17 are independent measurements of the same rain volume, the two RRP-100's should be identical, so we combine them into a single Figure 4.18 for comparison. The NX RRP-100 is displayed in the left panel, the HWF RRP-100 in the middle, with the color being RR in mm/h. Also, the ratio of rain rates (NX/HWF) RRP-100's is displayed in the right panel, where the color is dB scale. Note that NEXRAD observes the rain in a near-horizontal scan at S-band, and the radar echo is not attenuated.

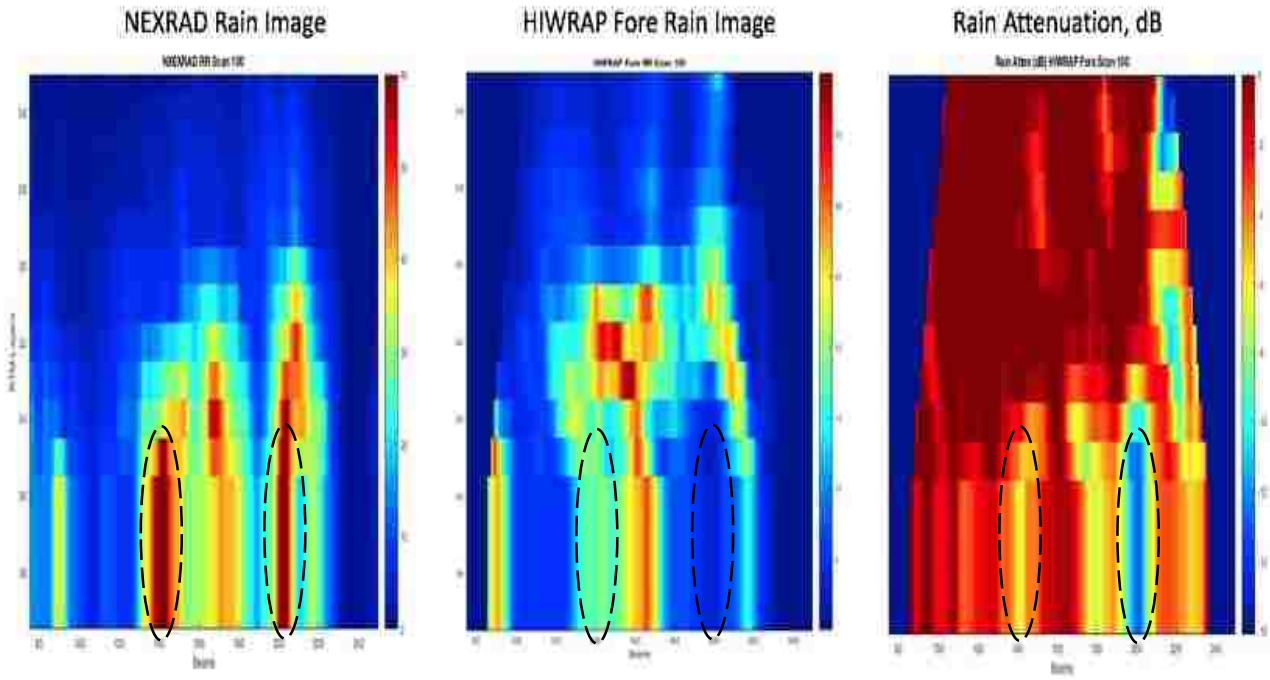

Figure 4-18: Rain rate vertical profiles for: NX (left), HWF (middle) and NX/HWF ratio expressed as dB (right). HIWRAP rain rates at the surface are significantly attenuated.

On the other hand, the HIWRAP observes the rain at Ku-band in a conical scan from the top, and the backscattered signal is attenuated proportional to the line of sight (LOS) rain rate and path length, and the corresponding regions of low HIWRAP rain attenuation are displayed as the

dark red color (0 dB) and regions of high rain attenuation are indicated by the dashed ellipses (beams 140 & 200) and by the cool colors: yellow (-8 dB) to blue (-16 dB) in the right panel.

The HIWRAP rain attenuation at an altitude of 1.5 km is illustrated in Figure 4-19. In the upper panel, the NEXRAD measured rain rate is plotted, and in the lower panel, we plotted the corresponding HIWRAP rain attenuation, which is correlated with the rain rate at that beam position. However, it should be noted that HIWRAP views the rain volume along a conical scan and not in the cross-track plane; therefore, the corresponding rain rate along the HIWRAP LOS is not necessarily the same as the NEXRAD value in this figure. Nevertheless, there is a strong correlation of HIWRAP attenuation with local NEXRAD RR.

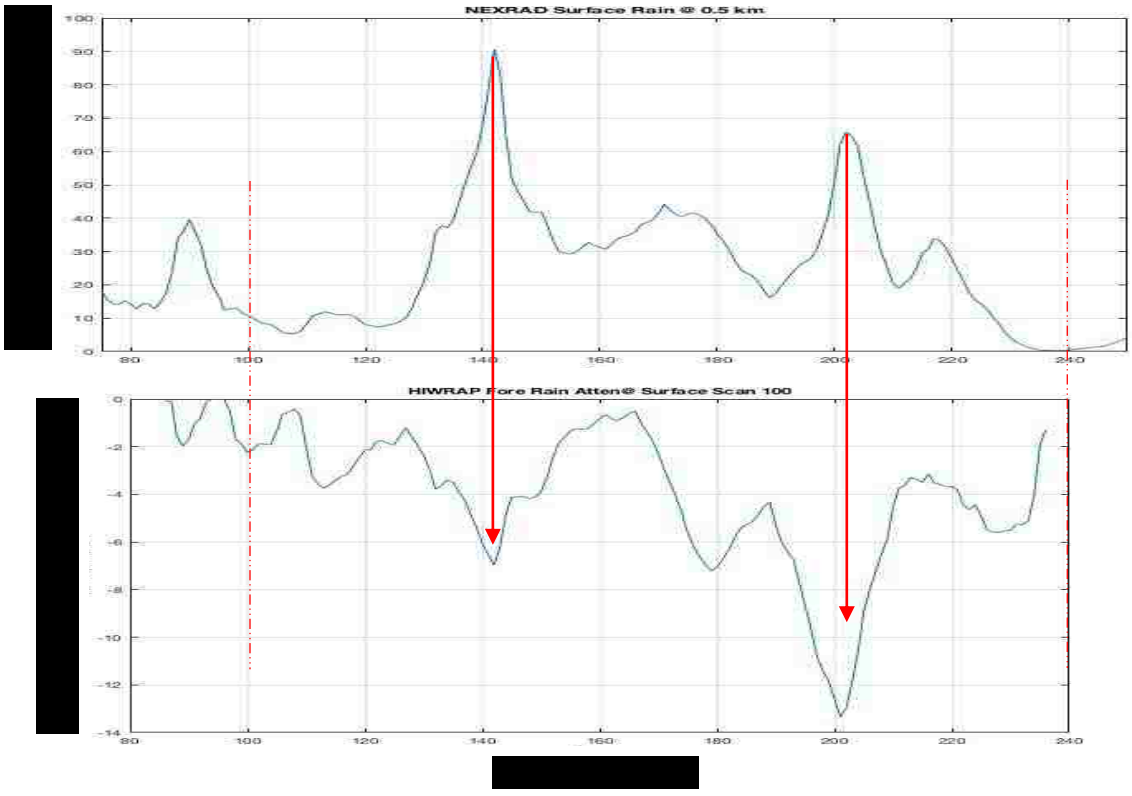

Figure 4-19: NEXRAD measured rain rate @ 1.5 km altitude (upper panel) and corresponding HIWRAP-Fore rain attenuation in dB (lower panel).

The HWF & HWA RRP-100 were corrected (by applying the inverse attenuation ratio), and as a result the 3 RRP-100's in Figure 4-20 (HWF) and 4-21 (HWA) are nearly identical.

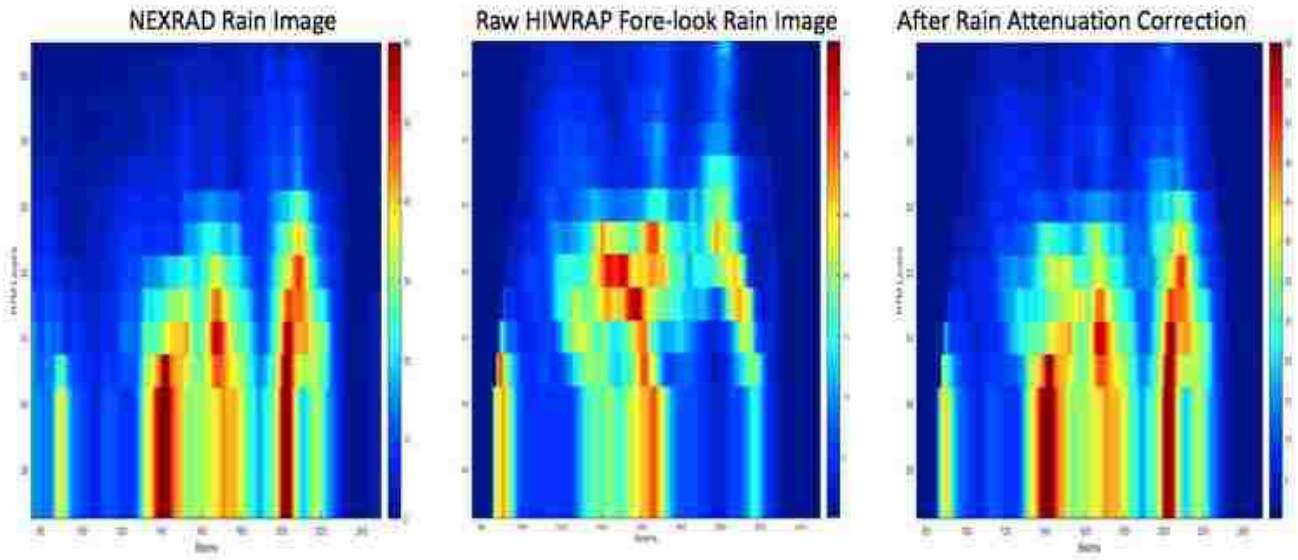

Figure 4-20: Rain rate profiles for NX (left), HWF (middle) and HWF with inverse rain attenuation correction applied.

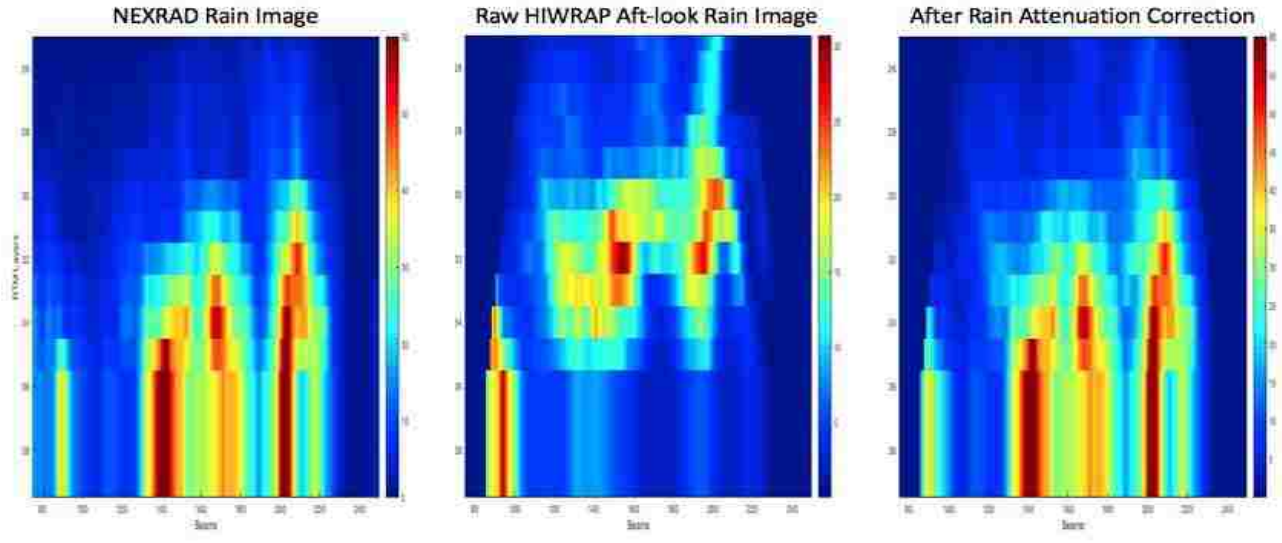

Figure 4-21: Rain rate profiles for NX (left), HWA (middle) and HWA with inverse rain attenuation correction applied.

While this gives a favorable result for this example, this ad hoc approach is not rigorous, and as a result this is not used in this dissertation. Therefore, the use of HIWRAP rain measurements as surface truth was eliminated for the comparisons that follow. Fortunately, the NEXRAD rain measurements are an excellent source of surface truth and these are used.

Further, using the NEXRAD 3D rain measurements, it should be possible to develop a rain attenuation correction for HIWRAP. However, this is estimated to be a difficult task, and as such, this effort is beyond the scope of this dissertation. Nevertheless, it is highly recommended for future research.

CHAPTER 5:
HIRAD RAIN BRIGHTNESS TEMPERATURE

The HIRAD instrument was developed to remotely sense hurricanes wind speed and rain rate; and to retrieve these quantities, it is necessary to have an accurate ocean brightness temperature theoretical model. Since HIRAD is a 1D STAR radiometer (see Section 2.2), the Tb measurement is synthesized simultaneously in the cross-track plane, which is equivalent to a push-broom antenna with 321 equally spaced sub-beams that are combined to make the scene Tb (see Figure 2-5). Thus, given the multi-frequency (4, 5, 6 & 6.6 GHz) Tb measurements, the WS and RR retrievals are obtained as simultaneous solutions on a pixel by pixel (beam #) basis in the cross-track plane.

Since the measured brightness temperature is the scalar sum of blackbody emission (random noise) from the surface as well as two Tb atmospheric components (upwelling and downwelling), it is necessary to consider the instrument line-of-sight geometry. Moreover, the HIRAD IFOV is designed to Nyquist sample the hurricane surface wind field that reduces exponentially in a radial direction from the hurricane eye (spatial scale is of order 10's of km). On the other hand, the hurricane spiral rain bands are more heterogeneous comprising a collection of convective rain cells (thunderstorms) with spatial scales of km. As a result, for a particular off-nadir surface point (HIRAD beam #), it is recognized that these upwelling and downwelling atmospheric paths pass through different nonhomogeneous rain regions.

As previously mentioned in Section 1.2, the effect of rain has dominated the observed Tbs, and as a result WS retrievals have been significantly degraded for moderate to strong rains. Therefore, to retrieve the weaker WS signal in the presence of a stronger rain rate signal, it is

necessary to precisely measure (and model) these atmospheric components of rainy Tb. As a result of this dissertation research, we will validate the improved the HIRAD measured and modeled Tbs, which will be used in the WS and RR retrieval.

5.1 HIRAD Measured Tb

5.1.1 Radiometric Calibration

Based upon HIRAD in-flight history, there were two significant issues associated with the measured Tbs. The first issue concerned the absolute radiometric calibration of the four frequency radiometer channels. Although the receivers had noise diode injection for continuous gain calibration, the phased array antenna was outside of this calibration loop. Because of high distributed losses (2 - 3 dB) in the antenna beamformer, there were large loss-self-emission radiometric biases (~ 100 - 140 K), which had to be accurately known and subtracted to calculate the ocean scene Tb. Given the scene brightness (Tap) captured by the antenna, the "antenna temperature" (Ta) input to the radiometer receiver was:

$$T_a = T_{ap}*L + (1 - L)*T_{phy} \tag{5.1}$$

where L was the total distributed loss transmissivity (power ratio) between the antenna aperture and the input to the receiver, $(1 - L)$ was the corresponding total distributed loss absorption (power ratio), and T_{phy} was the effective physical temperature of the distributed loss (Kelvin). During the HIRAD flight at high altitude, the ambient air was a heat sink that cooled the antenna. While there were on-board heaters that made-up for this heat loss, the physical temperature of this front-end loss never stabilized during flight.

So, the desired measurement was the scene temperature given by

$$T_{ap} = (T_a - (1 - L)* T_{phy})/L \quad (5.2)$$

but unfortunately, neither the loss (L) nor the T_{phy} were well known. However, it is expected that the beamformer loss was constant, but the T_{phy} changed in an unpredictable manner over time periods of minutes to hours. The best estimate of the resulting HIRAD Tb measurement error comes from Sahawneh [19], who performed an analysis of HIRAD in-flight observations for clear-sky ocean with uniform moderate wind speeds (~ 8 – 10 m/s). He found that over a typical one-hour period of HIRAD operation, the 5 GHz Tb calibration changed slowly in an unpredictable manner with a 10 K peak to peak excursion.

To mitigate this unacceptable radiometric performance, Ruf et al. [20] developed an effective in-flight calibration procedure, using clear-sky ocean scenes, to provide the radiometric (Tb) calibration. Since the Tampa Bay Rain Experiment included both clear-sky ocean and an over-flight of North Florida peninsula, we extended this approach to using known cold (ocean) and hot (land) radiometric Tb scenes to produce "adjusted" HIRAD Tbs that were used for the data analysis that follows.

5.1.2 Tb Image Stripes

The second HIRAD radiometric calibration issue involved non-geophysical artifacts in Tb images (known as "stripes" [21]) that frequently existed and had to be removed before data analysis could be performed. For the Tampa Bay Rain Experiment, Tb stripping occurred in both ocean and land Tb images for 5, 6 & 6.6 GHz channels, and an example for the least-affected channel at 5 GHz is illustrated in Figure 5-1. For this image the EIA is truncated to ± 60°, which corresponds to beams (21:301). Because the land brightness temperature scene is approximately independent of EIA (constant Tb), the stripes were more recognizable in this scene (right panel).

On the other hand, for oceans (left panel), the stripes were also present, but they were partially masked by a large change in the scene brightness with EIA that caused the brightness to decrease from the swath center to both edges. Also, for the ocean scene, high Tb bands existed at both ends of the image because of the increased Tb associated with the rain events.

These stripes resulted during the inverse Fourier transform of visibilities (complex cross correlation between pairs of antenna elements) used to form the scene brightness image. In simplest terms, these stripes can be thought of as radiometer gain variations (a multiplicative factor) in cross-track beam # positions, which resulted in Tb variations approximately aligned with the flight direction (i.e., at fixed beam #).

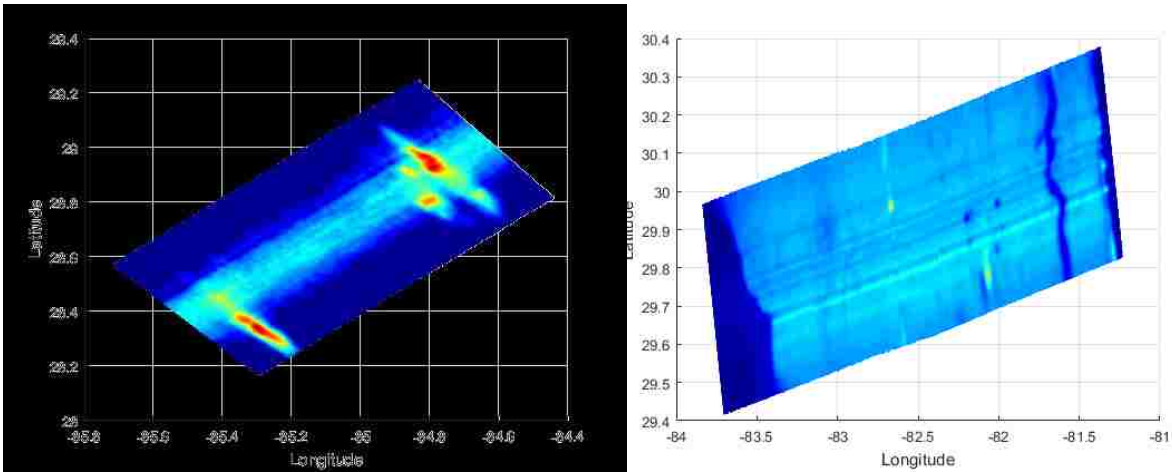

Figure 5-1: HIRAD Tb 5 GHz Tb images for ocean (left) and land (right) with "Tb stripes" occurring in the along-track direction. Note that the mean value has been subtracted from each image, and the color represents Tb from radiometrically cold (blue) to hot (red).

For this dissertation, the removal of these stripes artifacts was performed (separately by beam #) using the total power radiometer transfer function (TPRTF) developed from average Tbs during the HIRAD passes over ocean (radiometrically cold) and land (radiometrically hot). We averaged the clear-sky ocean Tbs over HIRAD scans 250 to 500 to produce the cold calibration

point. For land, the scene brightness was constant over EIA, although we filtered these data to remove Tb < 200 K (that removed cold Tbs associated with lakes, rivers and oceans). Also, we filtered unrealistic land Tb regions > 300K that were caused by radio frequency interference (RFI). After filtering, we calculated the mean Tb by beam position, and we used the land brightness value of 281 K based upon previously measured SFMR Tbs over land [19].

Next, we performed the TPRTF, using linear regression of the average ocean and average land points, calculated separately for each beam position to preserve the incidence angle effect on the measured Tb. An example TPRTF is shown in Figure 5-2 for beam # 80, where the modeled clear-sky ocean was 116 K and the land was 281 K, and the resulting TPRTF given as

$$(T_{b_{recalib}})_{i,j} = (T_{b_{raw}})_{i,j} * gain_{\,j} + offset_j, \tag{5.3}$$

where slopes and offsets for all beam # are presented in Figure 5-3.

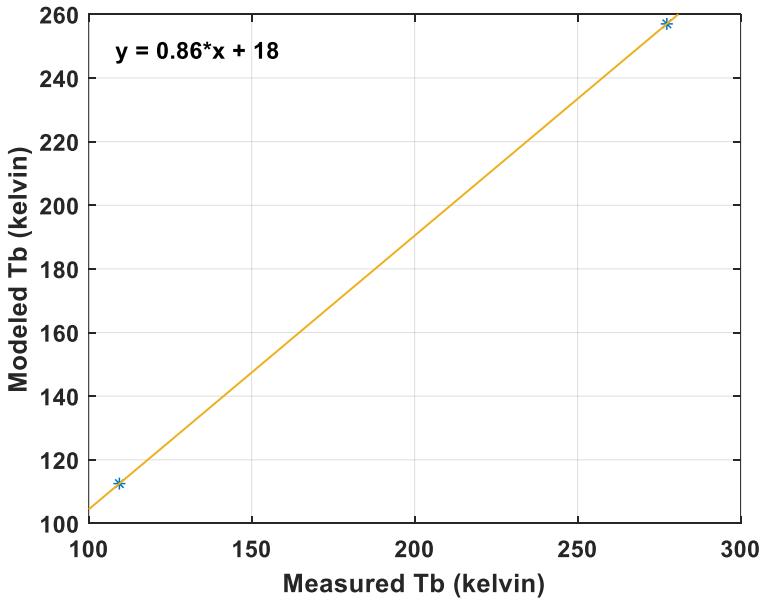

Figure 5-2: Total power radiometer transfer function for HIRAD 5 GHz channel for beam # 80. Calibration uses linear regression of clear-sky ocean scenes (cold point) and land (hot point).

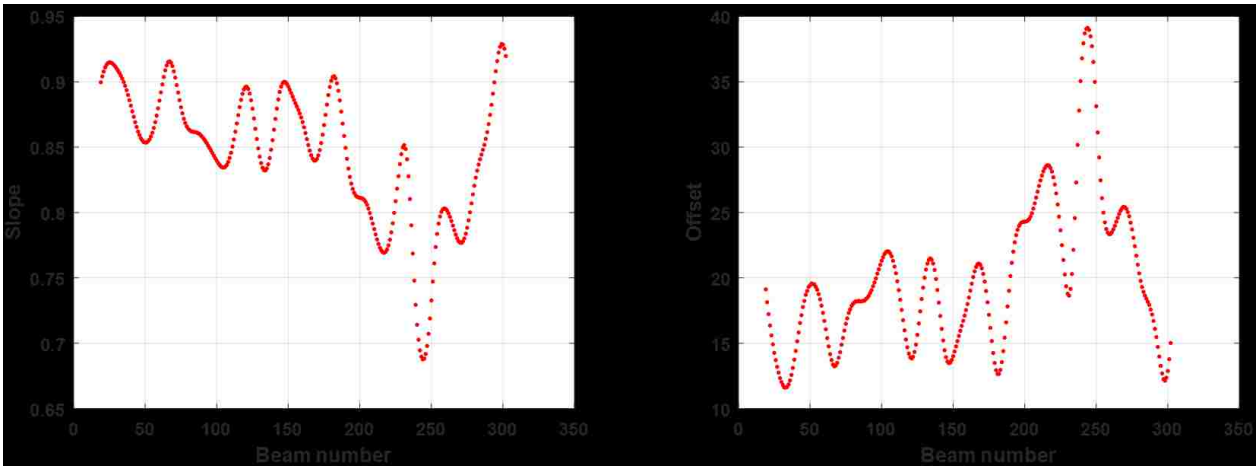

Figure 5-3: Total power radiometer calibration linear regression: Slope (left panel) and Offset (right panel) for HIRAD 5 GHz channel and all Beam #'s.

Consider first the 5 GHz channel Tb images shown in Figure 5-4 (matrix format) with color-bars indicating the Tb scale in Kelvin. The raw Tb measurements are shown in panel-(a), and the corresponding recalibrated Tb measurements are shown in panel-(b). The clear-sky portion of the image is located between scans 200 and 550, where the Tbs are the result of ocean surface emission that are dominated by the EIA effect (highest Tb in the center and monotonically decreasing to the swath edges). The next panel-(c) shows an image of the difference of raw and recalibrated Tb images (color-bar for this panel is +6 to -10 K) and note the existence of systematic Tb variations (aligned with the flight direction) that are known as "stripes". These artifacts, of the image formation process, introduce non-geophysical noise into the Tb image, which can be removed (destriped) in post-processing of the Tb image [21]. In general, the number and location of Tb stripes are random, and the destriping process is somewhat subjective. Fortunately, with the unique HIRAD two-point (hot & cold) radiometric calibration employed during this experiment, it was discovered that these stripes have been effectively removed from the recalibrated Tb image.

In panel-(d), the average clear-sky, ocean Tb profiles are plotted for the raw and recalibrated datasets. The similarity of these plots indicates that only minor differences in calibration exist for 5 GHz; however, note that the Tb stripes observed in the difference Tb image (panel-(c)) are very sensitive to small gain and offset differences.

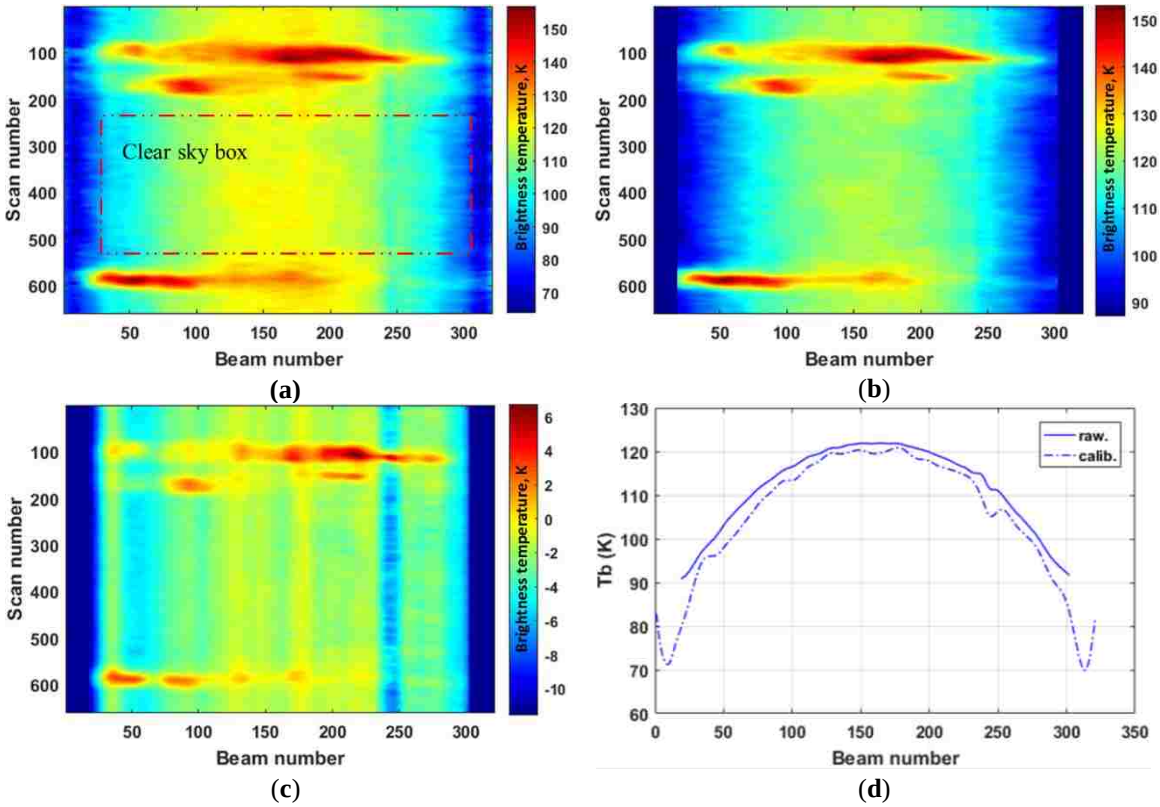

Figure 5-4: HIRAD Tb measurements for 5 GHz in (a) raw Tbs; (b) recalibrated Tbs; (c) difference between Raw and Adjusted Tbs; and (d) average ocean Tb in "clear-sky box" for raw (dashed) & calib (solid).

Next, the corresponding Tb images for 6 GHz are presented in Figure 5-5. The matrix plots of raw and recalibrated Tbs are similar to the corresponding 5 GHz plots, but the difference matrix shown in panel-(c) is not correlated with the respective 5 GHz image, and the corresponding color-bar has a wider dynamic range (-10 to +25 K). Moreover, the two plots in panel-(d), for the clear-

sky ocean scene, results in larger separations (and greater variability) between curves than for the 5 GHz comparisons.

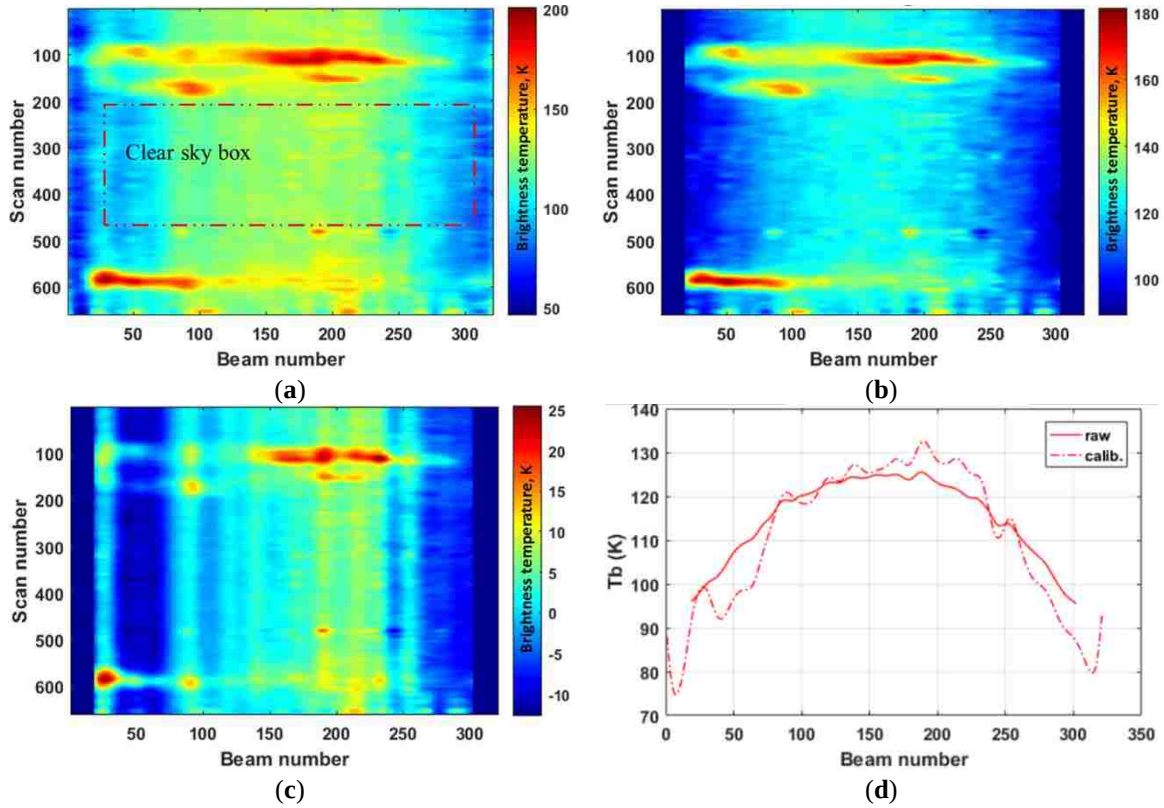

Figure 5-5: HIRAD Tb measurements for 6 GHz in (a) raw Tbs; (b) recalibrated Tbs; (c) difference between Raw and Adjusted Tbs; and (d) average ocean Tb in "clear-sky box" for raw (dashed) & calib (solid).

Finally, the corresponding 6.6 GHz measurements are presented in Figure 5-6. For this case, consider first panel-(d), which shows the effect of poor cross-polarization ratio in the HIRAD antenna at the edges of swath. As a result, the swath width is reduced to beam #'s of 50 to 270, and the corresponding beam #'s (X-axis) for panels-(a), (b) & (c) are also truncated to match. Looking at the clear-sky Tb image, there are stripes that are removed by the linear recalibration; however, the rain images are badly distorted compared to 5 and 6 GHz. Therefore, our analysis set

was reduced to only 5 and 6 GHz. Fortunately, this is a negligible impact to our objective of validating the forward RTM.

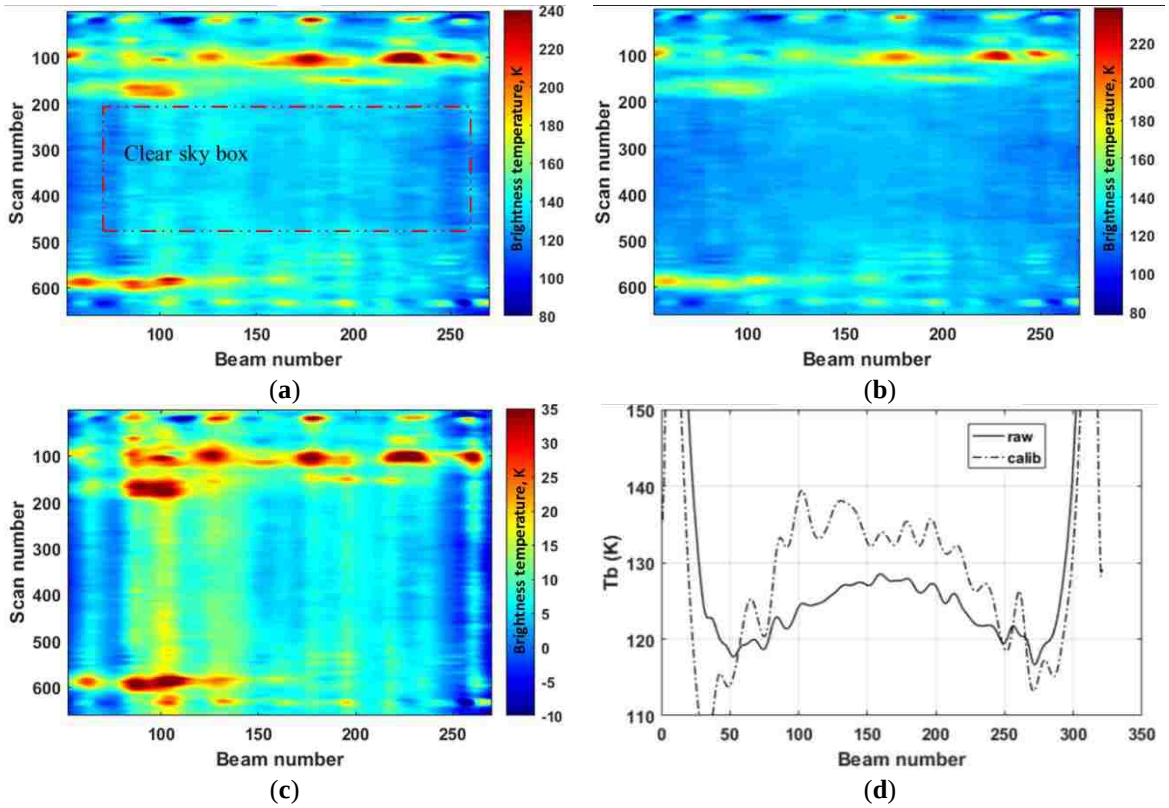

Figure 5-6: HIRAD Tb measurements for 6.6 GHz in (a) raw Tbs; (b) recalibrated Tbs; (c) difference between Raw and Adjusted Tbs; and (d) average ocean Tb in "clear-sky box" for raw (dashed) & calib (solid).

Also, shown in Figure 5-7 are the corresponding land Tb image results, which were equally successful in removing stripes. All HIRAD Tb data used in this dissertation were "adjusted" using the TPRTF, and the data matrices are so designated e.g., "Tb5_24_adj" corresponds to: 5 GHz Tb for ocean flight pass-24 and "adjusted" using the TPRTF.

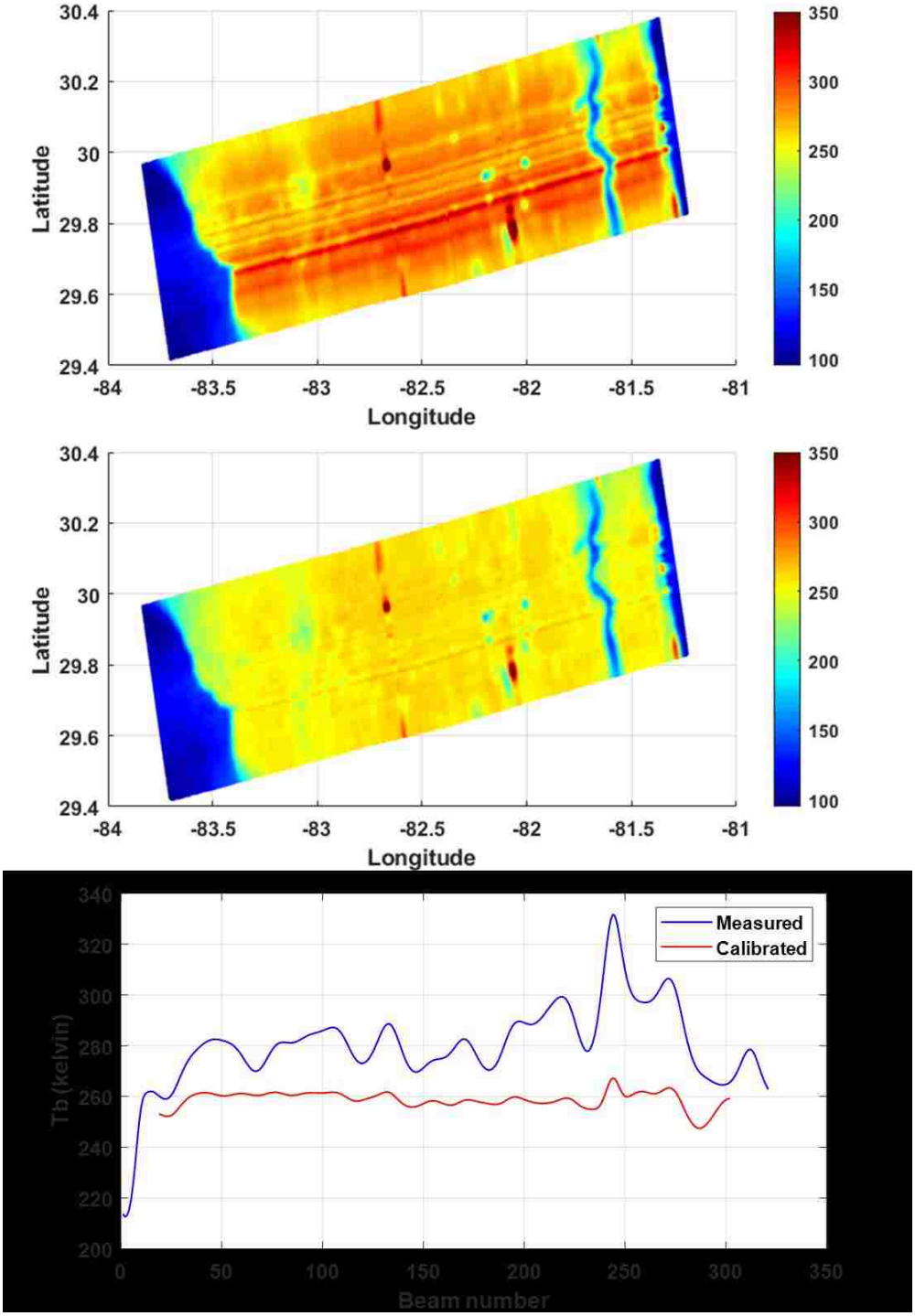

Figure 5-7: HIRAD raw (uncorrected) land Tb image at 5 GHz (upper) and adjusted Tb image (middle) after applying the TPRTF to calibrate the Tbs. The average Tbs by beam #'s are presented in the lower panel and note that the stripes were removed during this process.

5.2 HIRAD Modeled Tb

5.2.1 Forward RTM

The original HIRAD Radiative Transfer Model was developed by Amarin [5, 6], to calculate the brightness temperature at the HIRAD antenna aperture based on the observation geometry and environmental parameters from the 3D atmosphere and ocean surface, as shown in Figure 5-8. The scene brightness temperature is the scalar sum of three Tb components at the antenna aperture, namely: the upwelling atmospheric graybody emission along the radiometer line of sight (LOS), the ocean surface emission, and the downwelling atmospheric emission that is specular reflected at the ocean surface. Note that the latter (downwelling) component includes two sub-components, namely: the transmitted cosmic background brightness (2.73 K) and the self-emission due to atmospheric absorption.

At HIRAD's C-band frequencies (4 – 6.6 GHz), the absorption of microwaves by water vapor and cloud liquid water are negligible; therefore, the atmosphere is very transparent except for rain, which is a strong absorber/emitter of Tb. For clear-sky conditions, the relevant oceanic environmental parameters that affect Tb are surface wind speed (m/s) and sea surface temperature (Kelvin).

Before HIRAD, the majority of microwave imagers, were conical scanners with an earth incidence angle (EIA*)* of 50° - 60°. Because of this, theoretical ocean surface emissivity models were not available for the HIRAD EIA's between nadir and 50°. Further, the ocean emissivity models only performed well for WS ≤ 20 m/s, which is the lower-end of the HIRAD measurement requirement. Fortunately, the SFMR had developed an empirical ocean emissivity model at nadir that extended WS to ~ 70 m/s. So, the critical issue became the development of a new ocean

emissivity model that covered the full EIA and WS range for HIRAD. The CFRSL accepted this challenging assignment that became the dissertation of El-Nimiri [22, 23]. Without this model, the prelaunch HIRAD hurricane simulation and feasibility study of Amarin would not have been possible, and most likely, the instrument would not have been developed.

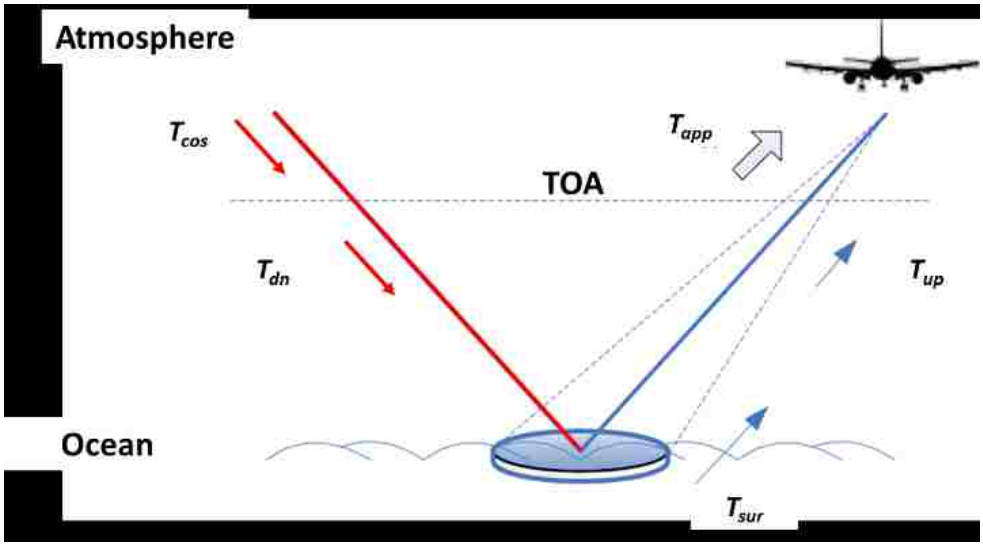

Figure 5-8: RTM upwelling and downwelling geometry in the HIRAD cross-track plane from Amarin [6].

Thus, the modeled apparent brightness temperature (T_{model}) as function of the *EIA* (θ) at the top of atmosphere is:

$$T_{model} = T_{up} + e_{up}^{-\tau} * \left(\varepsilon * SST + \Gamma * (e_{down}^{-\tau} * T_{cos} + T_{dn})\right) \tag{5.4}$$

where

$$T_{up}(\theta) = \sec(\theta) * \int_0^{TOA} K(z')T(z')e^{-\tau(z',TOA)sec\theta}\, dz' \tag{5.5}$$

$e_{up}^{-\tau}$ (& $e_{down}^{-\tau}$) is total atmospheric transmissivity of the upwelling (& downwelling) path, ε is the ocean emissivity from El-Nimiri [22, 23], $\Gamma = (1 - \varepsilon)$ is the ocean power reflection coefficient, T_{cos} is the Cosmic brightness temperature (2.73 K), and

$$T_{dn}(\theta) = \sec(\theta) * \int_{TOA}^{0} K(z')T(z')e^{-\tau(0,z')sec\theta}\, dz' \tag{5.6}$$

To implement the T_{up} & T_{dn} calculation in a computationally efficient manner, we divide the propagation path into thin (0.5 km) planar layers, and thereby, expressed the integral as a summation of blackbody emissions (T_i) at the center of "*n*" (39) RTM layers through slightly absorptive atmosphere. Thus, of the upwelling brightness temperature is:

$$T_{up} = \sum_{i=1}^{n} (T_i \cdot \sqrt{\tau_{up_i}} \cdot \prod_{j=i+1}^{n} \tau_{up_i}) \tag{5.7}$$

where $T_i = sec\theta\ K_i\ \Delta z' T_{phy\_i}$, K_i is the atmospheric absorption coefficients (sum of clear-sky and rain) of the RTM i^{th} layer, $\Delta z'$ is the layer thickness (0.5 km all layers), T_{phy_i} is the atmospheric physical temperature of the i^{th} layer and $\tau_{up_i} = e^{-K_{up} \cdot h_i \cdot \sec\theta}$ is the transmissivity of the i^{th} RTM layer.

Similarly, the downwelling is:

$$T_{dn} = \sum_{i=n}^{1} (T_i \cdot \sqrt{\tau_{dn_i}} \cdot \prod_{j=i}^{i-1} \tau_{dn_i}) \tag{5.8}$$

For clear-sky, an example of the modeled TOA ocean brightness temperature in the cross-track scan is presented in Figure 5-9. Because the TOA Tb is primarily ocean surface emission, the resulting brightness temperature is an even function of EIA, where the center of the HIRAD swath is the nadir viewing beam (160) and the swath edges are EIA's of ±60° (beams 21:301). The curves are plotted for 5 GHz (solid lines) and 6 GHz (dashed lines), for 3 wind speed cases of 10,

20 & 30 m/s (blue, red and black colors respectively), and note that the Tb increases approximately exponentially with WS for all beams (EIA's) and for both frequencies.

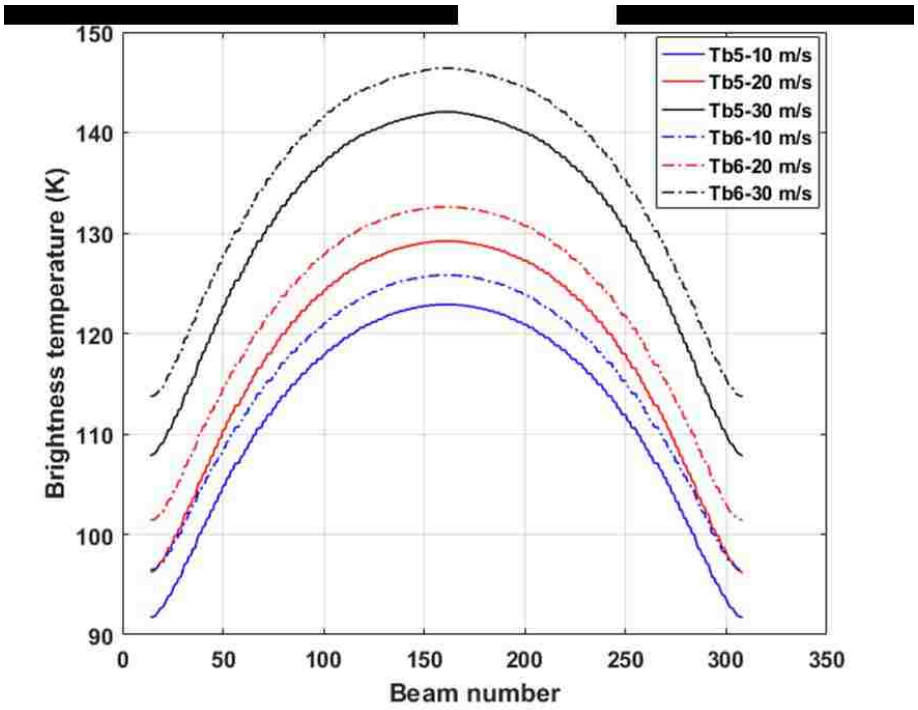

Figure 5-9: Theoretical clear-sky, TOA, Ocean Tb for HIRAD at 5 GHz (solid curves) and 6 GHz (dashed curves) for fixed WS of 10 (blue), 20 (red) & 30 (black) m/s.

For the case of rain, the total atmospheric absorption is the sum of clear-sky absorption and an empirical C-band rain absorption coefficient derived for the SFMR [24]. Thus, the HIRAD rain absorption is proportional to the 3D rain rate (interpolated into the individual RTM layers separately for the upwell and downwelling paths) that is expressed as:

$$K_{up} = a \cdot R_{up}^{0.87}$$

$$a = g \cdot f^{n} \tag{5.9}$$

$$n = 2.63 \cdot R_{up}^{0.06}$$

where "*a*" is the frequency "*f*" (GHz) dependent coefficient, *R* is rain rate (mm/h) and *g* is a constant of 3.94×10^{-6}. An example of the TOA modeled Tb for uniform rain (from the atmospheric freezing level to the ocean surface) is presented in Figure 5.10 for 5 & 6 GHz. There are 3-sets of solid (5 GHz) and dashed (6 GHz) curves that represent incidence angles 0°, 30° and 60°, and note that increasing rain rate results in a monotonic warming of the clear-sky, ocean Tb at all EIAs.

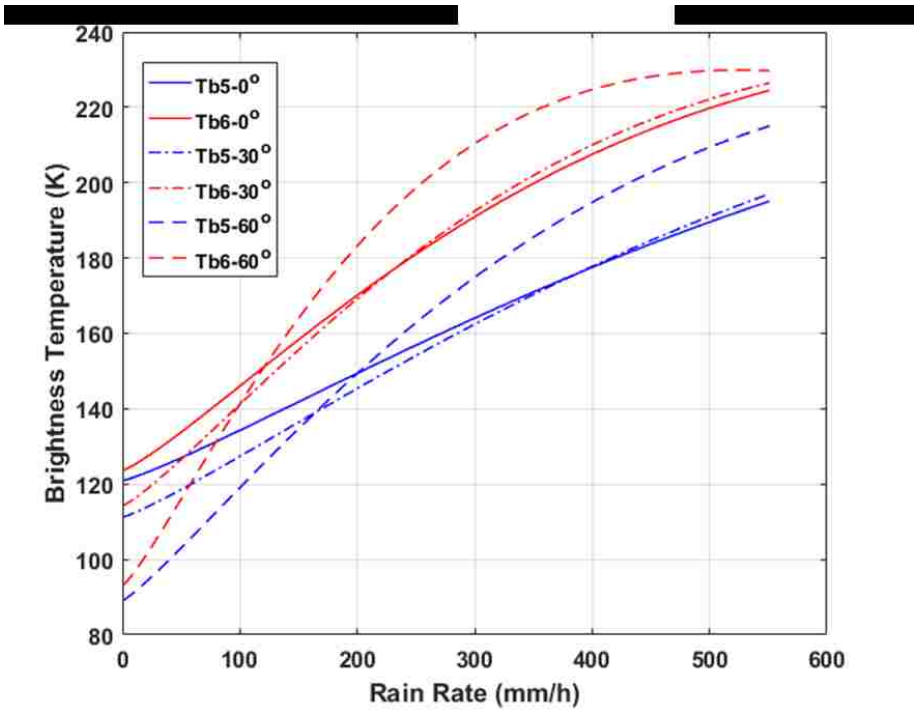

Figure 5-10: Theoretical HIRAD TOA, Ocean Tb for uniform rain rates @ 5 & 6 GHz and three *EIA*s.

5.2.2 Tampa Bay HIRAD Tb Modeling

The HIRAD RTM required input of the ocean surface and 3D atmospheric environmental parameters that occurred during the Tampa Bay Rain Experiment. For the ocean surface, the corresponding NOAA numerical weather model (GDAS) [25], showed that both the wind speed

and sea surface temperature were nearly homogeneous over the HIRAD swath, and input values of: WS = 6 m/s and SST = 302.5 K where used. As previously mentioned, at the HIRAD C-band frequencies, the atmosphere is almost transparent (transmissivity > 97% @ 5 GHz and > 95% @ 6.6. GHz). Moreover, the small atmospheric absorption is due primarily to Oxygen, so the effect of water vapor and cloud liquid are negligible; however, for completeness, typical tropical atmospheric profiles (versus altitude) of physical temperature, pressure and water vapor were used in the TOA Tb calculations.

On the other hand, the effects of rain rate are very important, and fortunately, there were two independent sources of rain measurements (NEXRAD and HIWRAP) that provided high spatial resolution 3D rain volumes that were resampled into the HIRAD grid. For the modeled Tbs, NEXRAD was chosen because it is the standard for rain measurements that is accepted by the meteorology science community. Also, another advantage of NEXRAD was that the spatial extent of these measurements were much greater than those of HIWRAP, which allowed the HIRAD RTM downwelling path to be modeled beyond the edges of the HIRAD swath. Finally, the significant uncorrected rain attenuation suffered by the HIWRAP reflectivity measurements (Chap-4), made them an unacceptable choice for independent rain measurements.

The TOA Tb calculation was performed on a given HIRAD cross-track scan by importing the corresponding NEXRAD rain rate environmental parameter into the RTM, which involved two-steps (see Figure 5-11): (1) for a given beam # (corresponding to an EIA), to define the 3D line of sight (LOS) geometry for HIRAD's downwelling and upwelling paths and (2) to determine the intersection of these LOS's with the NEXRAD rain rates resampled to the HIRAD grid. As mentioned previously, the RTM was divided into 39 atmospheric layers, equally spaced by 0.5

km; however, since the height of rain was typically ~ 5 - 6 km, the NEXRAD rain was resampled (interpolated) to fill only the lower 12 RTM layers. Nevertheless, for completeness, the entire 39 layers were used in the brightness temperature calculation.

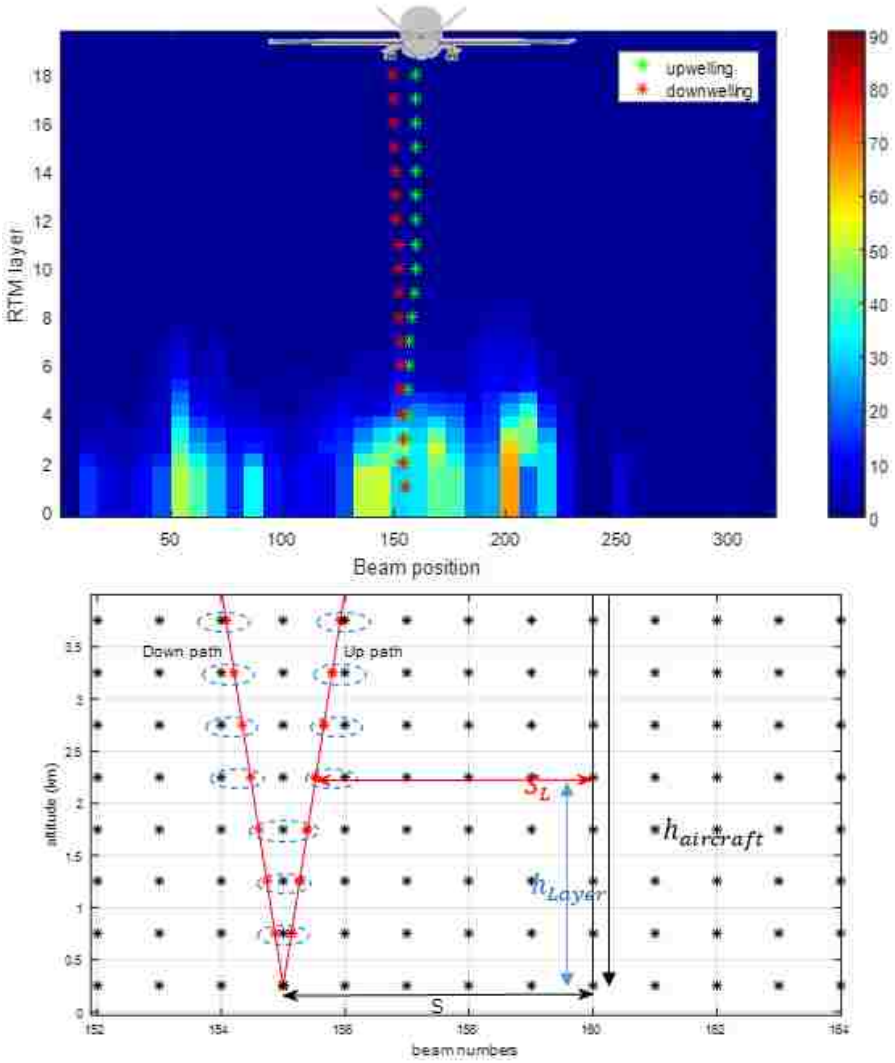

Figure 5-11: Example of HIRAD upwelling and downwelling LOS paths through the rain rate vertical profile in a selected HIRAD scan (upper panel). The lower panel shows the up- and downwelling paths (red symbols and connecting lines) for a surface beam position of 155. The black symbols are the corresponding HIRAD grid (NEXRAD RR) and dashed ellipses denote corresponding rain rate pairings.

In the process of populating rain rates into the RTM layers, we verified that a flat earth approximation (plane geometry as opposed to spherical trigonometry) was sufficient, and this assumption reduced the complexity of locating the intersection between the two HIRAD LOS paths and the gridded NEXRAD rain rates. This "pairing process" is illustrated in Figure 5-11 lower panel, where the locations of the 2D NEXRAD rain rates samples (black dots), the intersection of the LOS and RTM layer center (red dots), and the selected paired (dashed ellipses) of NEXRAD rain rates are shown. Knowing the EIA (for a given Beam #) and the altitudes of the aircraft ($h_{Aircraft}$) and RTM layers (h_{layer}), we used the method of similar triangles for pairing, as follows:

$$\frac{S}{h_{Aircraft}} = \frac{S_L}{(h_{Aircraft} - h_{Layer})} \tag{5.10}$$

where $S = h_{Aircraft} * \tan(eia)$ is the distance between the nadir point and the selected beam # (corresponding EIA) and S_L is the distance between the nadir point and the desired RTM layer.

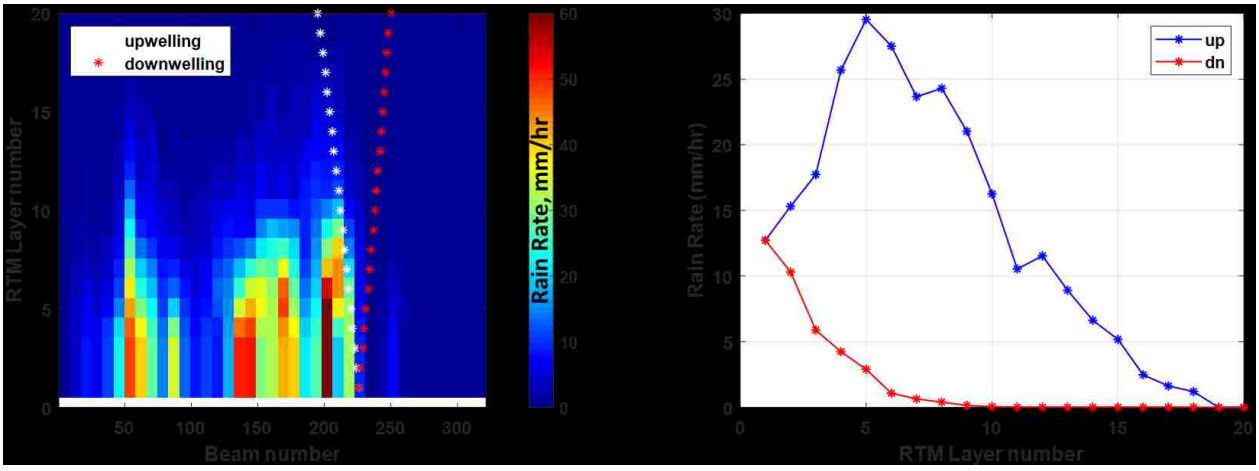

Figure 5-12: NEXRAD upwelling and downwelling paths (left panel), and the selected rain rates in the HIRAD RTM layers (right panel) for scan 110 and beam 225.

After locating the intersections between the propagation paths and the HIRAD RTM layers, the rain values for upwelling and downwelling paths were selected to be the closest rain pixel at each layer (shown within the dashed ellipses). An example of this computational process is shown in Figure 5-12 for scan 110 and beam 225. The left hand panel shows the up and down LOS's intersecting the NEXRAD 2D rain rate image, and the right hand panel shows the resulting RTM rain rate profile that produced two matrices (upwelling and downwelling) of the same size as the HIRAD grid, which was input to the RTM to compute the modeled Tb.

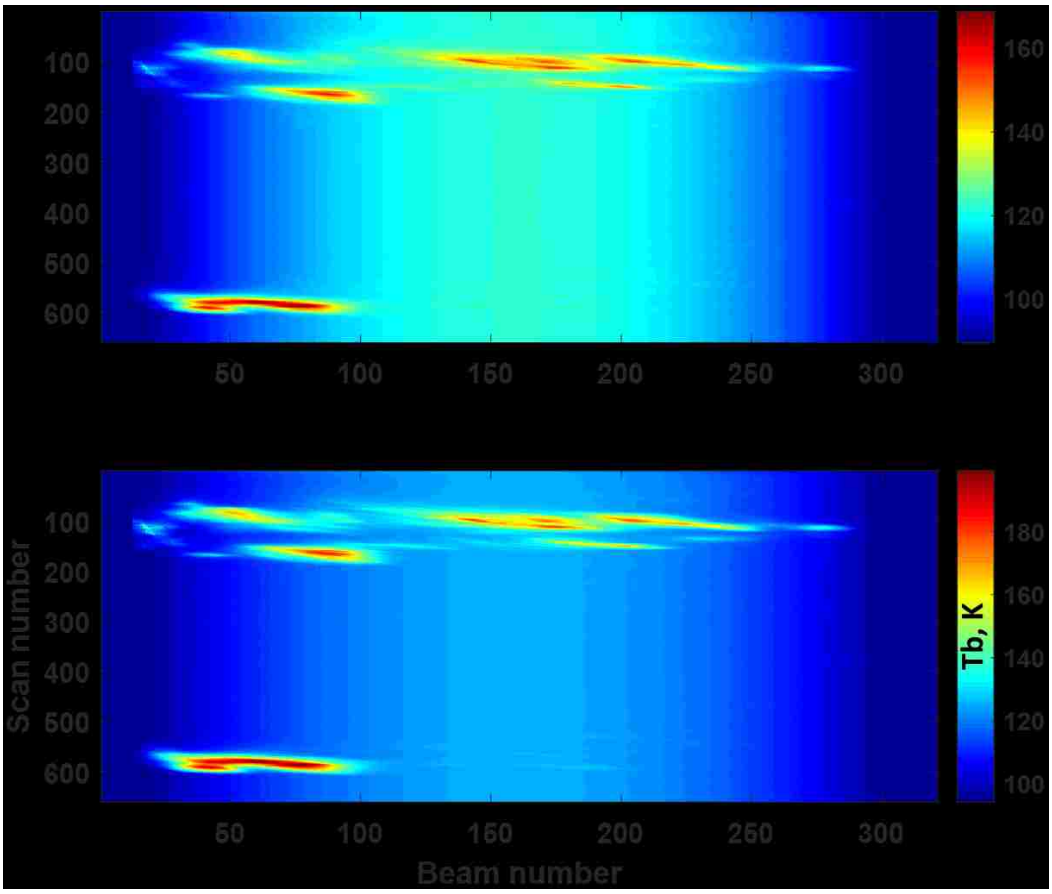

Figure 5-13: Theoretical TOA Tb for 5 GHz (upper panel) and 6 GHz (lower panel) for the pass-2 of the Tampa Bay Rain Experiment. Note that except for the color bar scales, these images are identical.

Next, the HIRAD forward RTM was run for each beam positions (21:301) in the cross-track plane to produce the modeled Tb image that corresponded to the measured NEXRAD rain rate vertical profiles. Finally, this process was repeated for the 661 scans to produce the modeled top of the atmosphere (TOA) Tb image for 5 GHz shown in Figure 5-13 (imagesc format). This is a unique contribution of this dissertation; whereby the measured rain rate 3D profiles were input to the RTM to produce the modeled TOA brightness temperatures for HIRAD.

5.2.3 Atmospheric Rain Component of Brightness Temperature

The innovative contribution of this dissertation deals with the retrieval of rain rate from the HIRAD TOA Tb measurements, and the above described forward radiative transfer model is an important part of this process. To better understand the quality of this modeling, it is important to partition the TOA Tb into a clear-sky component and a differential atmospheric rain component.

Basically, the effect of rain is increased absorption along the upwelling and downwelling paths, which increases both upwelling and downwelling atmospheric brightness, but the surface brightness at TOA decreases because of the decrease in the upward atmospheric transmissivity. The net effect is a monotonic increase in the TOA Tb with increasing rain rate. Therefore, the TOA brightness due to rain is:

$$T_{TOA_{rain}} = (T_{up_{clear}} + \Delta T_{up_{rain}}) + e^{-\tau}_{up_{clear}} * e^{-\tau}_{up_{rain}} * \Big(\varepsilon * SST + \Gamma * \big(e^{-\tau}_{dn_{clear}} * e^{-\tau}_{dn\_rain} * T_{cos} + T_{dn\_clear} + \Delta T_{dn\_rain}\big)\Big) \quad (5.11)$$

For rain conditions, separating this into the two components becomes:

$$T_{TOA\_rain} = T_{TOA\_clear} + \Delta T_{atmos\_rain} \quad (5.12)$$

$$T_{TOA\_clear} = T_{up\_clear} + e^{-\tau}_{up\_clear} * \Big(\varepsilon * SST + \Gamma * \big(e^{-\tau}_{dn\_clear} * T_{cos} + T_{dn\_clear}\big)\Big) \quad (5.13)$$

and

$$\Delta T_{atmos_{rain}} = T_{TOA\_rain} - T_{TOA\_clear} \quad (5.14)$$

Recognizing that: $e_{up\_clear}^{-\tau} * e_{up\_rain}^{-\tau} \approx e_{up\_rain}^{-\tau}$ and $\Gamma*(e_{dn\_rain}^{-\tau} * e_{up_{rain}}^{-\tau} - e_{dn\_clear}^{-\tau} * e_{up\_clear}^{-\tau})* T_{cos}$ < 1 K, which can be ignored; thus, solving for the atmospheric rain component, yields to:

$$\Delta T_{atmos\_rain} \approx \Delta T_{up_{rain}} + (e_{up_{rain}}^{-\tau} - e_{up_{clear}}^{-\tau}) * (\varepsilon * SST) + (e_{up_{rain}}^{-\tau} * \Gamma * \Delta T_{down_{rain}}) \quad (5.15)$$

Assume a uniform clear-sky scene (as the Tampa Bay case), then we calculate the change of the TOA Tb (due to rain) by subtracting the average clear-sky $< T_{TOA\_clear} >$.

$$\Delta T_{atmos\_rain} = T_{TOA\_rain} - < T_{TOA\_clear} > \quad (5.16)$$

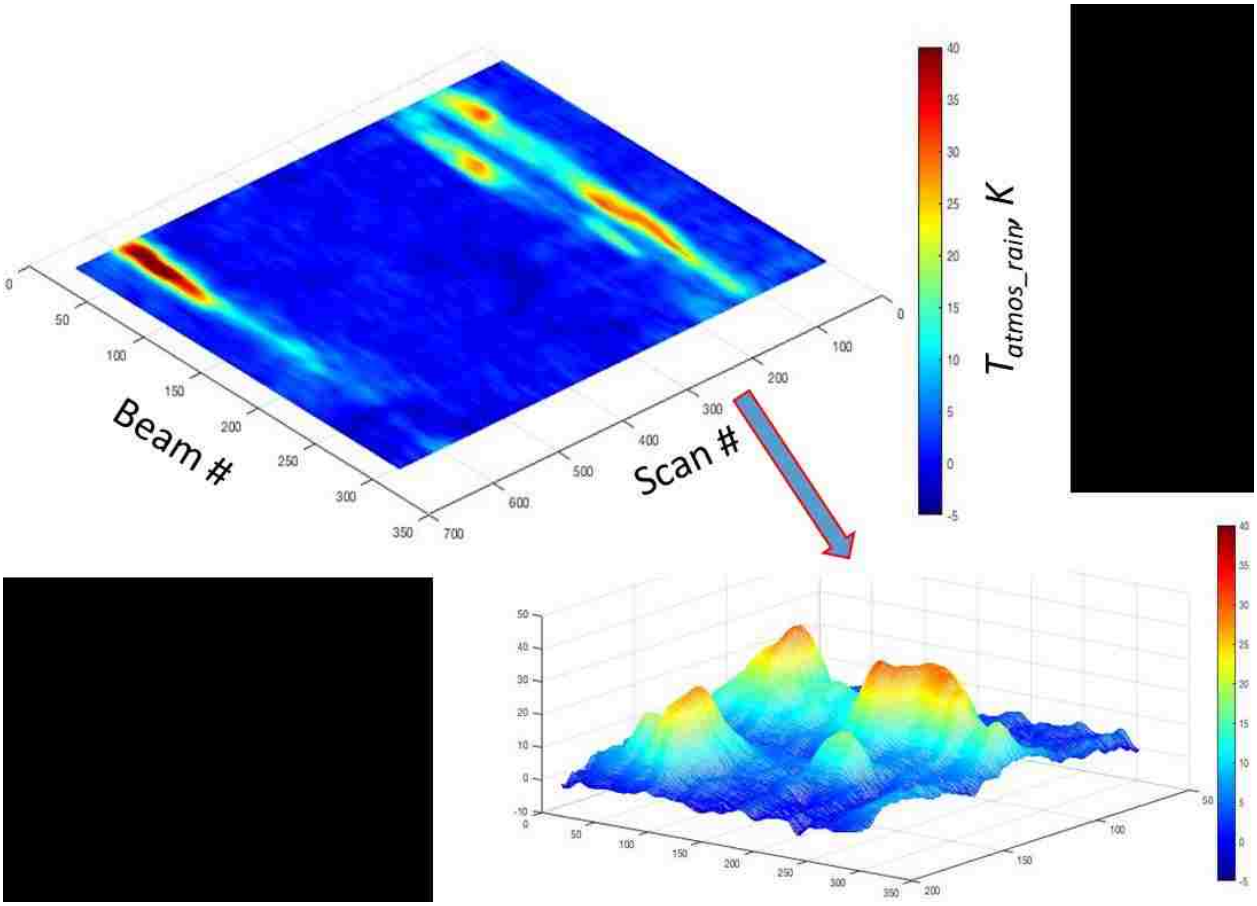

Figure 5-14: ΔT_{atmos_rain} for 5 GHz (imagesc format) for Global Hawk pass-2. Also shown in the lower panel is the 3D atmospheric component of rain brightness temperature.

For the Tampa bay Rain Experiment, the RTM was run, and the TOA Tb image was produced for both clear-sky and rainy conditions. Using Equation (5.16), the 5 GHz $\Delta T_{atmos\text{-}rain}$ was produced and is presented in Figure 5.14 (2D and 3D imagesc format).

Also, the resulting $\Delta T_{atmos\text{-}rain}$ for 5, 6 & 6.6 GHz are shown in Figure 5-15, and note the change in the Tb color scale with increasing frequency for the same rain rate.

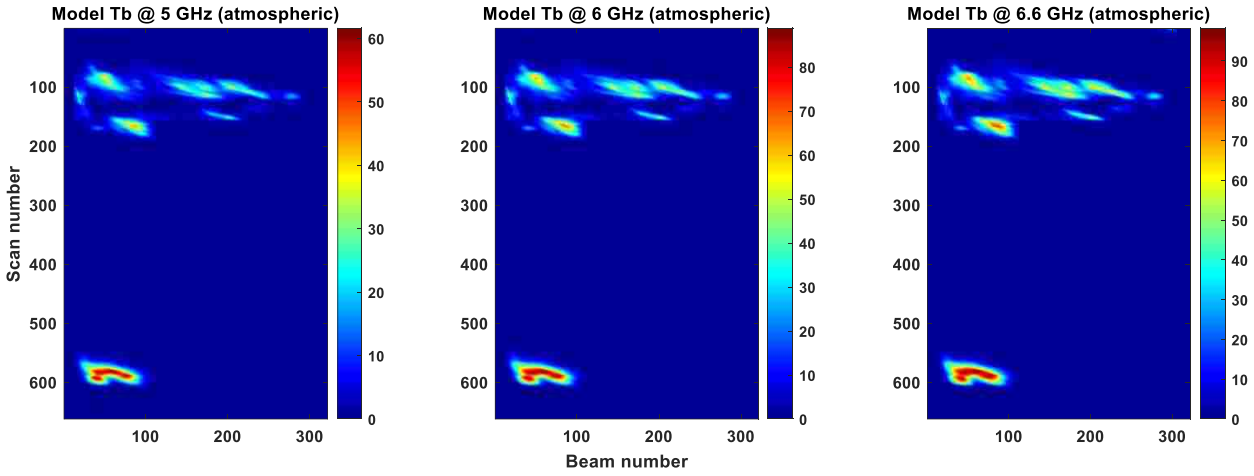

Figure 5-15: ΔT_{atmos_rain} for 5, 6 & 6.6 GHz (imagesc format) for Global Hawk pass-2.

5.2.4 Comparison of Measured and Modeled Top of Atmosphere Tb

Comparisons of modeled (left) and measured (right) Tb images are shown in Figure 5-16 for the tropical squall-line event in the upper half of Global Hawk path-2. First consider the clear-sky region, where the modeled image shows the expected ocean Tb signature of warm Tb in the center that symmetrically decreases in brightness to the edges of swath. Next considering the measured Tb image (right panel), these two images appear to be equal, which is typical of properly calibrated HIRAD ocean Tb images without rain.

Next, examine the modeled image and consider the collection of thunderstorm cells in the squall-line at the beginning of the flight path. There are five distinct convective rain cells that can be identified by the increased Tb (yellow to red colors). Now, compare this modeled rain (Tb) pattern with the corresponding measured HIRAD image, which indicates that the rain features are well represented in both images. Moreover, this indicates that the spatial/temporal alignment of

the NEXRAD images have provided good spatial registration with the independent HIRAD measurement.

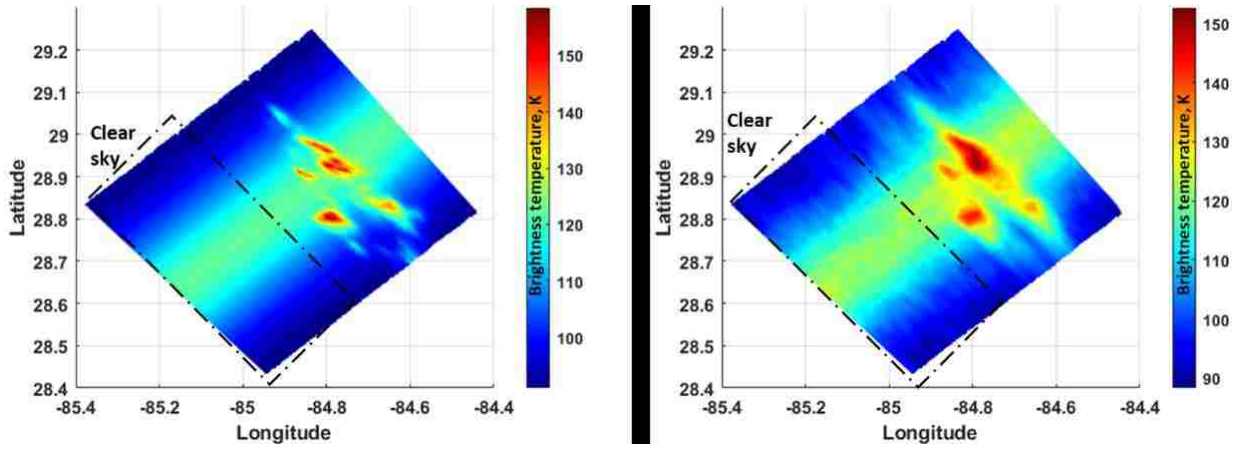

(**a**) (**b**)

Figure 5-16: Comparison of 5 GHz modeled (left) and measured (right) HIRAD TOA Tb images of the tropical squall-line for the upper half of Global Hawk path-2.

On the other hand, there were some minor differences between modeled and measured, which are important. For example, in the modeled Tb image between 29.0° and 28.9° latitude, there are three convective rain cells; however, in the corresponding location of the measured image, there appear to be only two. Thus, the measured Tb image appears to be smoothed compared to the higher contrast modeled image, which is expected because the measured brightness (T_{ant}) is a sum of all brightness incident on the antenna that are weighted by the HIRAD synthesized beam antenna gain pattern [26]. The resulting measured antenna temperature is the ratio of two double integrals in spherical coordinates (θ, ϕ & Ω), namely:

$$T_{ant} = \frac{\iint_{4\pi} T_{app}(\theta,\phi) * F_n(\theta,\phi) * d\Omega}{\iint_{4\pi} F_n(\theta,\phi) * d\Omega} \tag{5.17}$$

where the numerator is the convolution of the apparent brightness temperature scene $T_{app}(\theta, \phi)$ (surrounding the antenna) with the normalized antenna directional power gain pattern, $F_n(\theta, \phi)$, over the entire 4π steradians of a sphere, and the denominator is the total power collected by the antenna for a uniform scene = 1 Kelvin. Because the pole of the spherical coordinate system is aligned with the antenna look-direction (*EIA*), the corresponding normalized antenna pattern changes with *EIA* as discussed in Section 2.

As a result, the modeled Tb, without antenna pattern effects, shown in Figure 5-16 (a), represents the apparent scene brightness temperature with the HIRAD grid spatial resolution at the surface of about 150 m; while, the effective spatial resolution of the synthesized HIRAD measured Tb image (Figure 5.16 (b)) varies from ~ 2 km (middle of swath) to ~ 6 km (swath edge) [19, 20]. Therefore, before making a quantitative comparison between modeled and measured Tbs, the antenna pattern convolution (APCv) was performed (using the modeled Tbs), and the resulting modeled Tb image spatial resolution was degraded to ~ 1 km along track and ~ 2.5 km cross-track.

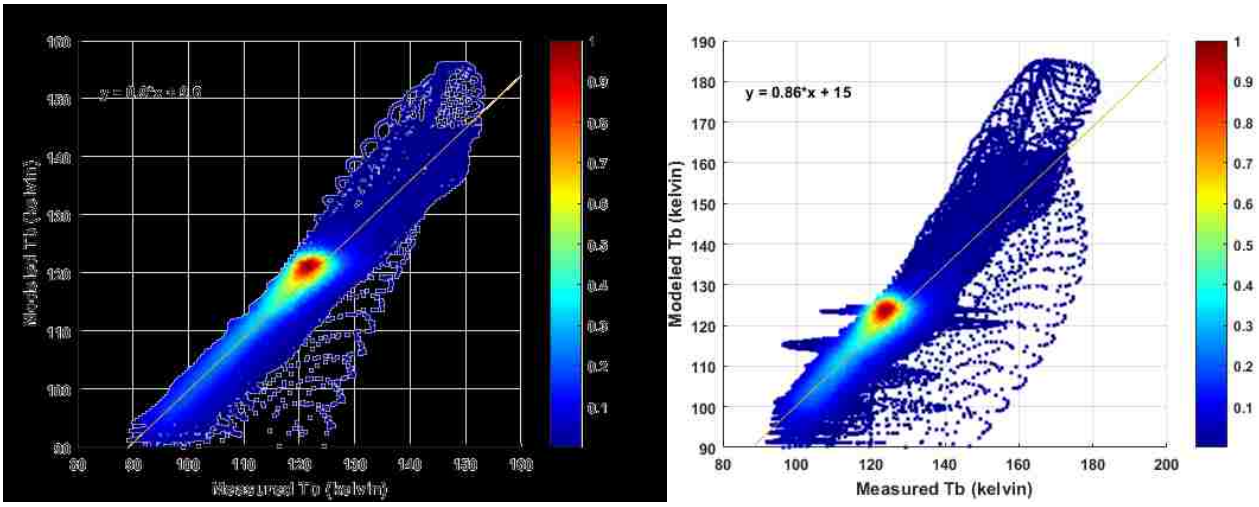

(**a**) (**b**)

Figure 5-17: Comparison of HIRAD measured and modeled (with APCv applied) Tb images for the flight pass-2 from 5 GHz (left) and 6 GHz (right), where the color represents the relative number of points.

First, using all pixels in pass-2, scatter diagrams were produced for 5 and 6 GHz between measured and modeled (with APCv applied) Tbs, and results are shown in Figure 5-17. In these comparisons, the points associated with clear-sky lay between 90 – 130 K, and they appear to be "tightly grouped along the linear regression line. On the other hand, at higher Tbs (associated with rain) there is considerably more divergence and the appearance of multiple paths for the grouping of points, which is an indication of spatial misregistration between these Tbs being compared.

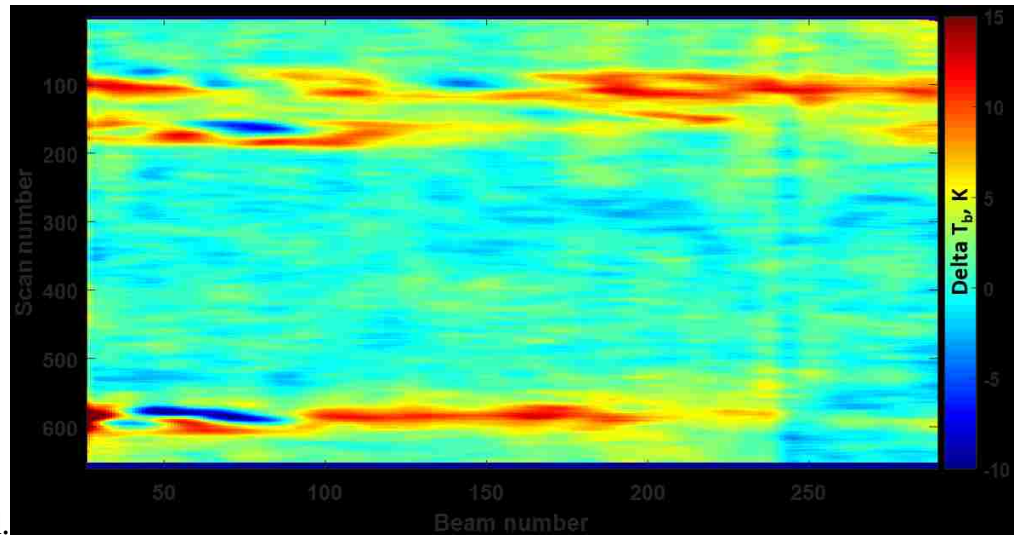

Figure 5-18: Matrix of HIRAD measured minus modeled (with APCv applied) Tb images for the flight pass-2, where the color represents the Tb difference in K.

To test this hypothesis of image mis-registration, the difference (between the measured and modeled Tb images) is plotted as a matrix in Figure 5-18, where the color scale is the corresponding Tb difference in K. The appearance of patterns of coupled blue (negative Tb) and red (positive Tb) features in the rainy regions is evidence that these two Tb images (associated with rain) are misregistered by a few km primarily in the along-track direction. Nevertheless, the linear regressions tend to average the comparisons, and the results for both 5 and 6 GHz scatter

diagrams are very good with slopes close to one and moderate offsets (see Table 5.1 at the end of this section). Since no normalization of the modeled nor measured rain rate magnitudes have been made in this comparison, this is a very significant finding, which implies the both the Z-R relation for the NEXRAD and the SFMR derived rain absorption coefficients are in good agreement.

To continue this comparison, the Tb images are partitioned into three regions, namely: "rain-1" (scans 50 to 200), "clear-sky" (scans 230 to 530), and "rain-2" (550 to 620). Consider first, the scatter diagrams for the clear-sky region, shown in Figure 5-19 for 5 and 6 GHz, where co-registration of measured and modeled images are not an issue. For both cases there is excellent agreement and the regression results are summarized in Table 5.1 and 5.2.

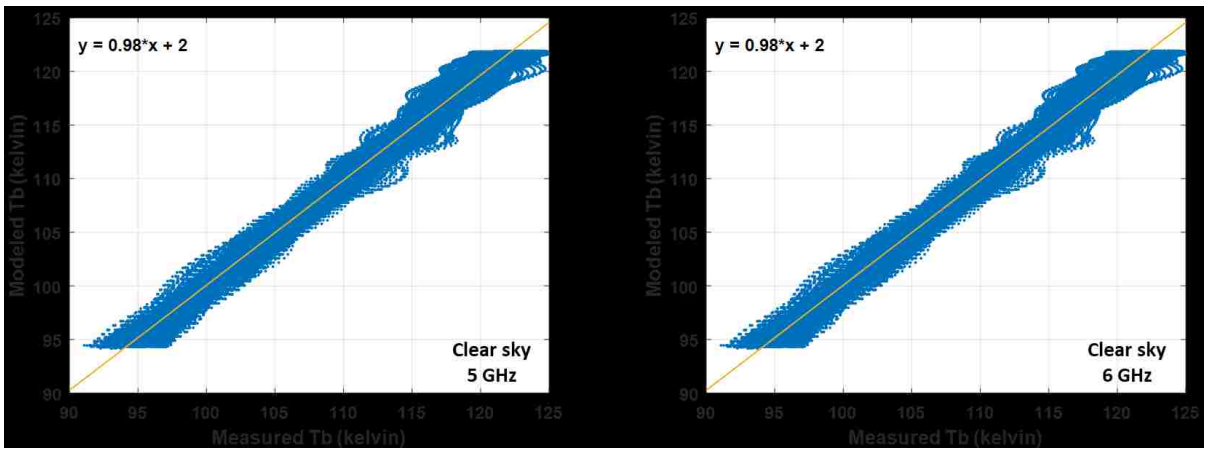

(**a**) (**b**)

Figure 5-19: Comparison of measured and modeled Tbs for the clear-sky region of pass-2 for 5 and 6 GHz.

Next, consider only the 5 GHz comparisons for the two rainy regions at the beginning (Rain-1) and end (Rain-2) of pass-2 that are combined in Figure 5-20. For this comparison, there is excellent agreement between measured and modeled, and the regression results (as well as results for 6 GHz) are summarized in Table 5.1 and 5.2.

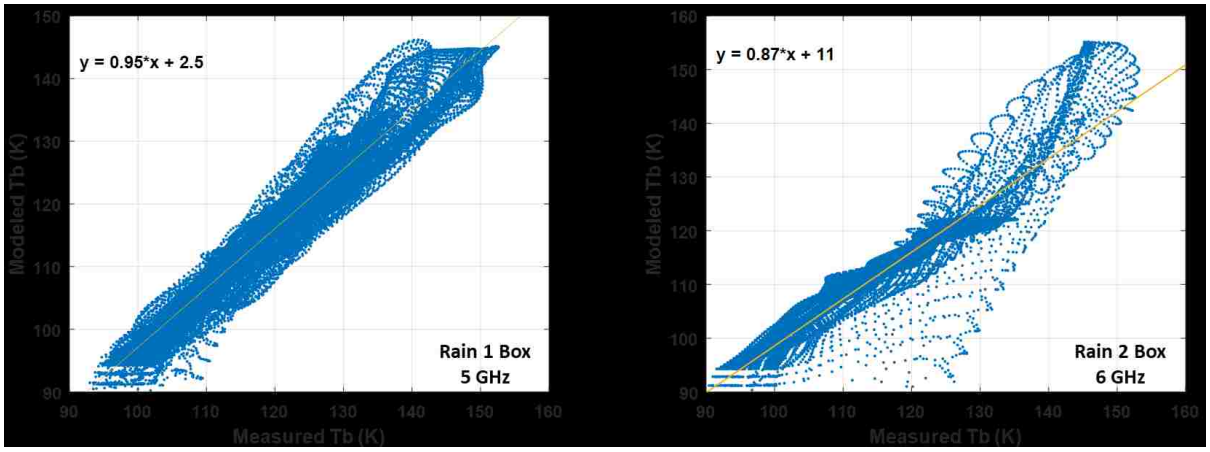

(**a**) (**b**)

Figure 5-20: Comparison of measured and modeled Tbs for the rainy regions (1 & 2 combined) of pass-2 for 5 GHz.

5.2.5 Comparison of Measured and Modeled Differential Rain Atmospheric Tb

Next, the average clear-sky brightness component of TOA Tb was removed using equation (5.16), and the comparison was made between the measured and modeled Tb components due to rain (ΔT_{atmos_rain}) over the entire flight pass-2. To match the spatial resolution of these two images, the APCv was applied to the modeled data, and the resulting images (in matrix format) for 5 GHz are shown in Figure 5-21, with rain occurring at the beginning and end of the leg. Qualitatively, there is a high degree of spatial correlation in these two images, but the magnitudes of the rain Tbs were slightly different as indicated by the RR color scales.

Further, in Figure 5-22, typical examples of the cross-track Tb profiles of ΔT_{atmos_rain} (for scan # 110 and both the 5 and 6 GHz channels) are presented, which illustrate the high degree of agreement in the small-scale rain features of these corresponding Tb images. In the left panel (a), the measured (solid line) and modeled (dashed line) atmospheric Tb components are presented for 5 GHz, and in the right panel (b) the corresponding plots are given for 6 GHz. For both plots,

there is excellent correlation in the dynamic change of the rain signals, although the measured and modeled curves have a small bias (< 10 K). When considering the heterogeneous nature of the propagating squall-line of thunderstorms, these independent comparisons are considered quite remarkable.

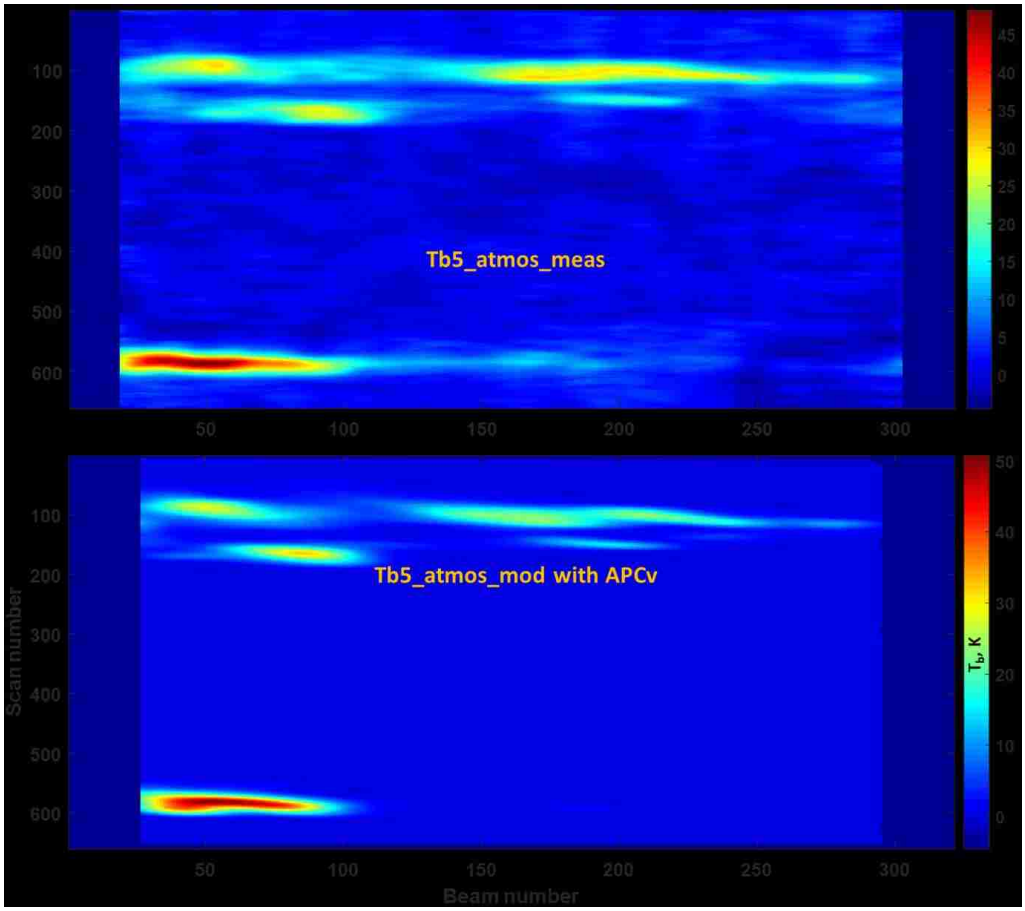

Figure 5-21: Differential atmosphere brightness component because of rain (matrix format) for 5 GHz. Upper panel is HIRAD measured and lower panel is modeled with APCv applied.

Finally, a measure of the cross-correlations between these ΔT_{atmos_rain} Tb components (for both 5 GHz and 6 GHz) is presented in Figure 5-23 in the form of two scatter diagrams with linear regressions applied. As discussed previously, the relatively large spread in these scatter

diagrams are probably due to imperfect coregistration of the NEXRAD and the HIRAD measurement, but the linear regressions show good correlation.

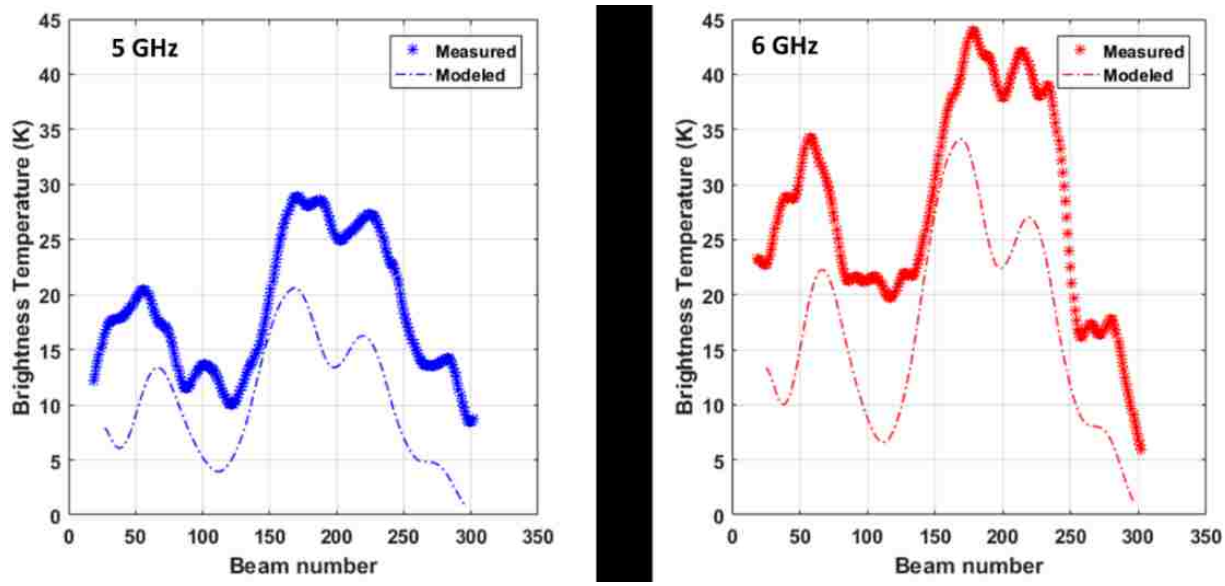

(**a**) (**b**)

Figure 5-22: Comparisons of the small-scale rain features in the cross-track differential rain atmosphere brightness components for scan 110 for: (a) 5 GHz and (b) 6 GHz.

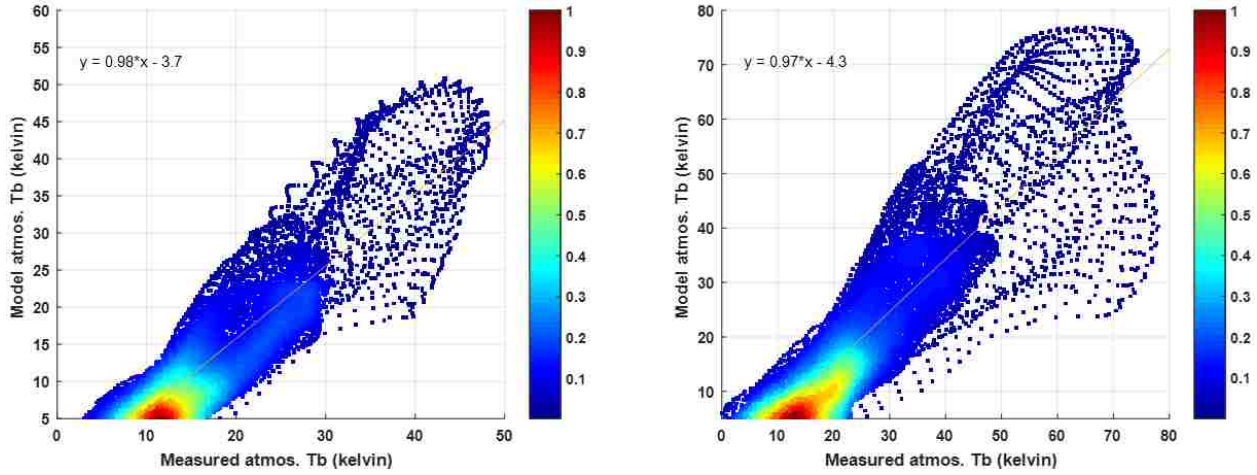

(**a**) (**b**)

Figure 5-23: Correlation of measured and modeled differential rain atmosphere brightness components for Global Hawk pass-2 for: (a) 5 GHz and (b) 6 GHz.

Results, for four different cases of comparisons of measured and modeled TOA Tbs, are summarized in Table 5.1 (5 GHz) and 5.2 (6 GHz), as well as, a single case for comparisons of the measured and modeled atmospheric Tb component due to rain. This table provides pertinent statistics for different spatial regions, which includes for Tbs in clear-sky and rainy regions (at the beginning (R1) and end (R2) of the flight pass-2).

Table 5-1: Comparisons of Measured and Modeled Tbs for 5 GHz.

Region Pass-2	Model Tb Dynamic Range Max/Min, K	Measurement – Model (APC) Mean/STD, K	Regression Slope/Offset
All points scans (1:661)	155/90	1.79/2.84	0.9/9.6
Clear-sky scans (230:530)	121/90	0.21/1.05	0.98/2.0
Rain – 1 scans (50:170)	146/90	3.98/3.03	0.95/2.5
Rain – 2 scans (550:620)	155/90	4.02/4.07	0.87/11.0
Tb atmos.	50/0	1.52/2.69	0.98/-3.70

Table 5-2: Comparisons of Measured and Modeled Tbs for 6 GHz.

Region Pass-2	Model Tb Dynamic Range Max/Min, K	Measurement – Model (APC) Mean/STD, K	Regression Slope/Offset
All points scans (1:661)	185/90	2.59/4.83	0.86/15.0
Clear-sky scans (230:530)	124/90	0.44/2.46	0.9/11.0
Rain – 1 scans (50:170)	168/90	4.96/4.77	0.93/3.5
Rain – 2 scans (550:620)	185/90	6.62/7.18	0.93/2.2
Tb atmos.	76/0	2.18/4.62	0.97/-4.30

Overall there were excellent qualitative comparisons showing nearly identical rain images (shape and intensity), however there were minor registration errors between HIRAD and NEXRAD. On the other hand, a variety of quantitative evaluations, presented in Table 5.1 (5 GHz) and Table 5.2 (6 GHz), are highly supportive of the quality of the forward RTM. The fact that, the slopes of the various linear regressions (given in Table 5.1 and 5.2) are close to unity and the offsets are also small, is very significant. This implies that both the Z-R relation for NEXRAD and SFMR derived rain absorption coefficients are in good agreement. Moreover, it is important to note that no normalization of the modeled rain rate nor the brightness temperatures have been made in these comparisons.

CHAPTER 6:
HIRAD RETRIEVAL

6.1 MLE Algorithm

The original HIRAD hurricane Maximum Likelihood Estimation (MLE) retrieval algorithm was developed by Amarin [5, 6], to estimate the ocean surface wind speed and rain rate on a pixel by pixel basis in the cross-track plane. This retrieval algorithm (Figure 6-1) uses the HIRAD multi-frequency brightness temperature observations and a set of a priori modeled Tbs, to estimate the corresponding WS and RR that results in the least square difference of the following cost function:

$$Cost\ Function = \sum_{freq=1}^{4}\left(Tb_{measured\_freq} - Tb_{model\_freq}\right)^2 \tag{6.1}$$

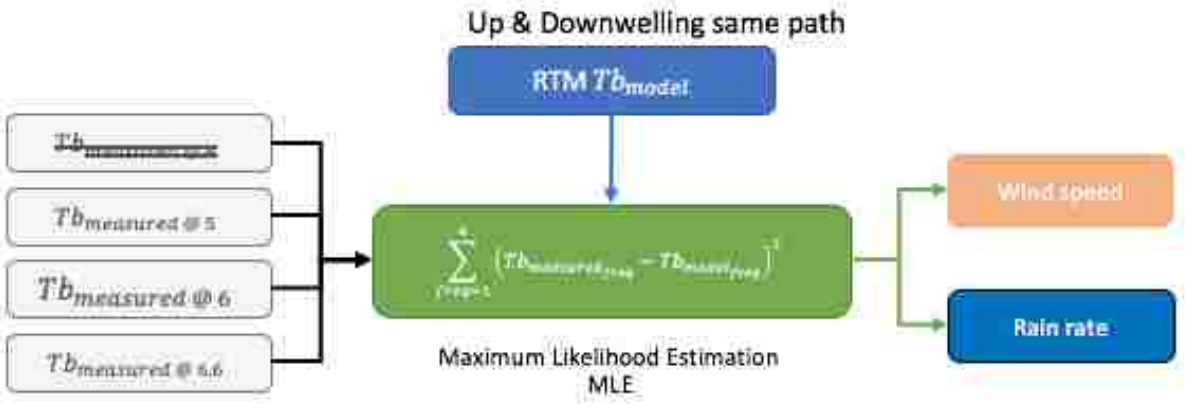

Figure 6-1: HIRAD MLE geophysical retrieval algorithm. Note that the 4 GHz channel was inoperative for this dataset.

Thus, the cost function is evaluated using all possible combinations of WS (rows) and RR (columns), to produce a 2D surface (for each cross-track beam position); whereby the location of the minimum value corresponds to the retrieved WS and RR.

A major part of this algorithm is the generation of the a priori modeled Tb tables, using the forward RTM (shown in Figure 6-2), which are matrices of theoretical Tbs for a wide range of assumed "trial" wind speeds and rain rates. There are separate tables for all possible incident angles (beam #) and the four frequencies, and these tables represent the totality of possible Tbs that can be observed by HIRAD.

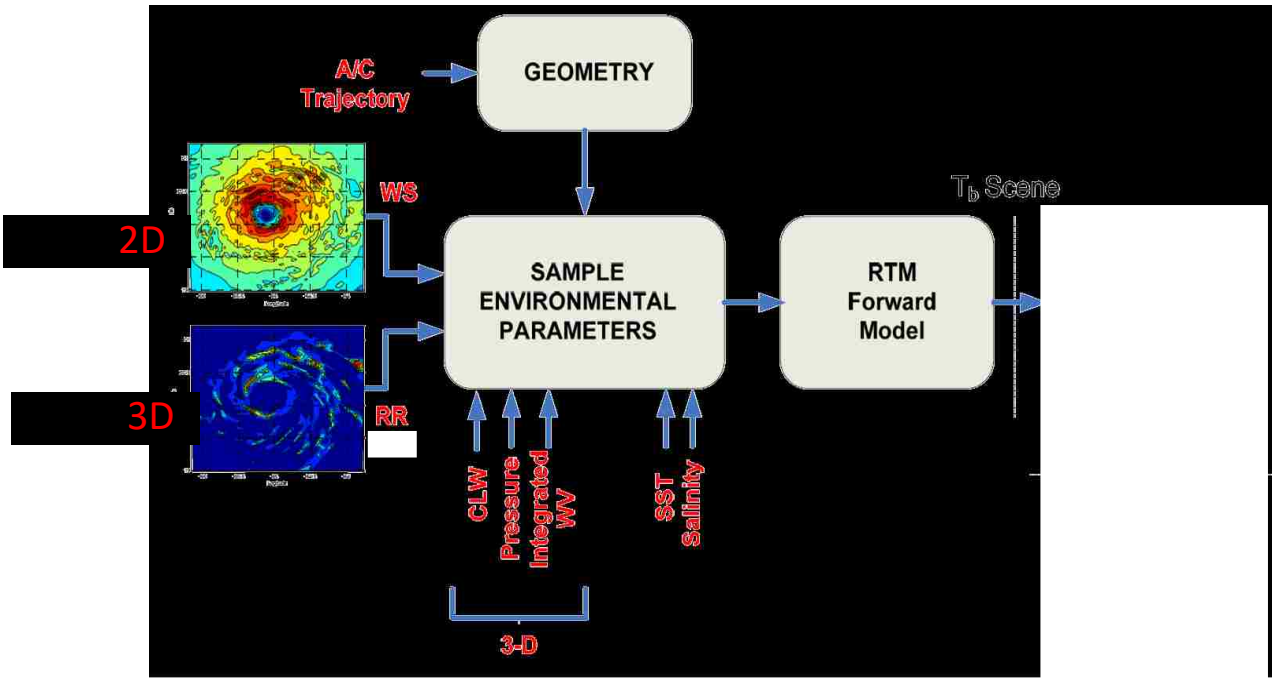

Figure 6-2: HIRAD forward radiative transfer model from Amarin [6].

Concerning the RTM environmental parameter inputs (e.g., SST, atmospheric temperature, pressure and water vapor profiles, etc.), a fixed hurricane database is used. However, for the unknown rain rate input, we use a constant value for both the upwelling and downwelling paths up to 5 km altitude that ranges from (0 - 100, mm/h); and for the unknown wind speed input, we use a constant value that ranges from (0 - 70, m/s). Therefore, using these environmental parameters in the forward RTM, produces a series of 2D tables, with integer wind speed indices

(0.2 m/s steps) and integer rain rate indices (0.2 mm/h steps) that are the matrix rows and columns respectively.

6.2 Geophysical Retrieval Algorithm Evaluation using Modeled Tbs

In remote sensing, it is a common practice to perform a "necessary but not sufficient" (sanity) test to evaluate the performance of an MLE geophysical retrieval algorithm. In this test, "simulated sensor measurements" are generated (using the forward RTM) with arbitrary environmental parameters. Next, these simulated measurements are the input to the retrieval algorithm (using the a priori modeled tables from the same forward RTM) to retrieve the geophysical parameters, which are the WS and RR that minimize the cost function (Equation 6.1). For this "perfect case", there should be an exact match between the arbitrary WS and RR parameters, used to generate the sensor inputs and output geophysical parameters, and any differences between these are attributed to algorithmic error (i.e., a failure of the retrieval algorithm to duplicate the MLE process).

Thus, an evaluation test was performed for the TAMPA Bay Rain Experiment, but now with simulated TOA HIRAD Tbs (Section 5.2.2), using the improved HIRAD forward RTM with the measured NEXRAD 3D rain rates, which resulted in different RR profiles along the up- and downwelling paths. Next, these calculated Tb data were used as sensor inputs to the HIRAD MLE retrieval algorithm described above (Section 6.1). It is important to note that this test is NOT the "perfect evaluation case", because slightly different RTM's were used: (1) to simulate the measurements (independent up- and downwelling paths) and (2) to produce the a priori model Tb tables (assumed constant RR over both paths).

The images of retrieved WS and RR for the Global Hawk pass-2 are presented in Figure 6-3, where the left panel is WS in m/s and the right panel is RR in mm/h. For WS the results are as expected, and the spatial distribution of retrieved WS being very similar to the assumed constant WS = 6 m/s input.

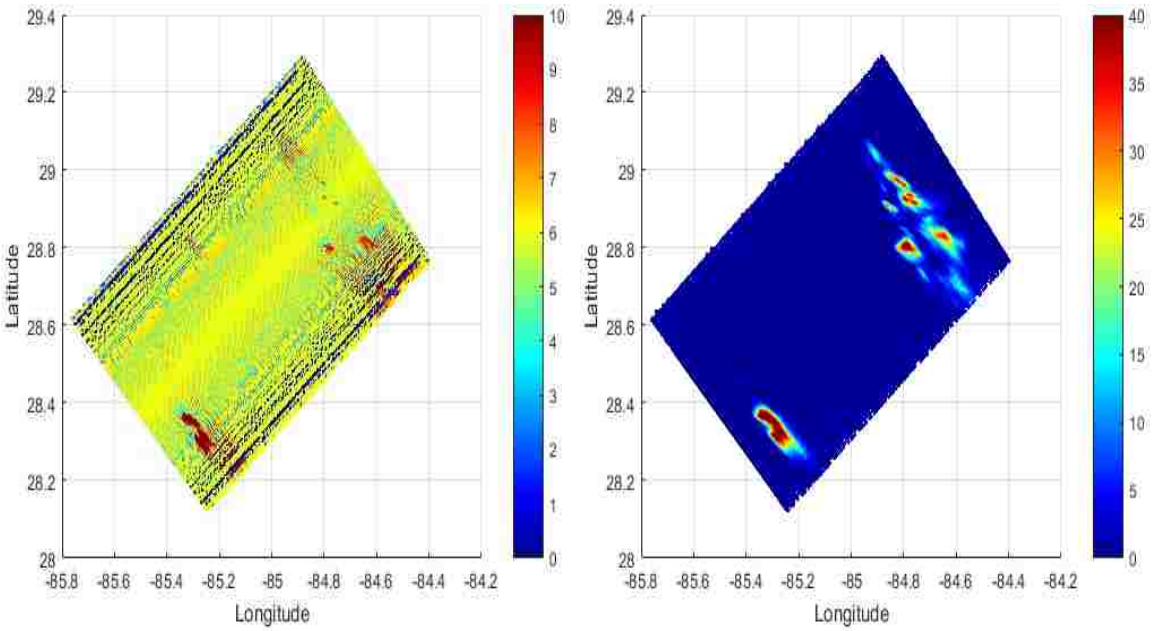

Figure 6-3: HIRAD Retrieved wind speed (left) and rain rate (right) using the modeled Tbs generated using NEXRAD measured RR into separate up and downwelling paths.

Next consider the RR retrievals, which were evaluated using comparisons made with the independent measured NEXRAD 3D RR. For this analysis, the issue is: what is the "metric" for comparing a 2D retrieved RR (RRR) with the 3D surface truth RR measurement? Certainly, for a given HIRAD retrieval (at a selected beam position), only rain along the upwelling and downwelling paths are "seen" by HIRAD. Therefore, we selected the path average NEXRAD rain rate along the RTM upwelling and downwelling paths (from the surface to 5 km altitude), which is designated as NRR, and the corresponding images of RRR and NRR are shown in Figure 6-4.

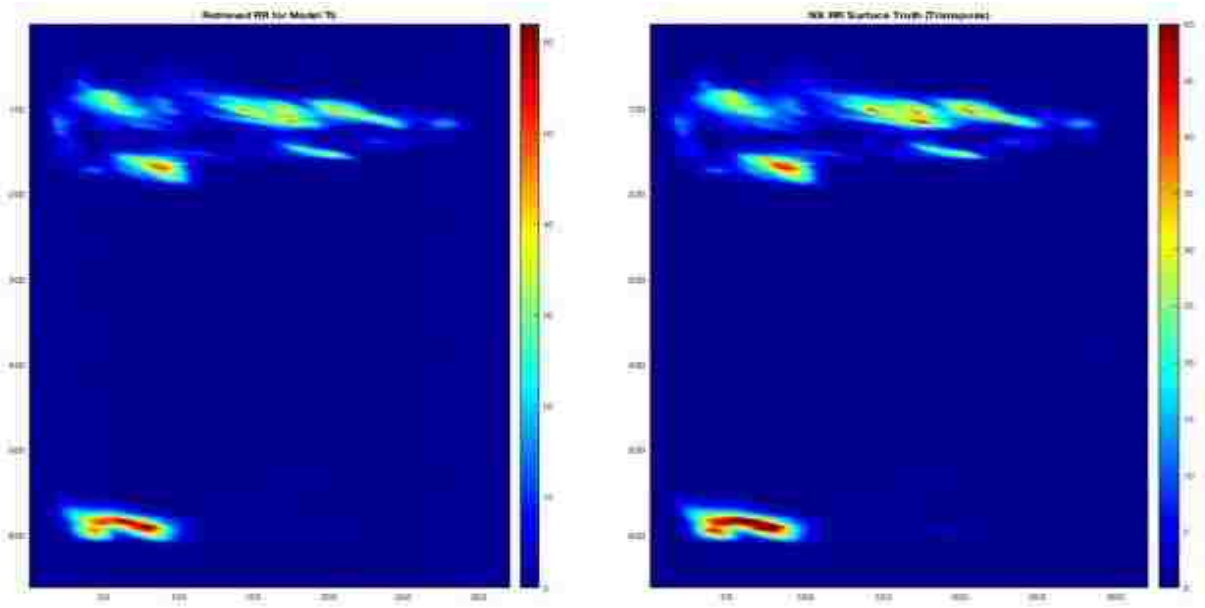

Figure 6-4: HIRAD (model Tb) Retrieved RR (left panel) and the path average NEXRAD RR surface truth (right panel).

Next, using the RRR and NRR data, we constructed a 4-color diagram (imagesc format) shown in Figure 6-5. This 4-color diagram is basically the sum of two binary (rain/no-rain) matrices for a given rain rate threshold (Ro). For this example, we assign the following values: "NRR no-rain" = 0 and "NRR rain > Ro" = 0.5 and "RRR no-rain" = 0 and "RRR rain > Ro" = 1.0. Thus, when the elements of both matrices are: "no-rain", the sum = 0, and when the elements of both matrices are: "rain > Ro", the sum = 1.5. If NRR matrix element is "no-rain" and the RRR element is "rain > Ro", the value is 1.0 and finally, if NRR = "no-rain" and RRR is "rain > Ro", the value is 0.5. Thus, the comparison between the retrieved RR and the surface truth is captured in the colors of the diagram, which are defined in the following manner:

Value/Color	MLE Retrieval Skill (compared to NRR surface truth)
1.5/Red	% of retrieval rain pixels correctly identified
1.0/Orange	% of false retrieval rain pixels

0.5/Light blue % of missed retrieval rain pixels

0/Dark blue % No-rain pixels correctly identified

Note that the sum of "red" and Orange" categories are 100%.

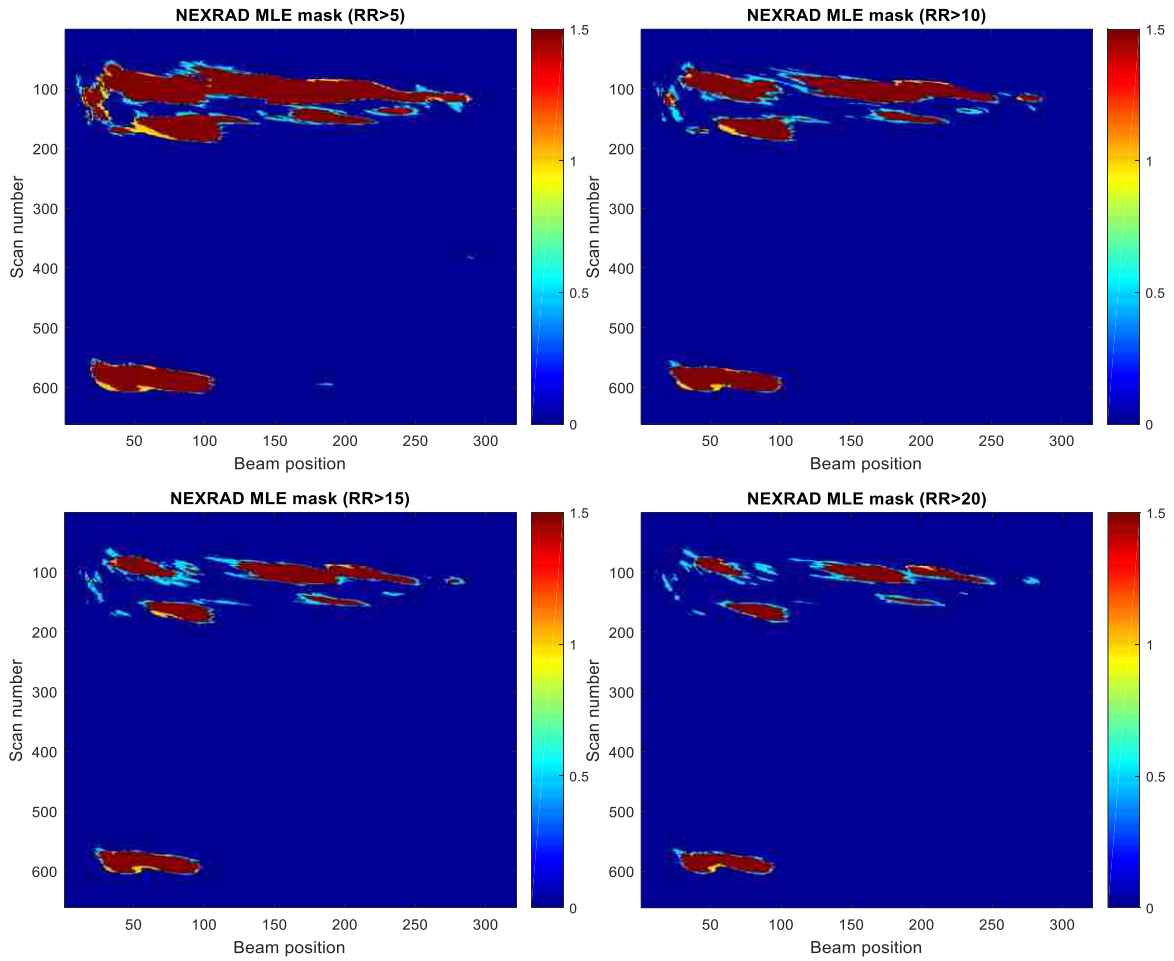

Figure 6-5: 4-color diagrams (imagesc format) between HIRAD (model Tb) retrieved RR and the path average NEXRAD RR (along the up and down welling paths) for Ro thresholds: 5mm/h (upper left), 10mm/h (upper right), 15mm/h (lower left) and 20mm/h (lower right).

As shown in Figure 6-5, the majority of retrieved rainy pixels are properly identified, regardless of the RR threshold selected (see Table 6.1); and there are small % of missed and false rain pixels selected, which indicate that the retrieval algorithm performs well.

Table 6-1: RR Retrieval for Modeled Tbs relative to Surface Truth

	Rain Rate Threshold			
	5 mm/h	10 mm/h	15 mm/h	20 mm/h
Correct RR	99.90	100.0	100.0	100.0
FALSE	11.43	16.41	19.25	23.89
Missed	0.10	00.0	00.0	00.0
No-rain	99.06	99.22	99.40	99.50

Now, consider Figure 6-6, where we show the histogram (right panel) of the differences between the surface truth (NRR) and the retrieval (RRR), and the corresponding scatter diagram (left panel). All these comparisons indicate a high degree of correlation between the retrieved RR and the NEXRAD surface truth RR values, which were used in the simulation.

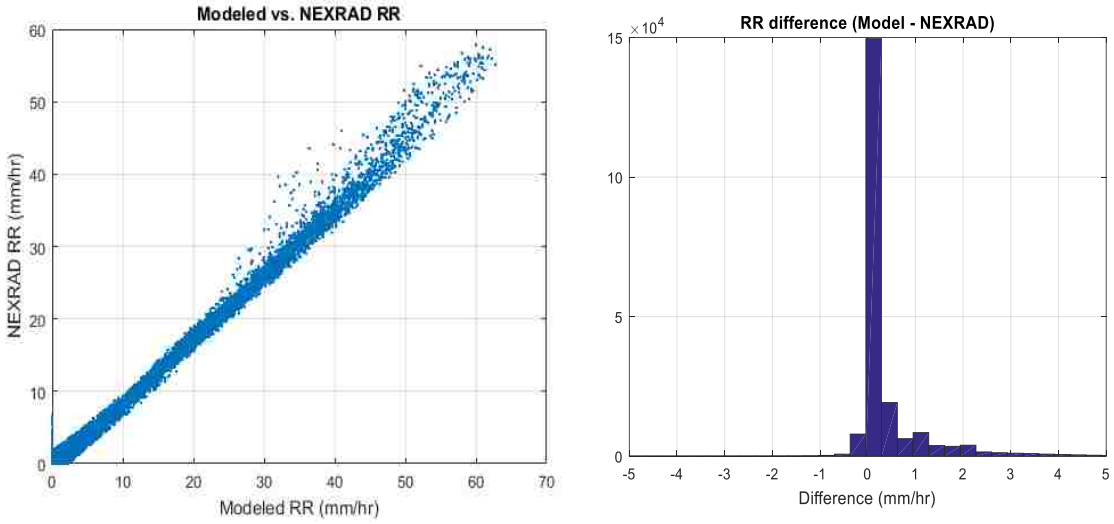

Figure 6-6: Comparison of NEXRAD surface truth rain rates and HIRAD retrieved rain rates (sanity case). The right panel is the histogram of the rain rate differences and the left panel is the corresponding scatter diagram.

Next, we performed a simulation to consider the effect of the spatial resolution of the simulated Tb image on the MLE retrieval. For this case, we degraded the resolution of the

simulated Tb by performing an antenna pattern convolution (APCv), which became the "new" measured Tbs. Using these new Tbs, the MLE retrievals were repeated and the resulting WS and RR retrieval images are shown in Figure 6-7, and the corresponding 4-color diagrams are given in Figure 6.8.

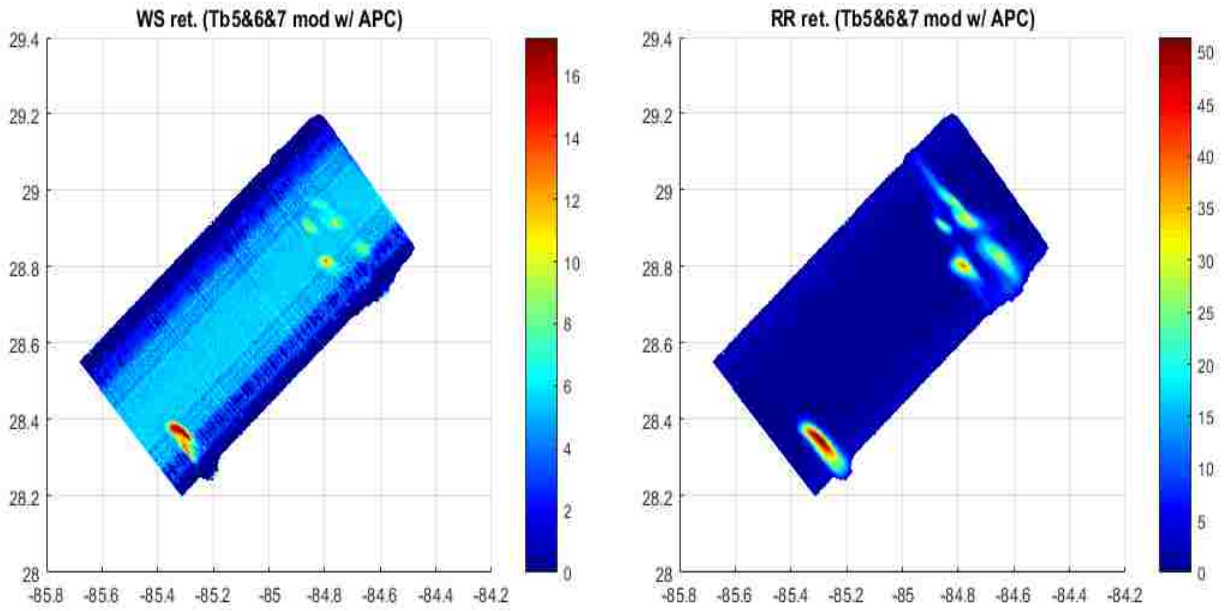

Figure 6-7: Simulated HIRAD retrieved wind speed (left) and rain rate (right) using the simulated modeled Tbs measurements with antenna pattern convolution applied.

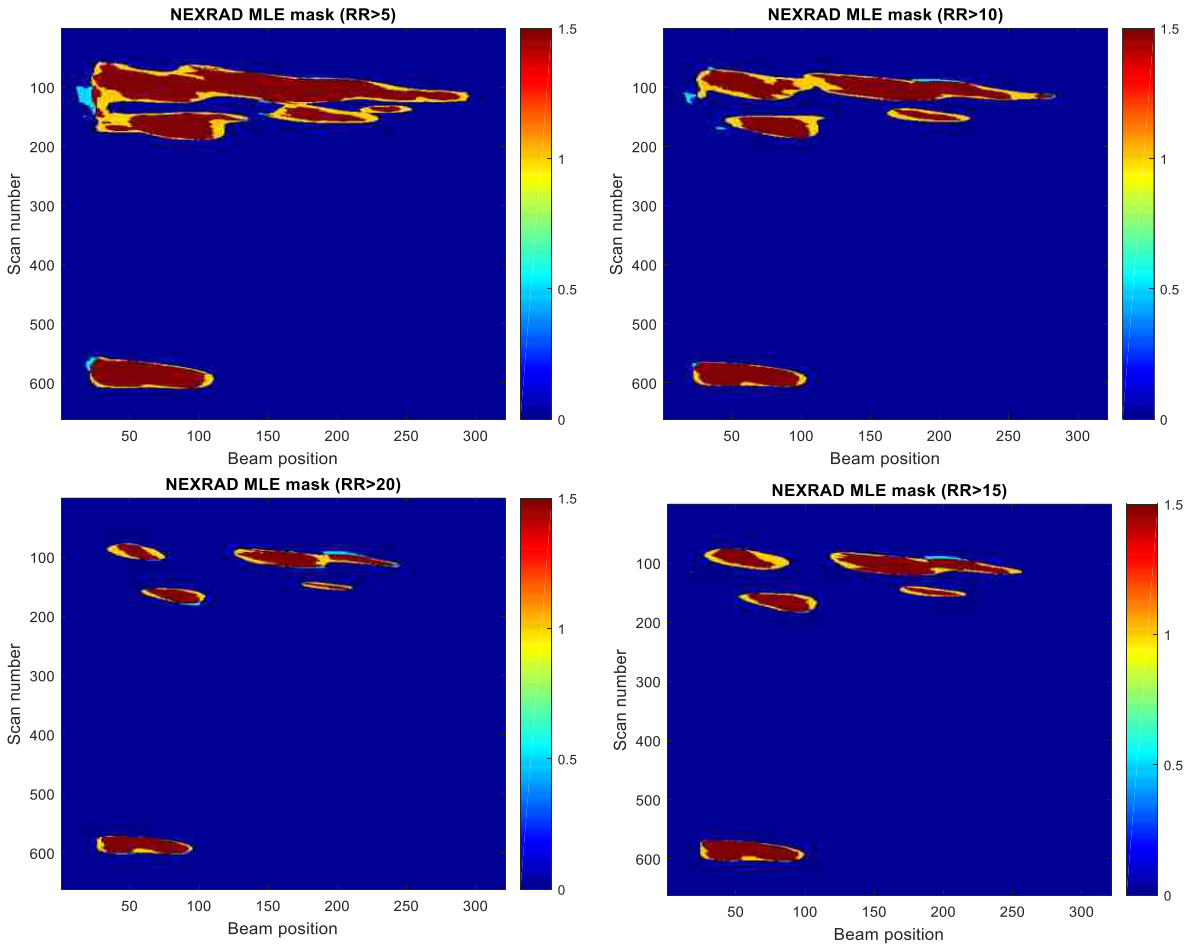

Figure 6-8: 4-color diagrams (imagesc format) between retrieved RR (with APCv) and the surface truth RR (average NEXRAD RR along the up and down welling paths) for various Ro thresholds.

Table 6-2: RR Retrieval for Modeled Tbs with APCv relative to Surface Truth

	Rain Rate Threshold			
	5 mm/h	10 mm/h	15 mm/h	20 mm/h
Correct RR	96.68	96.78	97.03	93.23
FALSE	32.62	37.74	33.94	32.93
Missed	3.32	3.22	2.97	6.77
No-rain	97.32	98.2	98.95	99.31

By comparing Table 6.1 and Table 6.2 we can separate the MLE algorithm implementation error (caused by the model Tb tables being produced using constant RR for up and downwelling paths) and the error associated with the antenna pattern convolution. Recognizing that the "correct RR" + "missed RR" = 100%, we see that the APCv causes about 3 – 6% missed RR pixels. This could be caused by the APCv smearing of the Tb, which reduced the magnitude of the RR retrieval and caused a few of retrievals to fall below the Ro threshold. Considering false alarms, the MLE implementation error causes 10% - 25% increase in the false RR pixels, whereas the APCv error monotonically increases the false RR pixels by a factor of 3x for Ro = 5 mm/h and by a factor of 1.5x for Ro = 20 mm/h, which is not a significant factor for a geophysical measurement of rain.

6.3 Geophysical Retrieval Algorithm Evaluation using Measured Tbs

The HIRAD MLE retrieval algorithm as evaluated by Amarin [5, 6], was found to be quite robust given zero mean random errors. However, when she performed her Monte Carlo statistical simulation, she did not consider random Tb biases in multiple channels, which we now recognize are a major issue with the HIRAD radiometric performance. Based upon the research of Sahawneh [19], we now better understand that the MLE is a very sensitive process to small errors in the measured Tbs; and this is especially true for differential Tb calibration errors that causes Tb biases between channels. Further, because the RR Tb signal is much stronger than the WS signal, the poor radiometric performance (accuracy and stability) of HIRAD Tb measurements is enough to cause a quasi-binary effect between the retrieved WS and RR.

For example, consider a typical HIRAD retrieval using measured Tbs, given in Figure 6-9. It is noted that where the retrieval gives rain, the corresponding retrieved WS is ~ zero; and vice

versa. In cases with accurate Tbs (such as described above for the modeled Tb cases), the cost function residual is generally < 1 K, which leads to both accurate WS and RR retrievals. On the other hand, for typical HIRAD measured Tbs, the cost function minima is quite broad and shallow (residuals of several K), which leads to large errors in both WS and RR. Then, the challenge for this dissertation is to separate poor radiometer performance (i.e., random Tb biases) from RR retrieval algorithm performance.

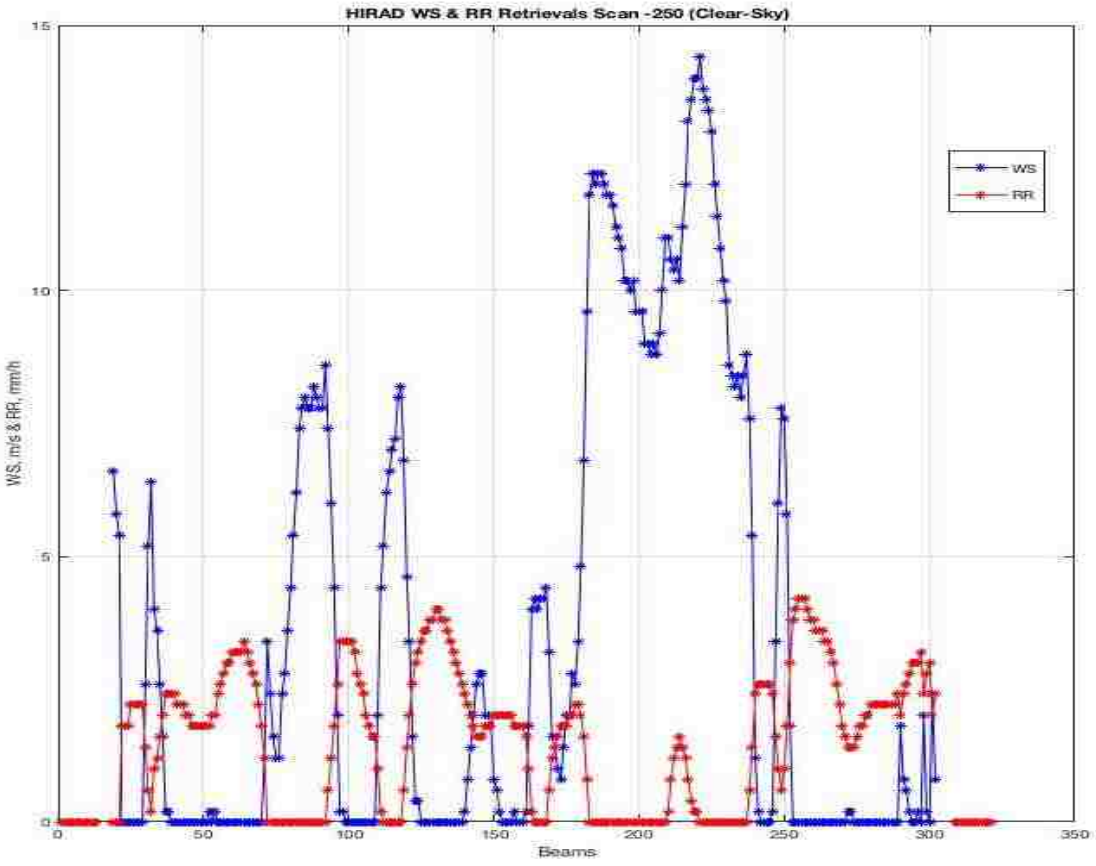

Figure 6-9: Typical HIRAD retrievals of wind speed (blue) and rain rate (red) using Tb5, Tb6 & Tb6.6 measurements. Note the quasi-binary nature of the cross-correlation between WS and RR.

With this introduction, consider MLE retrievals using adjusted measured HIRAD Tbs for pass-2 of the Tampa Bay Rain Experiment that are shown in Figure 6-10. First, examine the retrieved wind speed (left panel) in the middle clear-sky region of the leg, which appears to be acceptable retrieved WS (compared to the GDAS estimate of 6 m/s). However, a more careful examination, shows the dark blue stripes (zero WS), which are anomalous (non-geophysical). Further, in the regions where there is rain (beginning and end of leg-2), the retrieved WS appear to be too high with values of 10 - 25 m/s and with stripes of zero WS. So, unlike the modeled Tb case, where the WS retrievals were good (Figures 6.3 & 6.7), for this case (using adjusted measured Tbs) the MLE retrieval fails. On the other hand, the RR retrievals (right panel) appears qualitatively to be acceptable.

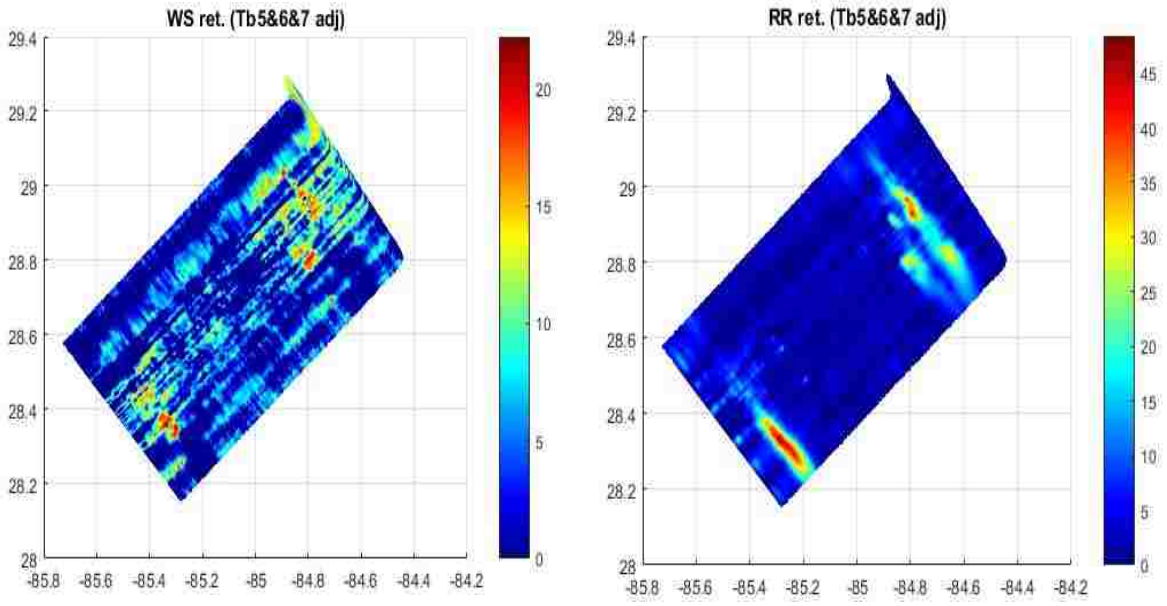

Figure 6-10: Retrieved wind speed (left) and rain rate (right) using HIRAD measured Tb.

Next, consider Figure 6-11, the 4-color diagram (imagesc format) comparison between the HIRAD RR retrieval (HRR) and the NEXRAD RR surface truth (NRR), where the color is red corresponds to the retrieval RR and surface truth agree, the yellow color is retrieval false rain

(compared to NRR), the light blue color corresponds to HRR missed rain and dark blue is the region of no rain. Quantitative results of the 4-color comparison are given in Table 6.3.

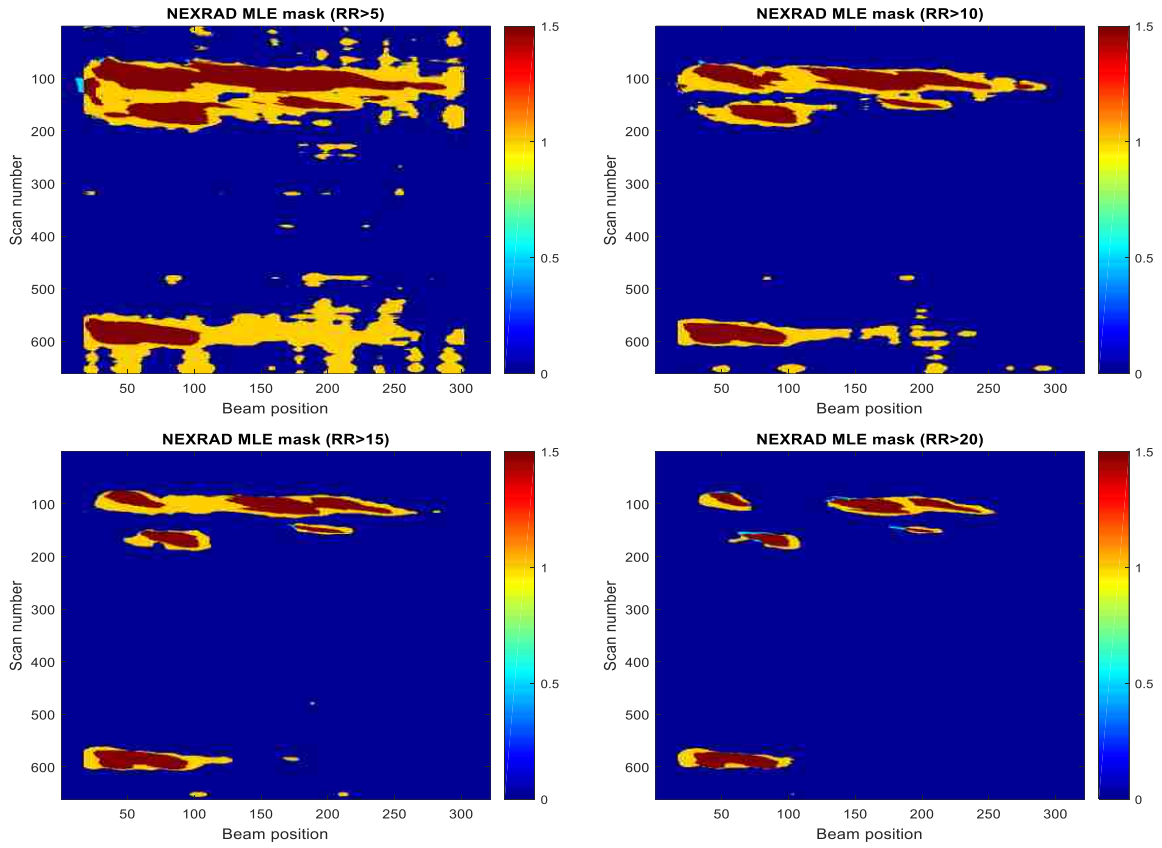

Figure 6-11: 4-color diagrams (imagesc format) using HIRAD (measured Tb) retrieved RR and path average NEXRAD RR surface truth, for four rain rate thresholds.

Table 6-3: RR Retrieval for Measured Tbs relative to Surface Truth

	Rain Rate Threshold			
	5 mm/h	10 mm/h	15 mm/h	20 mm/h
Correct RR	98.85	99.50	99.48	94.17
FALSE	210.98	142.34	113.62	78.20
Missed	1.15	0.50	0.52	5.83
No-rain	82.65	93.19	96.47	98.36

Compared to the RR retrievals for the modeled Tb with APCv (Table – 6.2), these RR retrievals are also excellent (essentially equal for the % of red pixels), but they produce 6 times the number of false RR pixels for Ro > 5 mm/h, which reduces to 2x for Ro > 20 mm/h.

Next consider Figure 6-12, where we show the histogram of the differences between NRR and HRR (right panel) and the corresponding scatter diagram (left panel) with high variability, which could be indicative of mis-registration between the true rain features (that produced the HIRAD Tbs) and the NEXRAD 3D RR measurements.

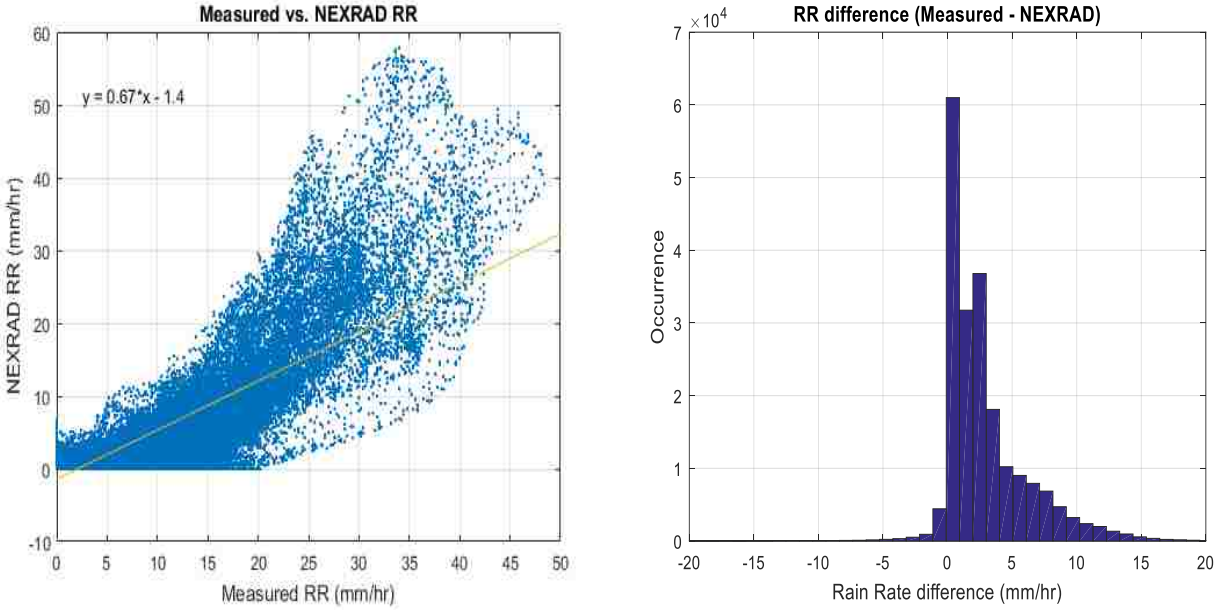

Figure 6-12: Comparison of HIRAD retrieved rain rates (measured Tbs) with NEXRAD RR surface truth. The right panel is the histogram of the rain rate differences and the left panel is the corresponding scatter diagram.

CHAPTER 7:
CONCLUSIONS AND RECOMMENDATIONS

This dissertation is the fourth in a series of PhD dissertations, from the Central Florida Remote Sensing Laboratory, in support of the Hurricane Imaging Radiometer (HIRAD) research; and the goal of this dissertation focuses on the retrieval of rain rate in hurricanes, using the multi-frequency brightness temperatures (Tbs) measured by HIRAD. The history of HIRAD's research at CFRSL has involved both theoretical and empirical components, and the progress has been difficult because of two aspects: (1) the difficulty of obtaining HIRAD hurricane observations with associated "surface truth" and (2) the issues associated with the HIRAD instrument performance.

Nevertheless, for this dissertation, the objectives are well defined, and results presented herein are a significant advancement in the state of knowledge for passive microwave remote sensing of precipitation using a 1D Synthetic Thinned Array Radiometer. The conclusions of this research and the recommendations for future research are summarized in this chapter.

7.1 Dissertation Accomplishments

The major accomplishments completed under of this dissertation were:

1. the collection of available remote sensing digital data sets from:
    a. The HS3 Global Hawk mission (HIRAD and HIWRAP) and
    b. The National Weather Service NEXRAD,
2. The development of MatLab scripts to:
    a. Convert data into engineering and geophysical units and provide quality control flags,

b. Resample datasets into a common 3D grid that was spatially collocated and near-simultaneous in time,
c. Implement a forward HIRAD RTM that accepts 3D rain profiles from radar observations in separate upwelling and downwelling paths
d. Perform simulations of HIRAD Tb data and compare with HIRAD measurements

3. The analysis of the Tampa Bay Rain Experiment using the above MatLab tools, and
4. The publishing of scientific results in a referred journal [27].

7.2 Significance of the Tampa Bay Rain Experiment

On September 16, 2013, a tropical squall-line of thunderstorms was observed simultaneously by the remote sensors on board of the Global Hawk aircraft (HIRAD and HIWRAP) and the ground-based NEXRAD's at Tampa and Tallahassee, Florida. This was a serendipitous event that provided the crucial tropical precipitation observation dataset used in this dissertation. Moreover, there were two aspects about this experiment that makes it unique in the history of passive microwave remote sensing of precipitation. The first was the favorable combination of strong tropical rain that occurred over a relatively calm sea. Because wind speed and rain rate have overlapping brightness temperature signatures, it is very challenging to separate them, and this fortunate circumstance made the "perfect experiment"; whereby, the wind was constant while the rain varied over a wide dynamic range. The second aspect was the unprecedented combination of remote sensors that simultaneously viewed this intense rain event,

namely: the HIRAD multi-frequency microwave radiometer, the HIWRAP airborne meteorological radar, and two National Weather Service NEXRAD ground-based meteorological radars.

This was advantageous to this dissertation, because both HIWRAP and NEXRAD radars could provide independent "surface truth" for the validation of the HIRAD rain retrieval. The approach taken was to use the well-accepted NEXRAD rain measurements as the standard: to evaluate the HIRAD forward radiative transfer model, and to "tune" the HIWRAP rain measurements to match NEXRAD (in a least mean squares sense). After completing the "tuning" of HIRAD and HIWRAP, the plan was to perform the HIRAD rain rate retrievals, and validate these results using the independent HIWRAP 3D rain profiles.

However, since the newly developed HIWRAP instrument was an unproved rain remote sensor, this experiment also provided an opportunity to validate HIWRAP precipitation measurements. Unfortunately, as presented in Chapter 4, it was discovered that HIWRAP experienced significant rain attenuation, which prevented the 3D measurement of rain rate. Using the combined NEXRAD/HIWRAP dataset it should be possible to develop the necessary HIWRAP rain attenuation correction algorithm, but this effort is well beyond the scope of this dissertation, and it is recommended for future research.

To elaborate on this issue, NEXRAD provides accurate 3D rain profiles sequentially in time at fixed altitude levels during the 5-minute volume scan. Unfortunately, during this time interval, the tropical squall line of convective rain cells is continuously evolving (changing in intensity of rain rate and in storm location). To tune the HIWRAP observations, it will be necessary to construct the 3D simultaneous rain volume viewed by the conically scanning HIWRAP antenna.

A further complication are the differences in the viewing geometry of NEXRAD and HIWRAP, which must be taken into account. Once this is accomplished, then the attenuated HIWRAP observed rain reflectivity (versus range) series can be related to the integral of the true rain rate (provided by NEXRAD) along the line of sight of the conically scanning antenna beam. Clearly this is a major data analysis task, but conceptually feasible (future research) given the results of this dissertation.

7.3 Conclusions

The most significant scientific accomplishment of this dissertation is the incorporation of the 3D volumetric distribution of rain along separate upwelling and downwelling paths, in an "improved" HIRAD forward radiative transfer model. This means, that given the 3D rain distribution, the revised HIRAD forward RTM will accurately predict the top of the atmosphere observed brightness temperatures for the 5 & 6 GHz channels; which was validated in Chapter 5, by comparisons between modeled and measured HIRAD Tbs.

For future research, this means that a new HIRAD hurricane rain rate retrieval algorithm can be developed using computer simulation. The advantage of simulations (rather than experimental observation) is the ability to parametrically vary the wind speed and rain rate environmental parameters independently. Thus, it is recommended that a more sophisticated algorithm be developed to account for the rain rate profile along separate paths.

Another notable accomplishment of this dissertation research involves the ability to reliably identify the presence of rain in the HIRAD Tb observations. Based upon our results presented in Chapter 6, we believe that rain rate (averaged over the upwelling and downwelling

paths) can be retrieved. Moreover, we showed that the MLE retrieval of low WS and high RR were successful using simulated Tb measurements, whereby the measured NEXRAD RR were input to the RTM separately for the upwelling and downwelling path. Also, we evaluated the effect of antenna pattern convolution (APCv), using these same simulated Tbs and found that the retrievals were also excellent with only small impact on false RR pixels produced. Concerning wind speed retrievals, unfortunately, the radiometric calibration and stability of the HIRAD instrument is not sufficient to ensure a reasonable simultaneous wind speed retrieval. Thus, the retrieved rain rate can be used to provide an accurate "rain flag", which will be of significant benefit for scientific users of HIRAD hurricane retrievals.

Finally, a third notable accomplishment of this dissertation research involves the radiometric calibration of the HIRAD channel Tbs. Using the external clear-sky ocean scene (previously used) with a radiometric "hot" land scene (new for this dissertation) provides a two-point (total power radiometer calibration), which has two significant benefits:

1. Improved absolute radiometric calibration and especially intercalibration between different frequency channels, which was previously an issue for hurricane wind speed retrievals, and
2. Reduced "striping" in the Tb image.

Therefore, for future research, it is highly recommended that previous HIRAD hurricane flights be reprocessed using both ocean and land scenes whenever possible. Also, that the lessons learned in this dissertation be applied to the rain rate retrieval.

APPENDIX: A
HIWRAP GEOLOCATION ERROR ANALYSIS

This appendix presents details of the HIWRAP Geolocation error analysis that were summarized in Chap-3. To determine the geolocation error, we compared the location of the strong land/water features in the HIWRAP surface reflectivity image with the corresponding Google Earth map. Specifically, we performed an analysis of the HIWRAP surface reflectivity image of the northern Florida peninsula, which is shown in Figure A.1. The HIWRAP surface reflectivity image (dB) in the resampled HIRAD grid format showed a number of water/land boundaries (lakes, rivers and ocean coastline). The HIWRAP surface reflectivity image (dB in the resampled HIRAD grid format) showed a number of water/land boundaries (lakes, rivers and ocean coastline), where the geolocation comparisons were made.

We used the HIWRAP surface reflectivity resampled to the HIRAD grid format as presented in Figure A.2, which shows an expanded view of the pass over Lake Sampson. Note that each radar measurement is color coded using the dB scale on the right-hand side. In the upper image (native format), we can see a reduced density of radar measurements (pixels) that occur along conical arcs as compared to the resampled HIRAD grid along straight scan lines. At the left-hand side of the figure, the locus of 3 scan arcs are shown in the upper panel, and the corresponding locus of 6 HIRAD scans are shown in the lower panel. Also shown are the HIWRAP IFOV's as a red ellipses about the measurement pixels (native format), which show continuous radar spatial sampling in both the along-track and cross-track dimensions. Also, the lake boundary is shown as the bold "circle pattern", and note that the lake diameter is 3 – 4 IFOV's, which allows the land/water boundary to be readily resolved in the radar image.

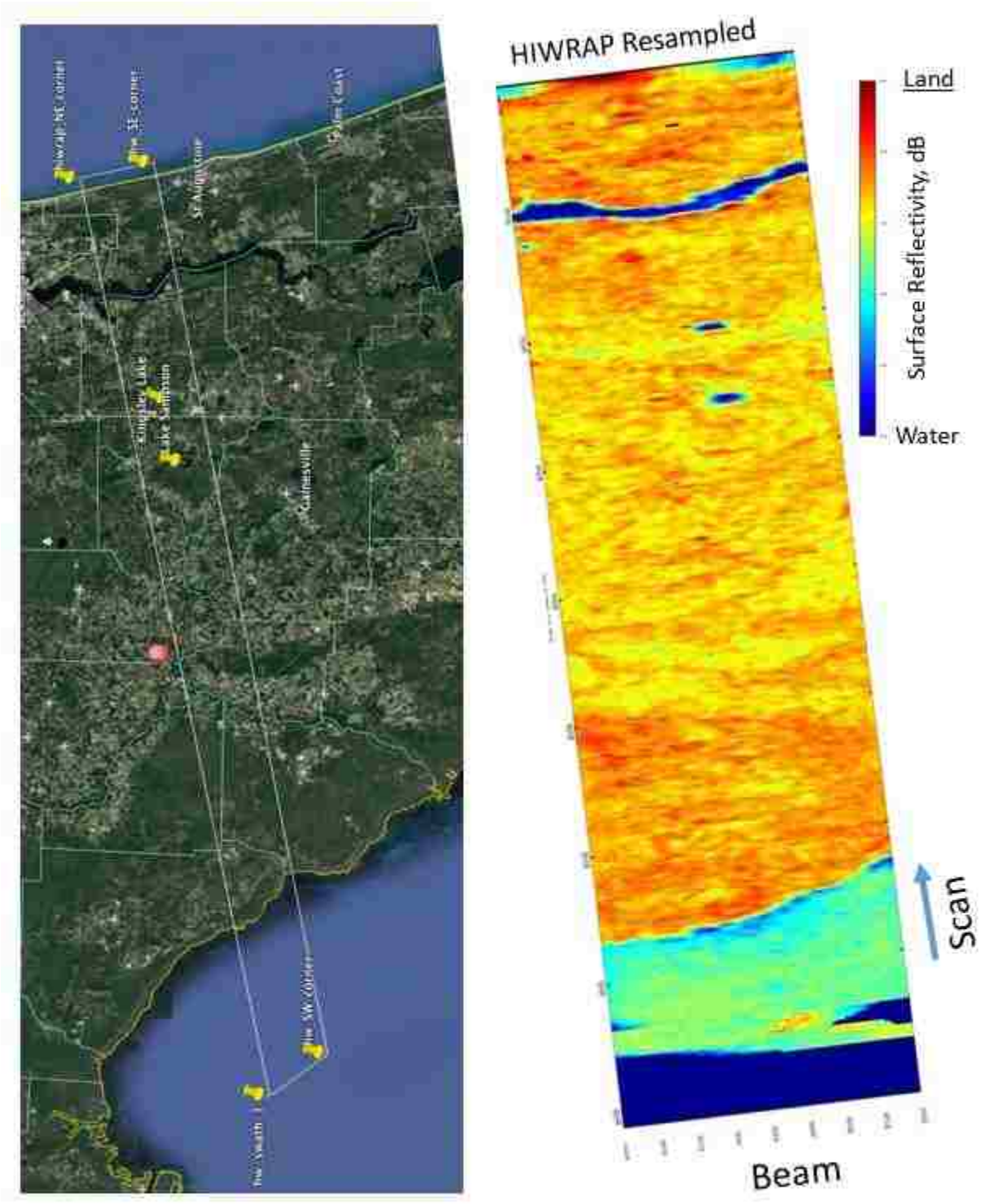

Figure A.1: Global Hawk pass over North FL (Google Earth – left side) with the HIWRAP swath of surface reflectivity indicated in false color image (right side).

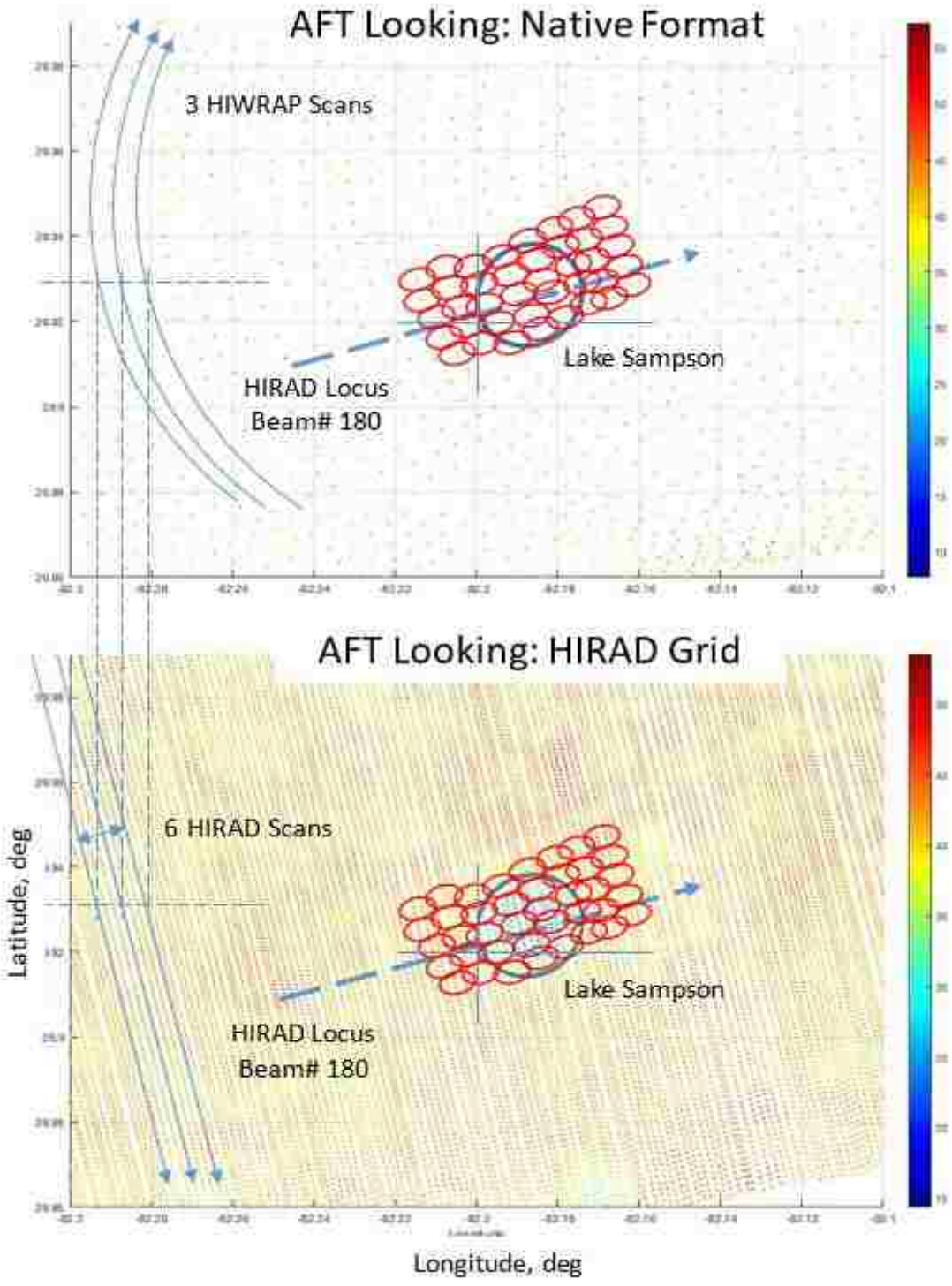

Figure A.2: Comparison of HIWRAP surface reflectivity image in Native and HIRAD grid formats for Lake Sampson.

Next, The HIWRAP data were analyzed using the time series along a fixed beam position for the transition over land/water boundaries that occurred at: (1) the Gulf coast, (2) inland lakes, (3) the St. Johns River and (4) the Atlantic coast.

Gulf Coast: The HIWRAP measurements over the gulf coast were excluded from this evaluation because a major part of the coastline is covered with marsh (wetland) as shown in Figures A.3 & A.4. These wetlands are a mixture of land and water, and as a result there is NOT a sharp discontinuity between land and water upon which to denote the boundary. The fact that these marshes extend to up to a few km from the Gulf Coast, causes a gradual transition of the surface reflectivity shown in Figure A.4. As a result, the first derivative of reflectivity (reflectivity slope) is very weak and cannot define a definite point between water and land. For this reason, these data were not included in the geolocation error determination.

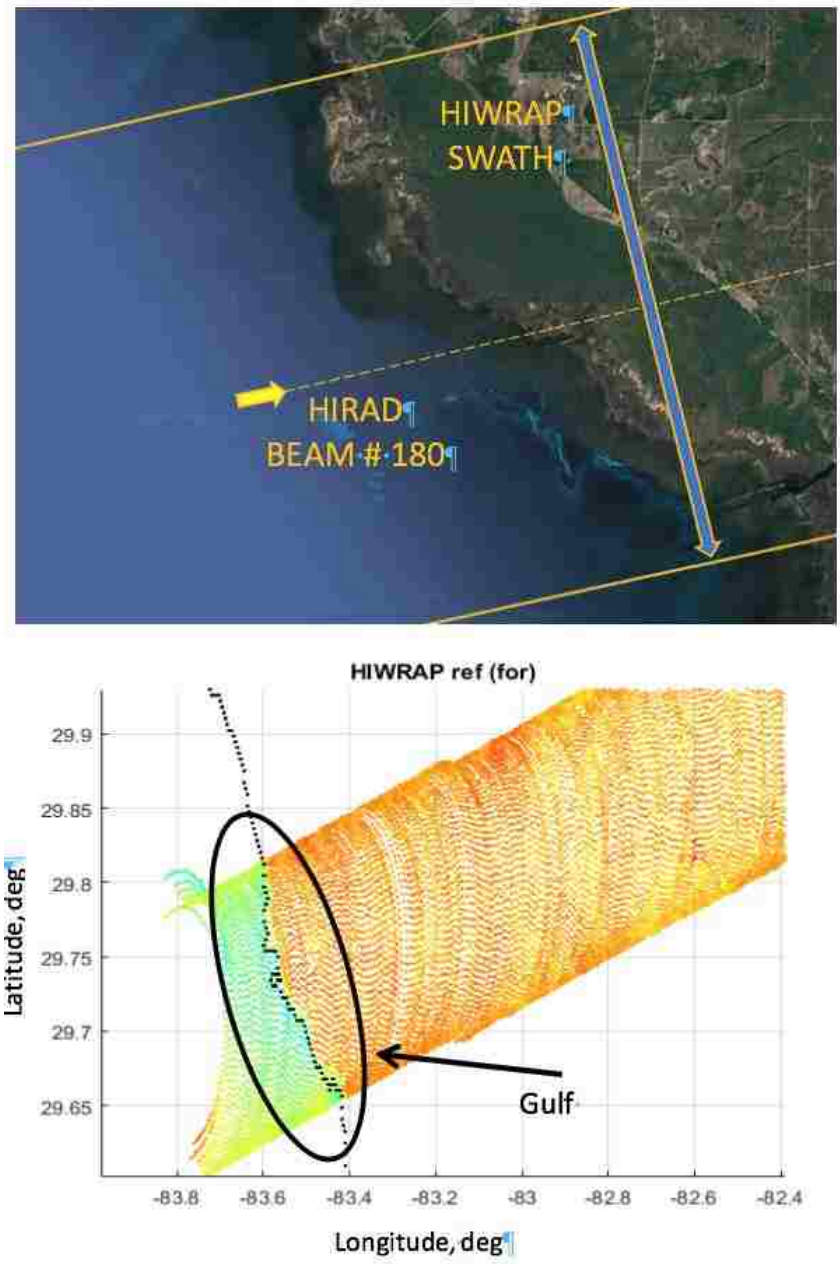

Figure A.3: HIWRAP surface reflectivity (Native format) over Gulf Coast with the locus of beam=180 shown as dashed line and dotted high-resolution coast-line in lower panel.

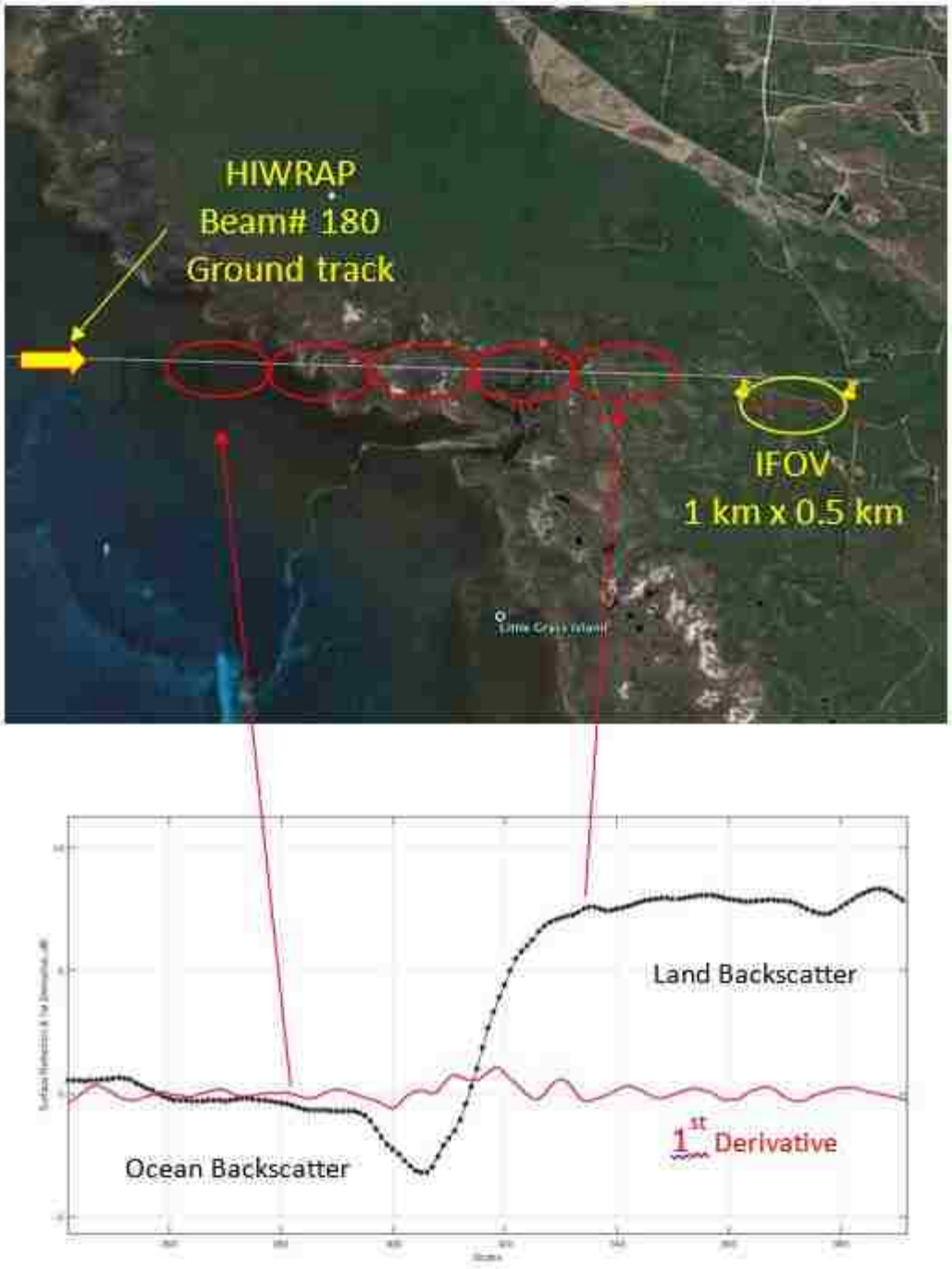

Figure A.4: Google Earth image with ground track for beam=180 (upper panel). Lower panel: Time series of HIWRAP surface reflectivity (HIRAD format) and reflectivity slope (1st derivative) transition over Gulf Coast.

Lake Sampson and Kingsley: The HIWRAP beam # 180 passed directly over these lakes as shown in Figure A.5 (upper panel). The middle and lower panels compare the surface reflectivity image before and after smoothing (low-pass filter).

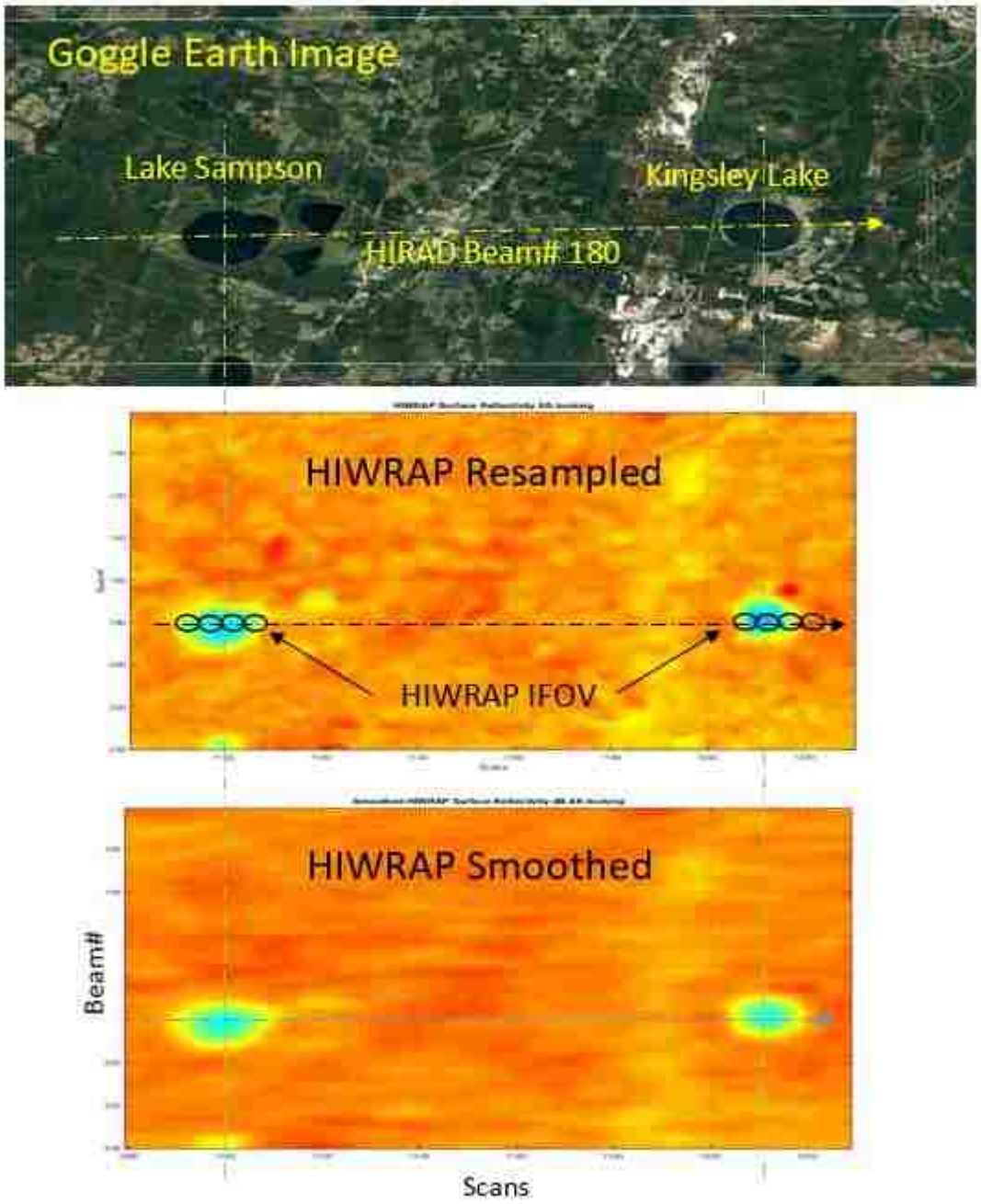

Figure A.5: Google Earth image with ground track for beam=180 (upper panel) that pass over two lakes. Lower panels: Images of HIWRAP surface reflectivity (HIRAD format, dB) and smoothed surface reflectivity and note strong contrast between land (red) & water (green).

Results presented in Figure A.6 (upper panel) demonstrate that fore- and aft looks are nearly identical and yield the same land/water transition location. Further, in the two lower panels, the peak reflectivity slope provides a robust estimate of the land/water boundary.

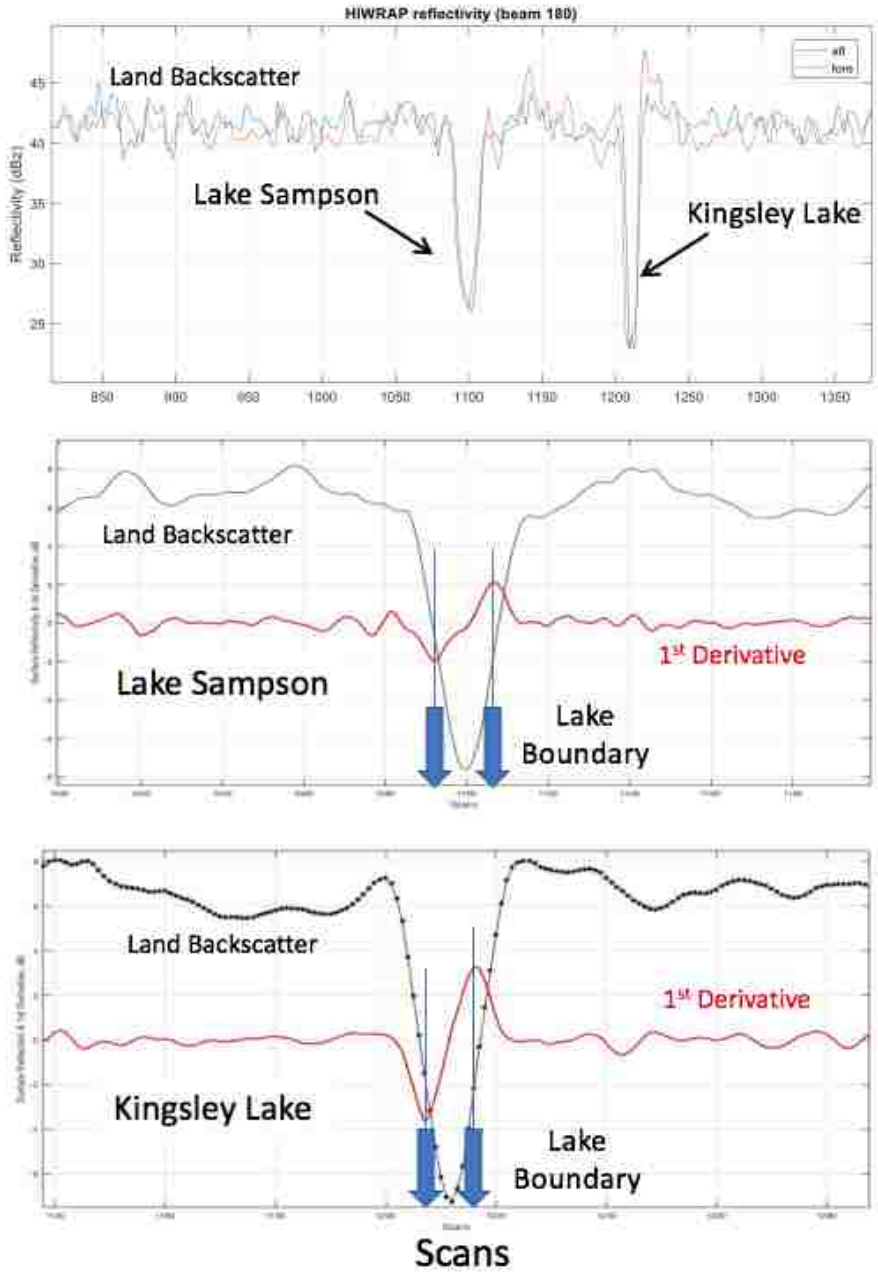

Figure A.6: Upper panel: time series of HIWRAP reflectivity for fore- (red) and aft- (blue) looking positions for Beam# 180. Middle & lower panels: expanded reflectivity time series (black) for Sampson & Kingsley respectively with strong peaks in the reflectivity first derivative (red) indicating the location of the land/water boundary.

St Johns River: Results for the HIWRAP geolocation analysis over the river are presented in Figures A.7, 8 & 9. The latter two figures show the effect of the low-pass smoothing, which significantly reduces the 1st derivative noise. As a result, this improves the determination of the location of the peak reflectivity slope (that corresponds to the land/water boundary).

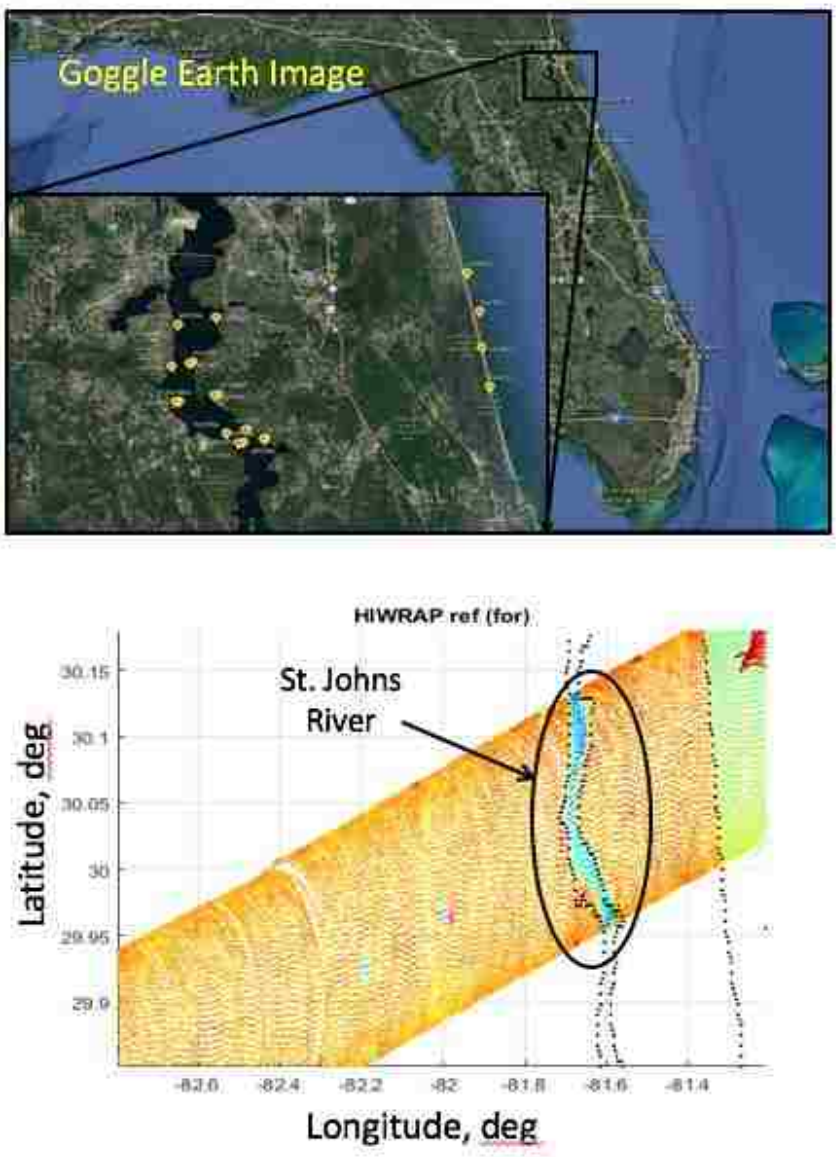

Figure A.7: Upper panel: Google Earth Image of the St. Johns River, and lower panel: corresponding HIWRAP reflectivity image (native format, dB).

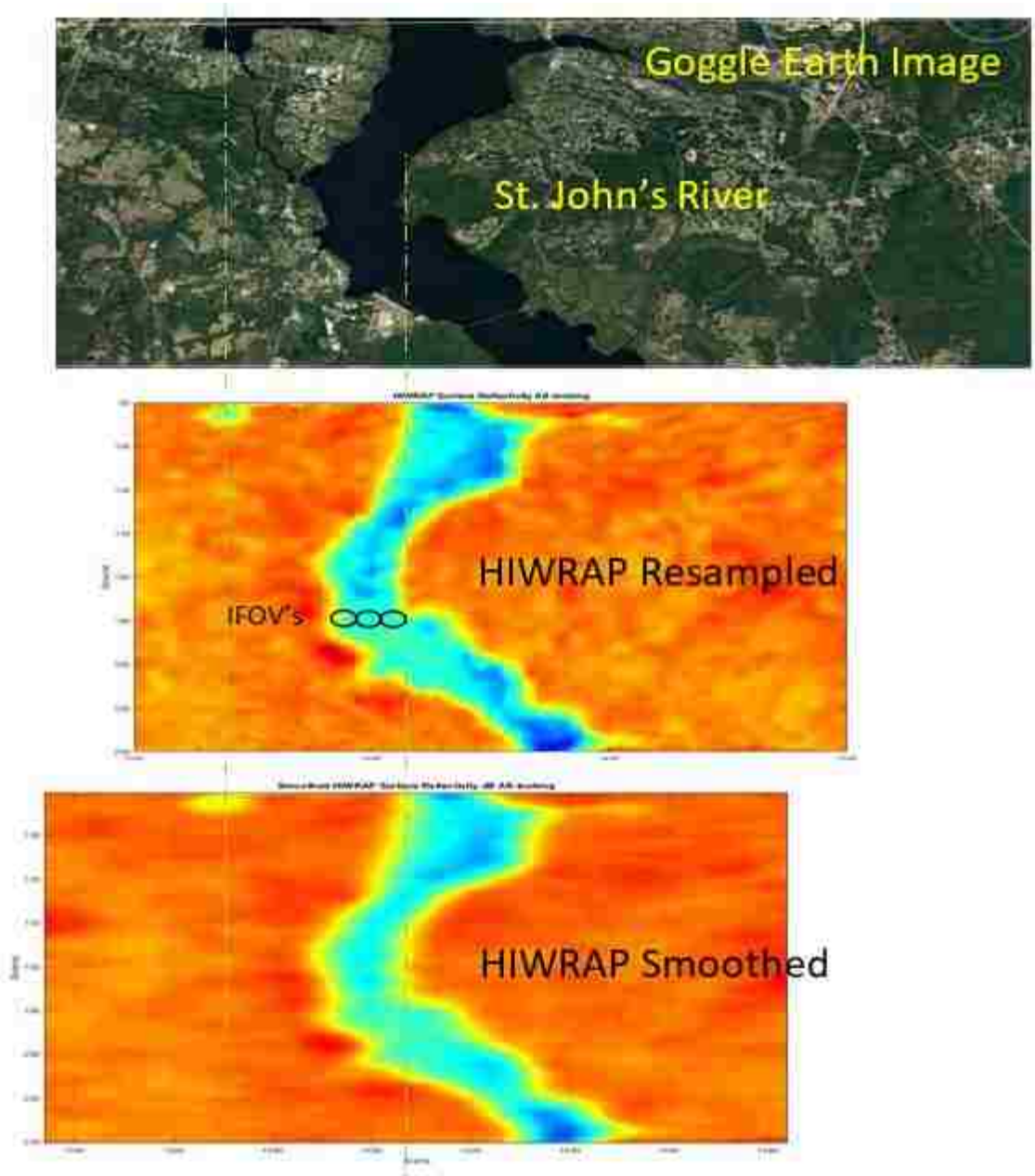

Figure A.8: Upper panel: Google Earth Image of the St. Johns River, and lower panels: Images of HIWRAP surface reflectivity (HIRAD format, dB) and smoothed surface reflectivity.

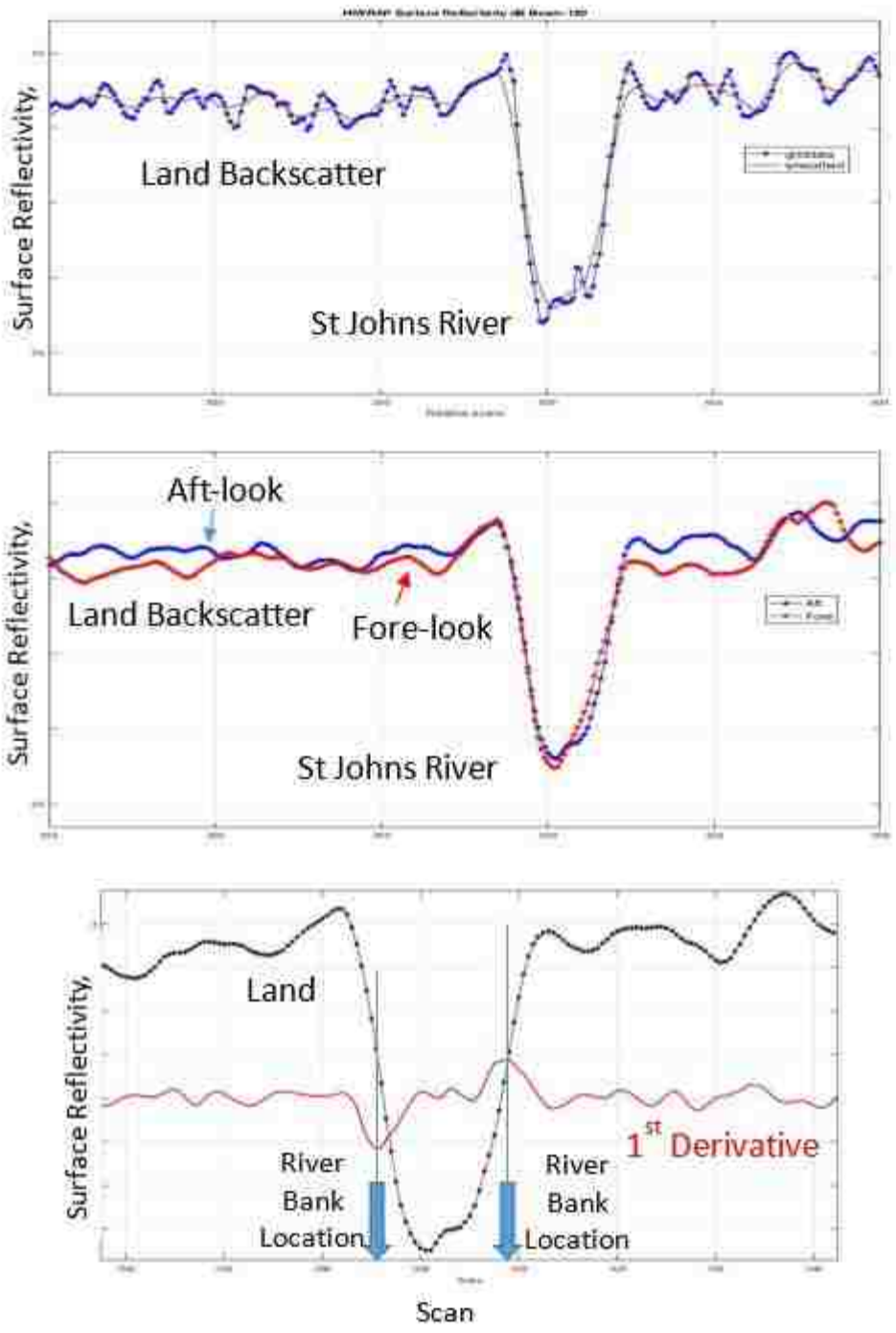

Figure A.9: Upper panel: time series of HIWRAP reflectivity (blue) and smoothed (red) for Beam# 180; Middle panel: smoothed reflectivity time series for fore- (red) and aft- (blue) looking positions; Lower panel: expanded fore-looking reflectivity time series (black) and the reflectivity first derivative (red), where derivative peaks indicate river bank location.

Atlantic Ocean Coast: The HIWRAP beam # 220 fore- and aft-looks passed directly over Atlantic coastline, and results are shown in Figures A.10 & 11. The locations for the peak reflectivity slopes were entered on the Google Earth map and the distance between the map and image locations were tabulated and presented in Chap-3.

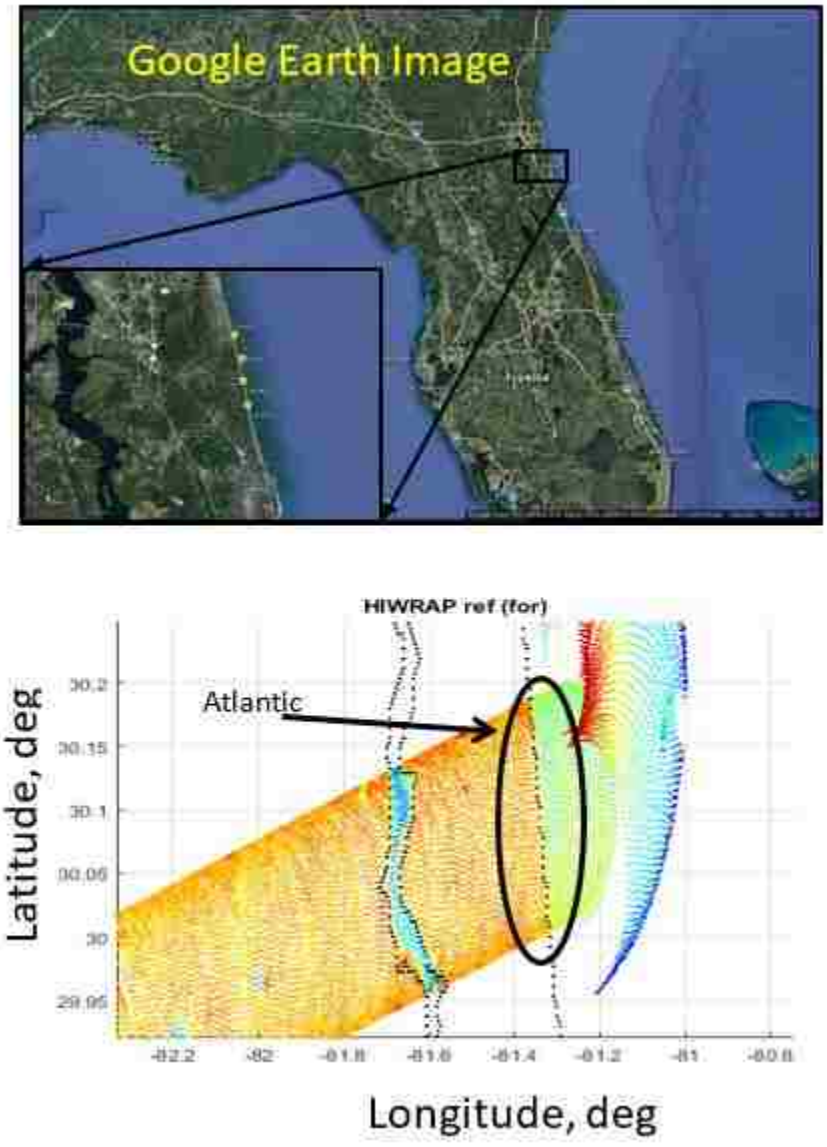

Figure A.10: Upper panel: Google Earth Image of the Atlantic Ocean coast at Jacksonville, and Lower panel: corresponding fore-looking HIWRAP reflectivity image (native format, dB). Note: red trace indicates the location of the conical scan pixels during an aircraft turn.

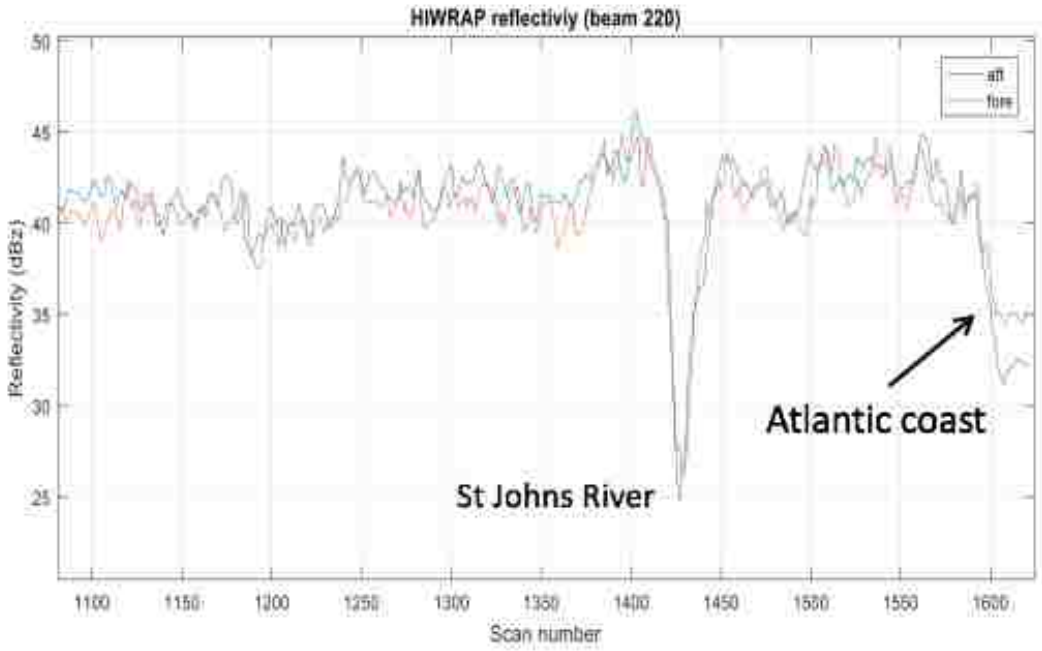

Figure A.11: Time series of HIWRAP reflectivity for fore- (blue) and aft-looking (red) positions for Beam# 220 over the St. Johns River and the Atlantic Ocean coast.

LIST OF REFERENCES

[1]. Eric W. Uhlhorn, Peter G. Black, James L. Franklin, and Alan S. Goldstein, "Hurricane Surface Wind Measurements from an Operational Stepped Frequency Microwave Radiometer," Mon. Wea. Rev., vol. 135, pp. 3070-3085, September 2007.

[2]. Jones, W. L., Zec, J., Johnson, J. W., Ruf, C. and M. C. Bailey, "A Feasibility Study for a Wide-Swath, High Resolution, Airborne Microwave Radiometer for Operational Hurricane Measurements", IEEE IGARSS 20002, Jun 24-28, 2002, Toronto, Ontario, Canada.

[3]. Johnson, James W., Amarin, R. A., El-Nimri, Salem F., and W. Linwood Jones "A Wide-Swath, Hurricane Imaging Radiometer for Airborne Operational Measurements", Proc. IEEE IGARSS-06, Aug. 28 - Sept. 1, 2006, Denver, CO.

[4]. Robbie Hood, R. Amarin, M. Bailey, P. Black, M. James, J. Johnson, L. Jones, B. Lim, C. Ruf, K. Stephens, and V. Rohwedder, "Development of the Hurricane Imaging Radiometer (HIRAD) Using a Systems Engineering Approach, 61st Interdepartmental Hurricane Conference, March 5-9, 2007, New Orleans, LA.

[5]. Ruba A. Amarin; Jones, W. L.; El-Nimri, S.F.; Johnson, J. W.; Ruf, C. S.; Miller, T. L. and E. Uhlhorn; "Hurricane Wind Speed Measurements in Rainy Conditions using the Airborne Hurricane Imaging Radiometer (HIRAD)"; IEEE Trans. GeoSci. Remote Sens., vol. 50, issue: 1, pp. 180-192, Jan. 2012.

[6]. Amarin, Ruba, "Hurricane Wind Speed And Rain Rate Measurements Using The Airborne Hurricane Imaging Radiometer (hirad)" (2010). Electronic Theses and Dissertations. 4223. https://stars.library.ucf.edu/etd/4223.

[7]. Maria Marta Jacob, Matin Salemirad, W. Linwood Jones, Sayak Biswas and Daniel Cecil, " Validation of Rain Rate Retrievals for the Airborne Hurricane Imaging Radiometer (HIRAD) ", Proc. 2015 IEEE Internat Geosci and Rem Sens Symp (IGARSS), Milan, Italy, July 27-31, 2015, pp. 902-905. doi: 10.1109/IGARSS.2015.7325911.

[8]. Braun, S.A., P.A. Newman, et al. (2016). NASA's Hurricane and Severe Storm Sentinel (HS3) Investigation. BAMS, November 2016, 2085-2102. doi: 10.1175/BAMS-D-15-00186.1.

[9]. Ruf CS, Swift CT, Tanner AB, Le Vine DM. Interferometric synthetic aperture microwave radiometry for the remote sensing of the earth. IEEE Trans Geosci Remote Sens. 1988;26(5):597–611.

[10]. M. C. Bailey, R. A. Amarin, J. Johnson, P. Nelson, M. James, D. Simmons, C. Ruf, W. L. Jones, and X. Gong, "Multi-Frequency Synthetic Thinned Array Antenna for the Hurricane Imaging Radiometer," IEEE AP-S Transactions on Antennas and Propagation, 2010.

[11]. Li, L., G. M. Heymsfield, J. Carswell, D. Schaubert, J. Creticos, and M. Vega, 2008: High-Altitude Imaging Wind and Rain Airborne Radar (HIWRAP). 2008 IEEE International Geoscience and Remote Sensing Symposium: Proceedings, IEEE, III-354–III-357, doi:10.1109/IGARSS.2008.4779356.

[12]. Federal Meteorological Handbook No. 11, 1990: Doppler radar meteorological observations, Part B, Doppler radar theory and meteorology. FCM-H11B-1990, Interim Version One. Office of the Federal Coordinator for Meteorological Services and Supporting Research, Rockville, Maryland, 228 pp.

[13]. https://support.hdfgroup.org/HDF5/doc/H5.intro.html

[14]. Personal communications: G. M. Heymsfield, NASA Goddard Space Flight Center, 2015.

[15]. Saleem Sahawneh, Linwood Jones, Sayak Biswas and Daniel Cecil, “HIRAD Brightness Temperature Image Geolocation Validation,” IEEE Geosci. and Rem. Sens. Letters, vol. 14, issue 11, Nov. 2017, pp. 1908-1912, doi: 10.1109/LGRS.2017.2731121.

[16]. B. Clymer, C. May, L. Schneider, F. Madero, M. Labanda, M. M. Jacob, et al., "Microwave radiometer (MWR) beam-pointing validation for the Aquarius/SAC-D mission," in Microwave Radiometry and Remote Sensing of the Environment (MicroRad), 2014 13th Specialist Meeting on, 2014, pp. 221-225.

[17]. Rinehart, R. E. 1997. Radar for meteorologists. Grand Forks, ND: Rinehart Publishing.

[18]. Fulton, R. A., J. P. Breidenbach, D.-J. Seo, D. A. Miller, and T. O’Bannon, 1998: The WSR-88D rainfall algorithm. Wea. Forecasting, 13, 377–395,

[19]. Sahawneh, Saleem, "Evaluation of the Hurricane Imaging Radiometer (HIRAD) Brightness Temperatures" (2017). Electronic Theses and Dissertations. 5389. https://stars.library.ucf.edu/etd/5389

[20]. C. Ruf, J. B. Roberts, S. Biswas, M. James, and T. Miller, "Calibration and image reconstruction for The Hurricane Imaging Radiometer (HIRAD)," in 2012 IEEE International Geoscience and Remote Sensing Symposium, 2012, pp. 4641-4643.

[21]. Abdusalam Alasgah*, M. Jacob, and W Linwood Jones (2017), “Removal of Artifacts from Hurricane Imaging Radiometer Tb Images,“ Proc. IEEE 2017 SoutheastCon, Mar 3-Apr 2, Concord, NC. doi: 10.1109/SECON.2017.7925284.

[22]. El-Nimri, Salem, "Development Of An Improved Microwave Ocean Surface Emissivity Radiative Transfer Model" (2010). Electronic Theses and Dissertations. 4224. https://stars.library.ucf.edu/etd/4224.

[23]. El-Nimri, Salem F., W. Linwood Jones, Eric Uhlhorn, Christopher Ruf, James Johnson, and Peter Black, “An Improved C-Band Ocean Surface Emissivity Model at Hurricane-Force Wind Speeds over a Wide Range of Earth Incidence Angles:, IEEE Geosci. & Remote Sens. Letters, Vol. 7, no. 4, pp. 641-645, Oct 2010.

[24]. Klotz, B.W. and E.W. Uhlhorn, 2014: Improved Stepped Frequency Microwave Radiometer Tropical Cyclone Surface Winds in Heavy Precipitation. J. Atmos. Oceanic Technol., 31, 2392–2408, https://doi.org/10.1175/JTECH-D-14-00028.1

[25]. NCEP (National Centers for Environmental Prediction) FNL (Final) Operational Global Analyses. Available: http://rda.ucar.edu/datasets/ds083.2.

[26]. Ulaby, F.; Long, D., *Microwave Radar and Radiometric Remote Sensing;* Univ. Mich Press: Michigan, USA, 2014; pp. 236-239, ISBN: 978-0-472-11935-6.

[27]. Alasgah, Abdusalam; Jacob, Maria; Jones, Linwood; Schneider, Larry. 2019. "Validation of the Hurricane Imaging Radiometer Forward Radiative Transfer Model for a Convective Rain Event." *Remote Sens.* 11, no. 22: 2650.